Predicting Tumour Response

Using magnetic resonance imaging to predict tumour response of HER2+ breast cancer patients.

Nathalie Lisa Oudhof
Delft University of Technologie

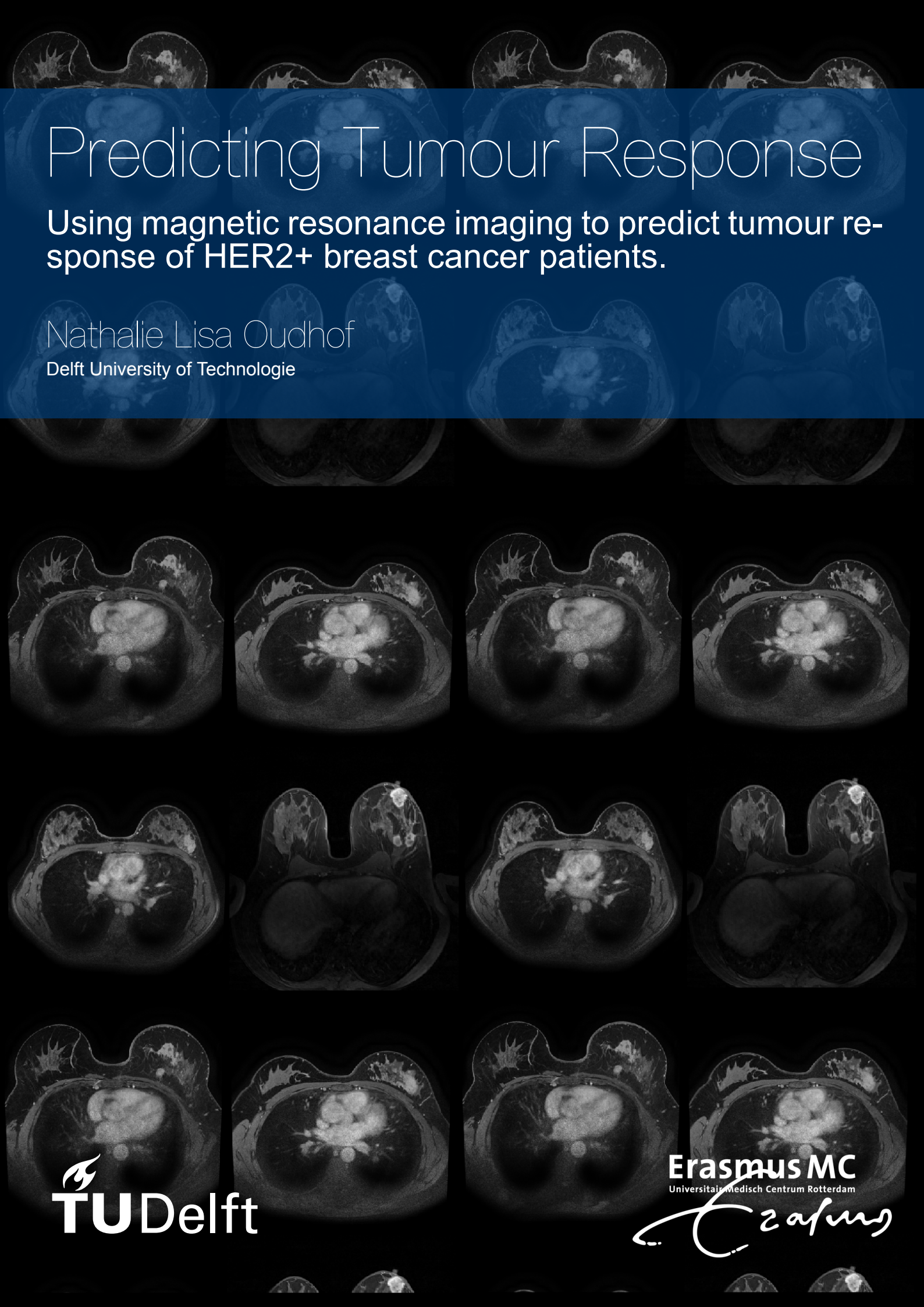

TU Delft

Erasmus MC
Universitair Medisch Centrum Rotterdam

Predicting Tumour Response

Using magnetic resonance imaging to predict tumour response of HER2+ breast cancer patients.

by

Nathalie Lisa Oudhof

to obtain the degree of Master of Science
at the Delft University of Technology.

Student number: 4370449
Project duration: April 1, 2021 – April 13, 2022
Thesis committee: Prof. dr. ir. M. van Gijzen, TU Delft
Dr. ir. E. G. Rens, TU Delft
Dr. A. Jager, Erasmus MC

TU Delft

Erasmus MC

Abstract

Every year, thousands of women are diagnosed with breast cancer. To increase their survival chance and improve the treatment plans available, it is important to accurately predict the patient's response to treatment. For HER2+ breast cancer patients, normally a set number of chemotherapy rounds are administered. However, perhaps some patients would benefit from more chemotherapy or conversely, fewer rounds are sufficient. A reaction-diffusion model as well as a mechanically coupled reaction-diffusion model are used to predict the tumour cellularity. Using two magnetic resonance imaging (MRI) scans, a patient-specific model is calibrated to calculate the response for each individual patient. A third MRI scan is used to validate the results. Several preprocessing techniques are used to obtain the necessary information from the MRI scans such as tumour cellularity, segmentation of tissues and breast region.

The model calculations are performed in 2-dimensions and the slice thickness chosen determines how much effect the incorporation of surrounding tissue has. Using thicker slices means that the surrounding tissue has a larger effect on the tumour growth. For patients that respond well to treatment, the models are both able to calculate the downward trend in tumour cellularity. For thin slices (1.6 mm), both models perform similarly. Using thicker slices (6.5 mm), the mechanically coupled model shows better performance. The most important additions to the model are implementation in 3-dimensions so the slice thickness no longer has an effect. Most importantly, the chemotherapy should be incorporated to better obtain a patient-specific prediction of the response to treatment.

Preface

This thesis will mark the end of my master of Applied Mathematics at Delft University of Technology. Starting my bachelor and even master, I would not have expected mathematics to play such an important role in the medical field. It was very important to me to apply the skills I had obtained during my time in Delft to a societal problem such as sustainability or medicine. I was very happy to have been able to do my thesis in collaboration with Erasmus Medical Centre and perform research on a topic that is so important.

Having done my master's and thesis during the pandemic has challenged me in many different ways. Unfortunately, most meetings were still online and most of my research was done at home. I would like to thank my supervisors for supporting me both mentally and academically. To Martin and Lisanne, I thank you for the mathematical and analytical insights to perform this master thesis as well as the weekly meetings which always made me smile. To Agnes, I thank you for the medical insights and enthusiasm during the project which motivated me to keep going.

Also many thanks to my friends and family who offered to proofread and kept me going. In particular, Tobias, who not only helped proofread but also let me bounce ideas off of him and kept me grounded.

Nathalie Lisa Oudhof
Delft, April 2022

Contents

List of Figures

List of Tables

1

Introduction

Cancer is one of the leading causes of death worldwide and the leading type of cancer in women. In 2020 alone, almost 10 million people succumbed to the disease and one in seven women will develop breast cancer in their lifetime [48]. Whilst the 5-year survival rate is now 89% in the Netherlands, compared to 52% in 1952, there are still about 3,000 deaths annually [5]. With more than 18 types of breast cancer, breast cancer can occur in several different areas of the breast, most commonly in the ducts or lobules [6, 37]. Ductal carcinomas are the most common kinds of breast cancer where the cancer starts in the cells lining the milk ducts [7]. Approximately 75% of breast tumours are ductal types, and only about 15% are lobular types. Figure 1.1 shows an illustration of the location of ducts and lobules in the breast.

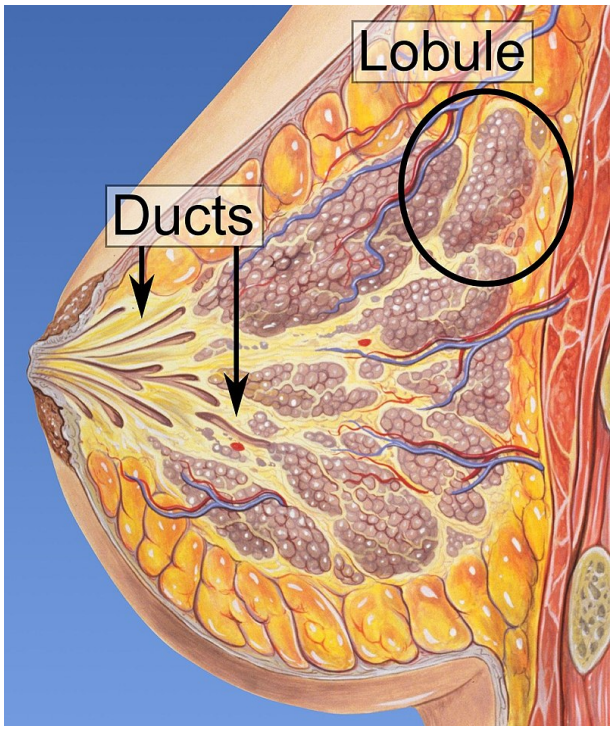

Figure 1.1: Location of ducts and lobules within a female breast [13].

Whenever a patient is diagnosed with breast cancer, it is classified by several grading systems, i.e. histopathology, grade, stage and receptor status. These grading systems are used to determine the best treatment plan [39].

- Histopathologic: This is determined by the histologic appearance of the tumour and can be broadly classified into two categories; carcinomas in situ and invasive carcinoma.
- Grade: This is based on how similar the cancer cells are to normal cells which is determined in the laboratory. Grade 1 means the tumour cells look very similar to normal cells and thus the tumour will spread slower. Grade 3 is the highest grade where the cells are very different and will grow and spread faster.
- Stage: Stages in breast cancer indicates how much cancer is in the body. The stages are between 0 and 4 where the higher the stage, the more widespread the cancer is.
- Receptor Status: Cells are tested to see if they have certain proteins that are either estrogen or progesterone receptors. Receptor status is especially important as it determines the suitability of the treatment options.

Evidently, there are several different combinations of grading systems. In this thesis, we will focus on one subtype of receptor status, namely HER2 positive tumours. There are three main subtypes of receptor status; Hormone receptor positive, HER2 positive and triple negative [7]. Firstly, hormone receptor positive (HR+) entails breast cancer which expresses either estrogen receptors (ER+) or progesterone receptors (PR+), or in some cases both. This type of breast cancer may depend on either of these hormones to grow. Furthermore, while it can occur at any age, this subtype is most common in women who have gone through menopause and about 2 out of 3 breast cancers are classed as hormone receptor positive. When a patient is neither ER+ nor PR+, they are called hormone receptor negative (HR-). Next, we have HER2 positive (HER2+), which is breast cancer that tests positive for a protein called human epidermal growth factor receptor 2. This protein is found on all breast cells and promotes growth, so breast cancer with a higher level of HER2 than normal is called HER2-positive, or HER2+. These cancers are known to grow and spread faster since the overexpression of the HER2 gene causes excessive cell division. About 20% of breast cancers are HER2+. Fortunately, these tumours also tend to respond favourably to treatment. Lastly, there is the subtype called triple negative. Breast cancer is classified as triple negative when it is neither HER2, estrogen nor progesterone positive. This type is the least common, only occurring about 15% but unfortunately has limited treatment plans and the worst prognosis.

1.1. Treatment

Once a patient has been diagnosed with breast cancer, a treatment plan has to be made. The goal of the treatment plan is to minimize burden to the patient whilst maximizing their potential to fully recover. Treatment can be in the form of chemotherapy, surgery, radiotherapy or a combination of these. If the cancer is locally advanced but had not yet spread to other parts of the body, i.e. metastasised, neoadjuvant chemotherapy can be administered. Neoadjuvant chemotherapy is the administration of chemotherapy prior to surgery. This helps reduce the tumour size, such that a mastectomy is no longer necessary but only a lumpectomy, i.e. the removal of the tumour, which is less invasive [45].

The growth of a tumour remains a complex process and the response to treatment for the same tumour type can vary per patient. With various different chemotherapy treatments available, and even more treatments emerging, it is of high interest to reliably predict a patient's specific response to treatment which results in the best possible treatment plan. Each treatment has a range of side effects, by accurately predicting the patient's response to said treatment, it could prevent the side effects of noneffective treatments. Additionally, patients who achieve a pathological complete response, pCR, in the neoadjuvant setting have increased chances of recurrence-free survival [19]. Pathological complete response is defined as the absence of residual tumour in the breast or nodes by histologic analysis [44]. Unfortunately, current neoadjuvant therapy is not optimized for each patient individually [20]. Based on the receptor status, tumour grade etc., the patients are given a set

number of chemotherapy cycles prior to operation. The patients' physiological characteristics such as breast density are not taken into account. The advantages for reliably predicting the outcome of neoadjuvant chemotherapy as early as possible is that it can help reduce unnecessary treatments and its related side effects on patients, since chemotherapy not only attacks tumour tissue but healthy tissue as well [44]. Furthermore, with numerous treatment plans available, unresponsive patients could change treatment for better individual care.

1.2. Research Aim

In this thesis, we will consider HER2-positive breast cancer patients as it is known that for these patients, neoadjuvant chemotherapy often leads to pCR [40]. In general, a set number of cycles of chemotherapy is given before surgery. However, it is unclear how many cycles a specific patient would need to achieve pCR. Some patients could need fewer cycles than others. For these patients, reducing the amount of unnecessary chemotherapy reduces the amount of treatment related toxicities. Conversely, for some patients, it could be beneficial to continue administering more chemotherapy to increase their chance of achieving pCR. Therefore, it is important to accurately predict how many cycles of chemotherapy a patient will need to achieve pCR.

The research in this thesis will focus on providing a model which can predict how the tumour will change over time. To make a mathematical model for tumour growth, knowledge of parameters is required [2]. There are many approaches to model tumour growth. Unfortunately, many of these are models which are not directly applicable to individual patients as they are unable to easily incorporate clinical data [44]. Additionally, they require a multitude of parameters which either have to be obtained from literature or empirically derived. This causes them to be impractical for predicting individual patient's outcome. In this thesis, we focus on creating a mathematical model which can maximize the impact of quantitative noninvasive imaging in order to predict patient-specific response. To find the parameters of the model, this research focuses on using noninvasive magnetic resonance imaging, MRI. By using MRI scans for each individual patient, a patient-specific model can be created to predict their outcome. For each patient, MRI scans at three different time points will be used, one prior to, one during and one at the conclusion of chemotherapy. The idea of using three MRI scans is to initialize the model parameters using the pre-treatment MRI scan, then the parameters can be calibrated with the follow-up scan and be validated with the last scan. Using these biomarkers, the predictive model can then be used to estimate the number of tumour cells after each additional cycle of chemotherapy. Then, a threshold can be chosen to determine when the patient has achieved pCR.

1.2.1. Research Questions

The main research question for this thesis is: *Can a mathematical model of tumour growth predict patient-specific response for HER2+ breast cancer patients?*

The answer to this question will be answered by the following subquestions:

- What kind of preprocessing techniques need to be applied to the MRI scans?
- How can MRI scans be used to calibrate and validate the model for patient-specific response?
- What kind of MRI scans can be used best to calibrate and validate the model?
- What patient-specific parameters are necessary for the model?
- Does taking the surrounding tissue into account help make the model more accurate?

In this thesis, an answer to these questions shall be presented.

1.3. Structure of Thesis

The structure of this thesis is as follows. First, Chapter 2 provides an overview of available literature on the modelling of tumour growth. Then, Chapter 3 discusses the data provided by Erasmus Medical Centre and the preprocessing of the data to extract the necessary information for each patient. Chapter 4 will explain the model implementation as well as the calibration of the model parameters. In Chapter 5, the preliminary results of model calculations are given as well as some in silico experiments to illustrate the performance of the model. Chapter 6 will present the results of the model which is tested on the data provided by EMC. The model is tested on each patient to see how it performs. In Chapter 7, the potential for future improvements is provided to improve the predictive capability of the model. Lastly, the conclusion provides and an answer to the main research question as well as some discussion of what the most important improvements are, will be provided in Chapter 8.

1.4. Review of Medical Ethics Committee Erasmus Medical Centre

This research has been carried out in collaboration with Erasmus Medical Centre, Rotterdam. Medical research which involves human subjects is covered by the Medical Research Involving Human Subjects Act (WMO). The Medical Ethics Committee from Erasmus Medical Centre of Rotterdam has reviewed the research proposal of this study and concluded that it is not subject to the WMO. Therefore, the provided data from Erasmus Medical Centre has been anonymised prior to conducting this research.

2

Review of Literature

The aim of this chapter is to provide insight into current tumour modelling techniques, and to review and determine which model is most promising for our objective. There are different ways to predict the growth of a tumour located in the breast. The standard way is to monitor the change in tumour size by physical examination or imaging. However, these methods often do not show if a tumour is responding until several cycles of chemotherapy have been administered and may be invasive [45]. This can lead to letting an unresponsive tumour becoming unresectable. In general, there are three main mathematical approaches to model tumour growth: discrete, continuum and hybrid modelling [29]. We will briefly explain discrete and hybrid modelling and focus mainly on continuum modelling.

2.1. Discrete Modelling

Discrete modelling can be used to model interactions of individual cells with each other and their environment. The cells are individually tracked and follow a set of biophysical rules [29]. Within discrete models, there are two main types, on-lattice and off-lattice [34]. On lattice models, as the name suggests, are constrained to a lattice which can be triangular, square, hexagonal, etc. This lattice defines the positions of the individual cells and their interaction neighbours. These models are generally easier to program than off-lattice models. However, the main disadvantage is that these models limit the number of directions in which the cells can move. Conversely, in off-lattice models, there is a more realistic representation of the cell locations. However, during cell division, it is important to determine the correct placement for daughter cells in order not to overlap. Additionally, the freedom of movement in all directions of the cells could result in cell collisions. For these types of lattices, the main disadvantage is that special algorithms need to be implemented to handle cell-cell neighbourhoods which makes them more complex. The two main discrete models are cellular automata and agent-based models [43]. Cellular automata in an on lattice model which synchronously evolves through time and with identical rules applied to each cell. On the other hand, agent-based models asynchronously evolves through time and have dynamic interactions between the agents and their environments. In this approach, each individual cell is represented as an agent. Because this approach is asynchronous, it is appealing to use for simulating tumours as they are heterogeneous and display behaviour that cannot be reduced to an averaged, simple mechanism. As discrete models use a series of rules for each cell, they can incorporate biological processes into the model based on data or assumptions. However, the computational cost for discrete models grows rapidly as the number of cells increases. Currently, simulation of only 1 mm^3 of tumour spheroid is not feasible using only a discrete approach as this spheroid would already contain more than a hundred thousand cells [29]. Additionally, obtaining measurements for model parameters can be challenging and may need to be done invasively. As such, a discrete approach is not feasible for the application in this thesis, but is a suitable approach for applications on a sub-millimeter scale [43].

2.2. Continuum Modelling

Continuum modelling methods are based on reaction-diffusion equations to describe tumour cell density, growth factors and inhibitors. This approach models tumours as a collection of tissue and allows monitoring of the expansion of a larger cluster of cells [43]. Unlike discrete modelling, individual cells are not tracked. This means the model can lack sensitivity to small local fluctuations within the tumour, such as tumour angiogenetic sprouting, i.e. the event where the tumour grows new blood vessels from existing ones [43]. A major advantage of continuum models is that model parameters are somewhat easy to obtain, analyse and control in comparison to discrete modelling [29]. Moreover, the computational cost is less than for discrete modelling. In general, continuum modelling is an appropriate choice for applications where one is interested in gross tumour behaviour, but is unsuitable for modelling the development of the tumour on an individual cellular level. This makes this type of modelling suitable for our objective since we are interested in modelling the overall change of the tumour rather than the individual tumour cells.

2.2.1. Reaction-Diffusion

Reaction-diffusion models are also known as mechanism-based mathematical models and are based on the assumption that the behaviour of a complex system can be modelled by mathematical descriptions of the interactions of individual components [17]. This system is often used to model the change in time and space of a concentration in chemistry or even the spread of biological populations. However, it can also be used in biology to model the number of tumour cells, where the diffusive term describes the random movement of the tumour cells. In general, the equation looks as follows:

$$\partial_t q(\bar{x},t) = \underbrace{\nabla\cdot(D\nabla q(\bar{x},t))}_{\text{Diffusion}} + \underbrace{R(q(\bar{x},t))}_{\text{Reaction}}. \tag{2.1}$$

In this equation, $q(\bar{x},t)$ is an unknown vector function and the equation is split into a diffusive and reactive part. D is the diffusion in each location and R contains the reactions. Several authors have already used and improved this model to describe tumour growth [17, 19, 20, 44, 45]. The models these authors have built are capable of incorporating patient-specific noninvasive imaging, MRI's, to determine the parameters in the model. In this specific application, the reaction-diffusion equations look as follows.

$$\frac{\partial N(\bar{x},t)}{\partial t} = \underbrace{\nabla\cdot(D\nabla N(\bar{x},t))}_{\text{Diffusion}} + \underbrace{k(\bar{x})N(\bar{x},t)\left(1-\frac{N(\bar{x},t)}{\theta}\right)}_{\text{Proliferation}}. \tag{2.2}$$

This equation models the spatio-temporal change of tumour cell number. In this case, $N(\bar{x},t)$ represents the number of tumour cells at position $\bar{x}$ and time t, where $\bar{x}$ is a two- or three-dimensional vector. $k(\bar{x})$ denotes the proliferation rate per voxel and θ is the carrying capacity, i.e. the maximum number of cells that fit into one voxel. A logistic growth function is used for the reaction. When regarding tumour growth, several different growth functions exist [32]. In the early stages, cell division is quicker, resulting in exponential growth. However, for later stages of tumour growth, this growth function is not realistic. Instead, a logistic growth function is found to be more realistic as it limits the growth of the tumour as more cells are present. This means the growth rate decreases linearly as the size of the tumour increases.

Additional expansions are made to make the model more realistic. Firstly, the apparent cell diffusion, D, which describes the random movement of the tumour cells, can be mechanically linked to surrounding breast tissue. This is done via the following equation:

$$D = D_0 e^{-\gamma\sigma_{vm}(\bar{x},t)}, \tag{2.3}$$

where $\sigma_{vm(\bar{x},t)}$ is the von Mises stress, γ is a coupling constant for the von Mises stress and D_0 is the diffusion of tumour cells in the absence of external stress. As can be seen from the equation, there is an inverse relationship between the von Mises stress and the diffusion coefficient. As the von Mises stress increases, the diffusion coefficient D decreases.

Additionally, a linear elastic, isotropic mechanical equilibrium is assumed between the tumour and its surrounding environment. The forces exerted by the tumour are assumed to be linear with the cellularity, shown in Equation 2.4. Here, λ is a coupling constant and G is shear modulus, $G = \frac{E}{2(1+\nu)}$ with E Young's modulus and ν Poisson's ratio. The Young's modulus relates to the stiffness of the surrounding tissue. The breast tissue consists mostly of adipose, fibroglandular and tumour tissue, with fibroglandular tissue being twice as stiff as adipose, fatty, tissue [45].

$$\nabla \cdot G\nabla\vec{u} + \nabla\frac{G}{1-2\nu}(\nabla \cdot \vec{u}) - \lambda\nabla N(\bar{x},t) = 0. \tag{2.4}$$

This equation shows the response of the displacement vector, $\vec{u}$, due to tumour cell growth. The left hand side represents the linear-elastic description of tissue displacement while the right hand side is the local body force which is generated by the tumour [15]. After solving this equation, the von Mises stress is calculated using the displacement vector and then used to update the diffusion coefficient. As the tumour grows, it imposes stress on the surrounding tissue, with stiffer tissues leading to higher stress. This, in turn, restricts the tumour's growth through stiffer tissues. Equations 2.2, 2.3 and 2.4 will be used in the model.

2.2.2. Overview Parameters

An overview of the parameters and variables which are present in the model can be seen in Table 2.1 and 2.2. For each parameter/variable, it is also shown whether they are taken from literature values or need to be calculated/calibrated per patient and what their assigned values are.

Variable	Description	Value
$N(\bar{x},t)$	Number of tumour cells in $\bar{x}$ at time t	Calculated from DWI-MRI [cells]
$D(\bar{x},t)$	Diffusion of tumour cells	Calculated [mm^2/day]
$\sigma_{vm}(\bar{x},t)$	Von Mises stress	Calculated from $\vec{u}(\bar{x},t)$ [kPa]
$\vec{u}(\bar{x},t)$	Displacement of tumour cells	Calculated [mm]
G	Shear Modulus	Calculated, $G = \frac{E}{2(1+\nu)}$ [kPa]

Table 2.1: Table with clarification on the variables and how their values are assigned.

2.2.3. Quantitative Imaging

In this thesis, noninvasive imaging is used to obtain the patient-specific parameters necessary for the model. In this case, Magnetic Resonance Imaging is used, MRI. Specifically, two different types of MRI scans are used, Diffusion Weighted Images (DWI-MRI) and Dynamic Contrast Enhanced (DCE-MRI). Both serve different purposes, DWI-MRI measures the random movement of water within the tissue, which can be linked to the number of tumour cells. DCE-MRI are MRI scans in which a contrast agent is administered to the patient after which a series of scans is made. This type of MRI scan is used by radiologists to determine the location and size of the tumour as it lights up due to the contrast agent. Both of these types of MRI scans are necessary for at least three different time points. One prior to starting chemotherapy, one during treatment and one at the conclusion of treatment, prior to surgery.

Parameter	Description	Value
D_0	Diffusion of tumour cells in absence of stress	Calibrated [mm^2/day]
$k(\bar{x})$	Proliferation rate of tumour cells	Calibrated [1/day]
θ	Carrying capacity of tumour cells in each voxel	Calculated [cells]
γ	Mechanical coupling coefficient for stress	Lit. value, 2×10^{-3} [1/kPa]
ν	Poisson ratio	Lit. value, 0.45
E	Young's modulus for adipose, fibroglandular, and tumour tissue	Lit. value, 2, 4 and 20 respectively [kPa]
λ	Coupling constant for the displacement of tumour cells	Lit. value, 2.5×10^{-3}

Table 2.2: Table with clarification on model parameters and how their values are assigned.

2.2.4. Determine Tumour Region of Interest

In order to determine the tumour cellularity, first, the tumour region of interest (ROI) needs to be established. For this, DCE-MRI data can be used to segment the tumour ROI. Several approaches for this exist. For example, Jarrett et al. (2018) determined the ROI by first calculating the difference between the average of the precontrast images and of three consecutive postcontrast images for each voxel. Then, the standard deviation of signal intensity of healthy tissue is calculated by using the average of the final six post contrast images of the normal-appearing tissue from the unaffected breast. Lastly, for each voxel within a manually drawn ROI, if the difference between the pre- and postcontrast image is greater than two times the calculated standard deviation from the healthy tissue, the voxel is considered to be part of the tumour.

On the other hand, Weis et al. (2013) determined the ROI of the tumour by comparing the difference between the average of pre- and postcontrast images for each voxel as well. If a voxel within a manually outlined ROI was exhibiting an 80% signal intensity increase between the pre-and postcontrast images, they were considered to be part of the tumour. This 80% threshold was chosen as this would provide the highest degree of correlation between the tumour volume at the time of surgery and tumour volume calculated by DCE-MRI.

Lastly, Jarrett et al. (2020) chose to use a fuzzy c-means-based clustering algorithm to determine the tumour ROI. In a fuzzy-based algorithm, the data points are divided into c different groups where the data point membership is no longer binary but can range from 0 to 1 and thus characterizes the degree of similarity between the data and the group. In this case, the algorithm divides the data points, voxels, into two groups, lesion and non-lesion and has been shown to be both effective and efficient [9].

Note that each of these three methods uses an already manually and conservatively outlined ROI before the algorithm proceeds to refine this to the tumour ROI. Also, the first and last scan in which the tumour is present should be known.

2.2.5. Tumour Cell Estimation

As discussed before, DWI-MRI provides a noninvasive measurement of the random movement, Brownian motion, of water in tissues which can then be quantified using the apparent diffusion coefficient (ADC). The free movement of water is hindered by cells and thus ADC is inversely correlated to tumour cellularity [1, 31]. To calculate the ADC values, the following equation can be used:

$$ADC = \frac{\sum_{i=x,y,z} \ln(S_0/S_i)/b_i}{3}, \tag{2.5}$$

where i is the diffusion weighting direction, b_i is the amount of diffusion applied to the sample, S_i is the signal intensity in presence of diffusion and S_0 is the signal intensity in the absence of diffusion. In general, multiple DWI-MRI scans are made with different diffusion directions and b-values. For instance, Philips uses the directions anterior-posterior (AP), feet-head (FH) and right-left (RL). For each direction, a scan is made. The ADC values can be found by fitting the signal intensities of each voxel from the images at the different b-values to Equation 2.5, using nonlinear least squares [47].

After this, the ADC values for voxels within the tumour ROI can be used to estimate the tumour cell number $N(\bar{x}, t)$ using the following equation:

$$N(\bar{x}, t) = \theta \left(\frac{ADC_w - ADC(\bar{x}, t)}{ADC_w - ADC_{min}} \right), \tag{2.6}$$

where ADC_w is the apparent diffusion coefficient of free water at $37°$C ($ADC_w = 3 \cdot 10^{-2}$ mm^2/s) and ADC_{min} is the minimum ADC value in a tumour voxel measured over time 1 and 2 [19, 44]. θ is the carrying capacity, i.e. the maximum number of tumour cells that fit into a voxel. To obtain θ, current models assume spherical tumour cells with a packing density of 0.7405 and a cell radius of 10 μm and so they arrive at a tumour cell volume of 4189μm^3. To find the carrying capacity, we divide the voxel volume by the tumour cell volume [1, 20, 44, 45].

2.2.6. Parameter Calibration

To predict patient-specific outcomes to treatment, patient-specific parameters are necessary. In the current model, the patient-specific parameters are the diffusion in absence of stress, D_0 and the proliferation rate per voxel, $k(\bar{x})$ which can be either positive or negative depending on cell proliferation or death respectively. As mentioned before, MRI scans from three different time points are needed for the model. This is for the calibration, as well as validation of the model. The data from the first two MRI scans, i.e. tumour cell distribution, is used to calibrate the model parameters using Levenberg-Marquardt nonlinear least squares [19, 20, 44, 45]. Using this, the sum of squared errors between the calculated cell number at time 2 and the observed cell number at time 2 is minimized.

2.3. Hybrid Models

Hybrid models combine both discrete and continuum techniques to bridge the cellular-scale to tumour-scale and may provide a more realistic coupling of biophysical processes [29, 43]. While discrete models are able to model the behaviour for individual cells, they are unable to do so for a large number of cells due to computational complexity. Conversely, continuum models allow for monitoring of larger clusters of cells yet fail to model cells on an individual scale. Though there are two types of lattices to choose from for the discrete cells, the continuous equations accounting for the chemical or physical fields are solved on a square, triangular or hexagonal grid [8]. Since both approaches have their benefits and limitations, hybrid modelling aims to combine both methods and use their best features, though more work is necessary to compete with the continuum results [29]. The goal is to create a discrete high resolution model while reducing computational intensity whenever possible.

For classical hybrid models, there are two types of continuum-discrete models [29]. The first approach represents tumours as the sum total of discrete elements (cells) and substrates (e.g. growth or therapy) are continuum variables. The second approach describes the tumour itself by both discrete and continuum components. This second approach provides the possibility of upscaling from cell-scale to tumour and even tissue scale which is not possible by using just discrete models.

In the last decade, hybrid models have started to combine two or more different mathematical frameworks. Continuous or discrete models were combined with concepts from other fields such as machine learning and fluid dynamics [8]. The different modelling frameworks can be found in Figure 2.1. In the classical hybrid model, physical laws determine the behaviour of the cells and it thus falls into the physics-based category. Other models can, for example, combine data-driven models with

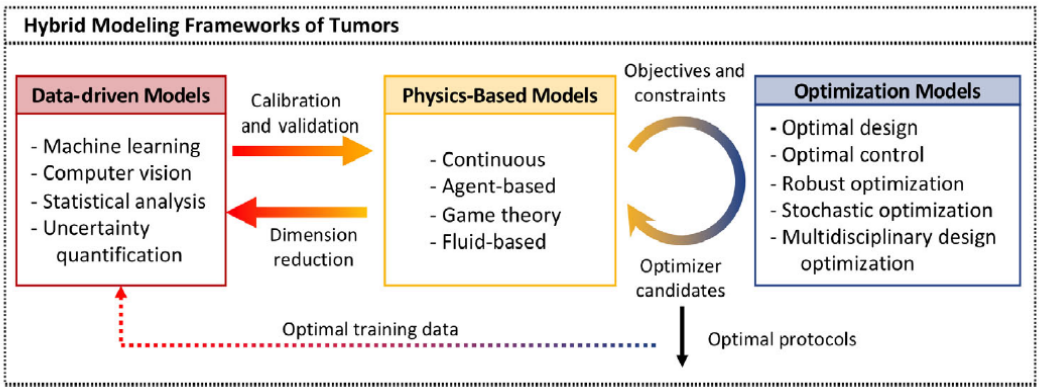

Figure 2.1: Hybrid modelling frameworks from Chamseddine and Rejniak (2020).

physics-based models. Data-driven models use statistical correlations to identify and find patterns in the underlying data and are often applied to medical imaging data [8]. One example of this is from Li et al. (2014), where image analysis algorithms are combined with a continuum mathematical model to determine whether changes in MRI scans after the first neoadjuvant chemotherapy could predict patients' response. In this study, an enhancement threshold was chosen to divide the MRI scans between responders and nonresponders. They used three continuous pharmacokinetic models to predict the tumour response and proceeded to use statistical analysis to calculate the prognostic capabilities of the parameters found.

2.4. Conclusion

Table 2.3 provides an overview of the different modelling approaches and lists the benefits and drawbacks of each method. Though discrete modelling is capable of investigating the tumour dynamics on an individual cellular scale, it is only able to do so for a limited number of cells due to computational costs. As such, it is unsuitable for the goal of this research as we wish to model the tumour response in its entirety. Hybrid modelling seems to be a relatively new approach with the goal to combine both discrete and continuum models and use only their advantages. It is able to be applied to both small- and large scales and could provide more realistic results. However, current literature is by far less extensively available than for continuum models. Additionally, sophisticated numerical techniques will be required and more model parameters will be necessary to model the individual cells which may have to be found invasively [29]. Continuum models are by far the most covered in literature for modelling tumour growth. Additionally, already several articles show promising results to combine the model with noninvasive imaging for patient-specific predictions [17, 19, 20, 45]. Though continuum models are unable to model individual cells, the capability to model larger-scale tumour dynamics is more desirable in the interest of this thesis. Therefore, the focus will lay on continuum models, specifically the reaction-diffusion equations described in the previous section.

Model Type	Characteristics
Discrete	• Autonomous cells, with a set of rules governing their behavior • Capable to investigate tumour dynamics at a single cell level and below • Limited to a comparably smaller scale due to prohibitive computational costs
Continuum	• Describing tumour tissue as a continuum medium • Capable to capture larger-scale volumetric tumour dynamics • Computational cost efficiency • Difficult to implement heterogeneous cell-cell and cell-environmental interaction, or molecular level dynamics
Hybrid	• Applicable to both small- and large scale models • Extensive numerical techniques required

Table 2.3: Benefits and drawbacks of different modelling types [43].

3

Data Preprocessing

In this chapter, the data preprocessing necessary for the implementation of the model will be discussed. Two different sets of data have been used. Prior to obtaining the data from Erasmus Medical Centre, data was collected from Cancer Imaging Archive from the QIN-Breast study [38].

3.1. Data Collection

As mentioned in the previous chapter, the data used for this research are Diffusion Weighted MRI scans (DWI-MRI) and Dynamic Contrast Enhanced MRI scans (DCE-MRI). Both types of scans are three-dimensional scans made of either one or both breasts of the patient and shall be used to initialize the model for each individual patient.

3.1.1. Data QIN-Breast

Since the Erasmus MC data was not available at the start of this research, first data from the QIN-Breast study was used [38]. The data from this study is from between 1987 and 1996. There were 68 patients in total, though for some only CT and PET scans were performed. It is also important to note that the specifications of the patients' tumour are unknown, i.e. we do not know whether these are HER2+ patients or not. Unfortunately, most patients only had MRI scans of two time points. Additionally, no information on the location of the tumour(s) was given, only whether the patient achieved pCR or not. In the end, patient 59 was taken, as this patient seemed to have one of the more distinguishable tumours. The scans of this patient date from 1993 and only 2 time points were available. It is also known that this patient did not achieve pCR. In this study, the DWI-MRI scans have a resolution of 144 x 144 x 12 with a voxel size of 1.333 mm x 1.333 mm x 5 mm and were made with b-values 0, 50 and 600 s/mm^2. The DCE-MRI scans have an acquisition matrix of 192 x 192 x 20 with the same voxel size of 1.333 mm x 1.333 mm x 5 mm. In one MRI scan session, 25 DCE-MRI scans are made of the breast over the course of about 7 minutes. The first 3 scans are classed as precontrast scans, and the latter 22 are postcontrast scans, where the contrast agent has been administered to the patient. Both scans are made over the sagittal axis and only the breast containing the tumour(s) is scanned.

Due to the third scan being unavailable, the data of this study will be used to establish the preprocessing pipeline and test the implementation of the model. The data from Erasmus shall be used to evaluate the performance of the model.

3.1.2. Data Erasmus MC

The data provided by Erasmus Medical Centre consists of 4 individual patients having one or multiple HER2+ tumours. For each of these patients, 3 time points with scans are given which ranged

between April 2020 and February 2021. All data has been anonymised, so a.o. the age, name and ethnicity of the patients are unknown. Since there are four patients provided by Erasmus MC, these will be named Patient001 to Patient004, respectively. The first scans from Patient002 were taken in a different hospital. As such, the dimensions of the acquisition matrix as well as the shape of the breast are different than the ones taken at Erasmus MC. In Table 3.1, an outline is made of the different matrix dimensions as well as voxel sizes. Due to the differences in voxel sizes and resolution, additional processing is needed compared to the data from QIN-Breast. All patients have a residual tumour at time 3. In this data set, the DWI-MRI scans have been made with b-values 50 and 800 s/mm^2 and all scans have been made over the axial plane where both breasts can be seen.

Additionally, Patient001 and Patient002 have multiple tumours. Patient002 has five separate tumours at MRI scan 1, but only one tumour remains from scan 2 onward. The tumours of Patient003 and Patient004 both have a very uneven shape compared to Patient001 and Patient002. Since Patient004's tumour had a very uneven shape and every DCE-MRI scan had different dimensions, it was decided to leave this patient out of this research. After registration and further preprocessing, it would have been difficult to confidently determine the tumour's size and shape which makes this patient not very suitable to test the model with.

Time	Type	Patient001	Patient002	Patient003	Patient004
Time 1	DCE Dimensions	512 x 512 x 120	448 x 448 x 160	512 x 512 x 120	512 x 512 x 120
	Voxel Spacing (mm)	0.66 x 0.66 x 1.6	0.8 x 0.8 x 0.9	0.66 x 0.66 x 1.6	0.7 x 0.7 x 1.6
	DWI Dimensions	256 x 256 x 32	116 x 190 x 34	256 x 256 x 32	256 x 256 x 32
	Voxel Spacing (mm)	1.4 x 1.4 x 6.5	1.89 x 1.89 x 4.8	1.4 x 1.4 x 6.5	1.4 x 1.4 x 6.5
Time 2	DCE Dimensions	512 x 512 x 120	512 x 512 x 86	512 x 512 x 120	512 x 512 x 86
	Voxel Spacing (mm)	0.66 x 0.66 x 1.6	0.66 x 0.66 x 2.2	0.66 x 0.66 x 1.6	0.6 x 0.66 x 2.2
	DWI Dimensions	256 x 256 x 32	256 x 256 x 32	256 x 256 x 32	256 x 256 x 32
	Voxel Spacing (mm)	1.4 x 1.4 x 6.5	1.4 x 1.4 x 6.5	1.4 x 1.4 x 6.5	1.4 x 1.4 x 6.5
Time 3	DCE Dimensions	512 x 512 x 86	512 x 512 x 86	512 x 512 x 86	512 x 512 x 90
	Voxel Spacing (mm)	0.66 x 0.66 x 2.2	0.66 x 0.66 x 2.2	0.66 x 0.66 x 2.2	0.7 x 0.7 x 2.2
	DWI Dimensions	256 x 256 x 32	256 x 256 x 32	256 x 256 x 32	256 x 256 x 32
	Voxel Spacing (mm)	1.4 x 1.4 x 6.5	1.4 x 1.4 x 6.5	1.4 x 1.4 x 6.5	1.4 x 1.4 x 6.5

Table 3.1: Dimensions and voxel sizes of the different types of MRI scans provided by Erasmus MC.

3.2. Image Registration

At different time points, an MRI scan has been made of the patient to assess the tumour. At every time point, the patient may lie a little differently in the MRI scanner, causing the breast to not always

be aligned correctly. In order to accurately assess the size and shape of the tumour, it is important for the scans to be registered. Image registration is the process of transforming the data from one set of MRI scans to the coordinate system of another set of MRI scans. Not only do we have sets of MRI scans at different time points, but also the different sets of MRI scans, i.e. DWI-MRI and DCE-MRI, also need to be registered. Due to the DCE-MRI scans having the greatest resolution and area of the breast scanned, this scan will be used as our reference coordinate system. However, as can be seen in Table 3.1, the dimensions and voxel sizes of the patient MRI scans may differ per time point as well as between the different types of scans. Therefore, the data will first need to be upscaled such that they have the same number of slices. For the data from QIN-breast, this step is unnecessary as both types of scans have the same voxel spacing.

3.2.1. Upscaling

Upscaling will be used to make sure that all time points as well as different MRI scans have the same number of slices in the z-direction. A zero-padded inverse Fast Fourier Transform, FFT, is used to resample the data. First, the data along the axis is transformed into the frequency domain. Then, the inverse FFT is taken where the sample size is taken as the upscaled number, i.e. time 3 for Patient001 will be upscaled to 120 slices. By doing this, all data is preserved when compared to downscaling. Additionally, it is important to use the correct voxel spacing for the newly upscaled image. From Table 3.1, it can be seen that the diffusion weighted images of the patients have (mostly) 32 slices, which all have a voxel spacing of 6.5 mm. When upscaled, the voxel sizes for the newly made 120 slices will be $\frac{6.5}{120/32} = 1.73$ mm instead of the voxel spacing of 1.6 mm of the DCE images. Taking this into account will be important for the registration. The following observation is made, Patient001 and Patient003 need the least amount of upscaling. Only the DCE-MRI images from time 3 need to be upscaled along with the DWI-MRI images for every time point. Patient002 and Patient004 prove to be somewhat of a challenge. Patient002's first scan was made in a different hospital. As such, it has very different dimensions and the diffusion weighted image is rectangular. Again, we only upscale along the z-axis and let the registration algorithm perform the rest.

3.2.2. Registration

In total, two different types of registration will be carried out, intra-scan and inter-scan registration. To do intra-scan registration, registration within one visit, the DWI-MRI will be registered to their respective DCE-MRI. The DWI-MRI can be seen in Figure 3.1, where we see that the DWI image looks slightly zoomed in to the DCE image. In this case, rigid registration is used as we only use translation and rotation to register the moving image onto the fixed image. The registration software which has been used is ITKElastix in Python [23, 36]. This powerful package already comes with ready to use parameter maps for the registration. In our case, the default rigid registration is used. For inter-scan registration, registration across visits, we use the default nonrigid registration. Nonrigid registration accounts also for the change in the shape of the breast, which is necessary as the patient may lie a little differently in the scanner on the next visit. The default bspline parameter map has been used for the nonrigid registration.

For the data from QIN-breast, some additional steps were taken before the registration could be carried out.

- The images are first sorted into their respective categories, e.g. timesteps or different b-values. For instance, for the DCE scans, 500 images were available. These 500 images were actually 25 scans over different time steps with each scan having 20 slices of the breast. As such, 25 3D breast images could be using tools such as ItkSnap or Slicer3D.
- We made sure that for the 3D breasts, the same part of the breast are scanned DCE and DWI images. In our case, the DWI images only had 12 slices of 5 mm instead of 20 of 5 mm. So,

the DWI-MRI scans were missing some of the parts of the breast. So, for the DCE-MRI, we removed the 8 slices which were not present in the DWI images.

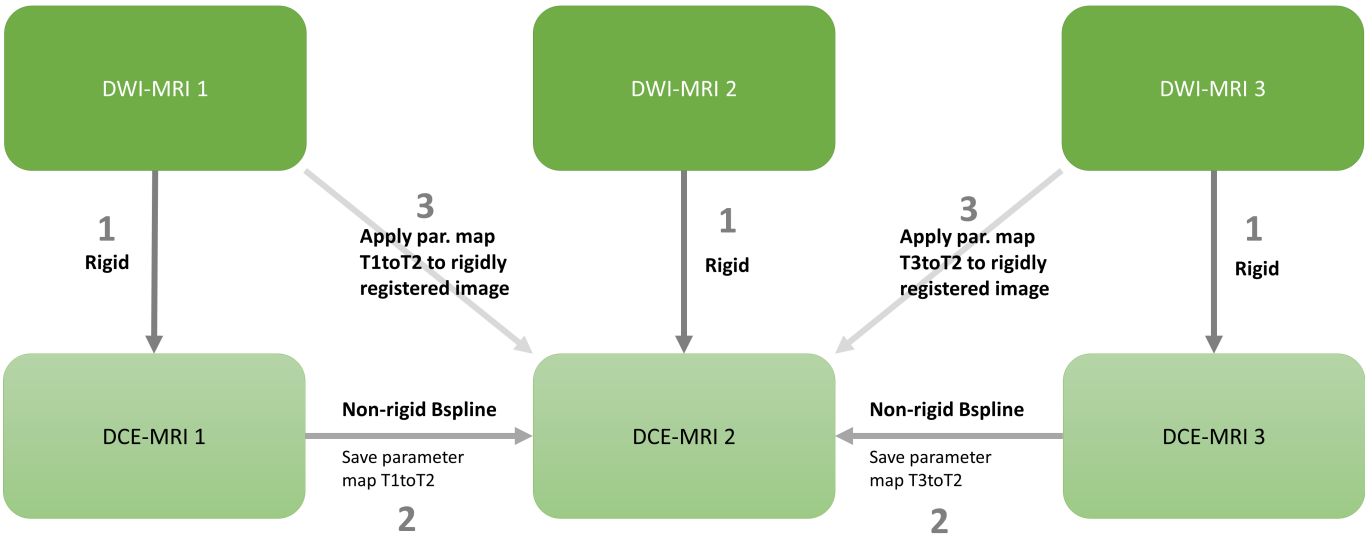

Figure 3.1: Pipeline used to register the MRI scans. Step 1: the DWI-MRI scans are registered rigidly to their respective DCE-MRI. Step 2: DCE-MRI scans are registered non-rigidly to a fixed reference time, scan 2 in this case. Step 3: Register the image result from step 1 non-rigidly using the same parameter map as in step 2.

In Figure 3.1, the pipeline for registration is shown. In step 1, the DWI-MRI scans are registered rigidly to their respective DCE-MRI scans and saved. Then, in step 2, the DCE-MRI scans are registered non-rigidly to the reference DCE-MRI. In this case, DCE-MRI scan 2 is taken as the reference MRI scan. The parameter maps for these registrations are saved which are then used on the already rigidly registered DWI-MRI scans in step 3. By doing this, we make sure that the DWI-MRI scans will have the same nonrigid registration as the DCE-MRI scans and thus have the same domain and shape.

The results of the registrations of the QIN-breast data can be found in Figure 3.2 and of the Erasmus data (of Patient001) in Figure 3.3. Both of these figures show the nonrigid bspline registration on top and the rigid registration on the bottom. The moving image is registered to the fixed image, where the fixed image is the reference DCE-MRI scan. The result image shows the result after registration. In these figures, we can see how the nonrigid registration changes the shape of the breast to make the moving image look more like the fixed image.

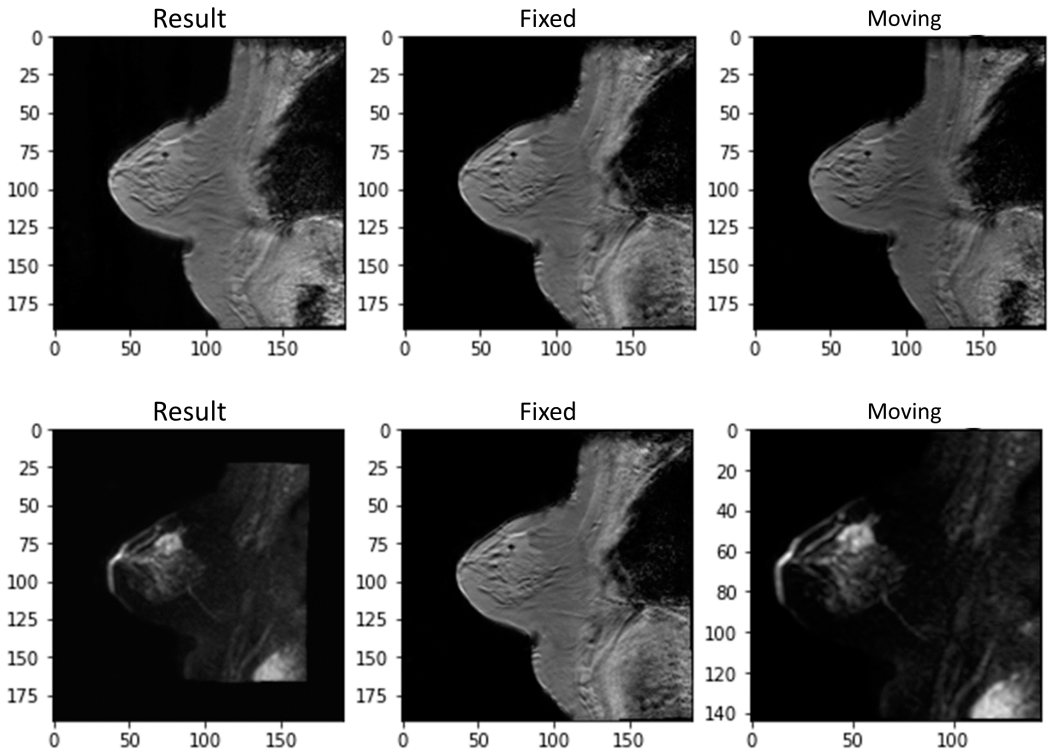

Figure 3.2: Registration for QIN-Breast study data. Top images show non-rigid bspline registration, bottom three images are registered rigidly. The moving image is registered to the fixed image. The resulting image shows the result after registration. The breast in the fixed image and result image have the same shape.

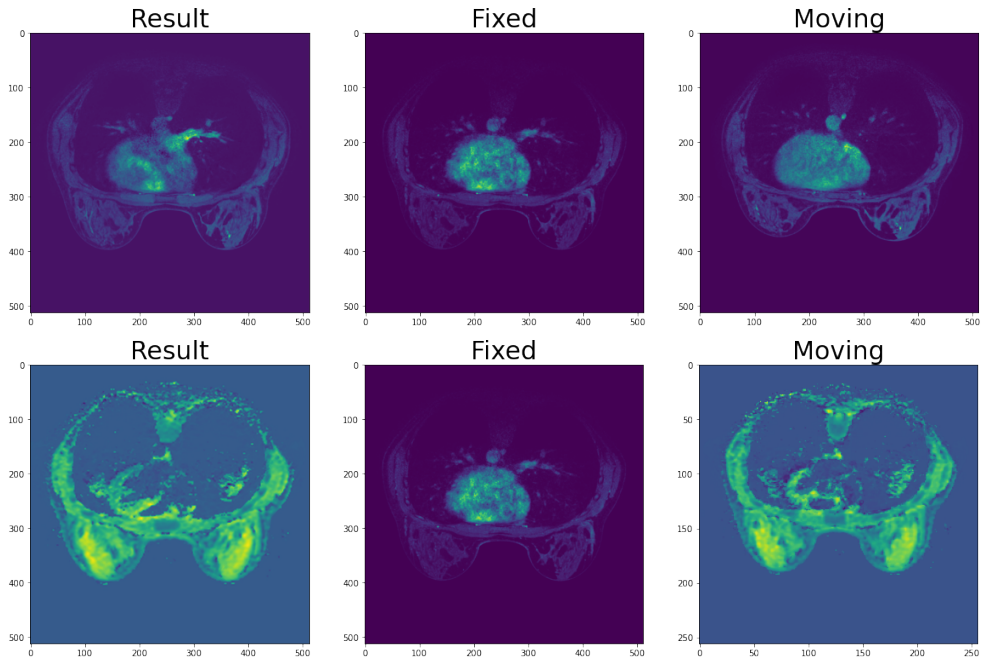

Figure 3.3: Registration for Erasmus MC Patient001 data. Top images show non-rigid bspline registration, bottom three images are registered rigidly. The moving image is registered to the fixed image. The resulting image shows the result after registration. The breast in the fixed image and result image have the same shape.

To check whether the resulted registered image is indeed correct, the checkerboard tool can

be used to see the differences between the images. If the registration is carried out successfully, the registered images should overlap (almost) exactly with the original image, as can be seen in Figure 3.4. In this figure, the left image shows the difference in the image before registration and its reference image. As can be seen, the shape of the breast does not connect very well. The right image shows the checkerboard performed on the registered image and the reference (fixed) image. Now, the shape of the breast connects almost seamlessly and so registration has been carried out correctly.

Figure 3.4: Checkerboard tool used between fixed and result image to ascertain whether the registration is carried out correctly. The left image shows the difference before rigid registration is carried out, the right image is checkerboard performed after registration.

Naturally, several more parametermaps exist which might be even better suited for this particular application. Due to time constraints, we were unable to fully experiment and research the best way to perform image registration for the nonrigid case as the tumour within the breast could be distorted incorrectly.

3.3. Region Growing

From the MRI scans, a three-dimensional matrix is obtained which contains all the voxel intensities. However, part of this three-dimensional matrix is not of importance for the model as this is merely the background and not the breast. Therefore, it is necessary to make a distinction between which voxels are within the breast and which voxels are in the background. The technique chosen to make this distinction is region growing. Region growing is a simple image segmentation method where a seed point is taken from which its surrounding neighbours are connected whenever the difference in voxel intensity between the two points is less than a certain threshold [12]. Iteratively, the region is grown until the neighbours no longer meet the threshold. The threshold has been chosen as the highest value for which the breast is correctly outlined. The DCE-MRI scans are used for this as they have the best distinction between breast and background, compared to the DWI-MRI. The second step is to take the largest connected component as the chosen domain of the model as seen in Figure 3.5. This ensures that local outliers in the background are filtered. In the end, a three-dimensional region of the breast remains.

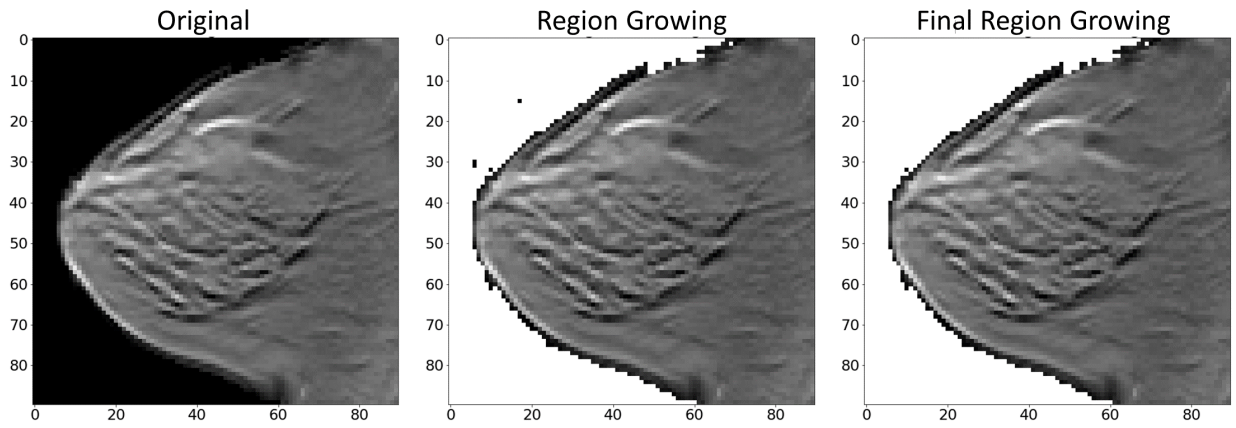

Figure 3.5: Finding the domain of the breast from DCE-MRI using region growing. On the left, the original image is shown. The middle image shows the result after initial region growing. Some outliers are still present. The image on the right shows the final domain after the largest connected component has been taken.

In Figure 3.5, the results can be found from Patient0059 from the QIN-breast study. Note that some spots may look like they are not connected to the breast after we take the largest connected component. While they may not be connected in the x- and y-plane, they are connected in the z-plane. In Figure 3.6, the three-dimensional outline of the breast is shown as well as a resulting slice from Patient001.

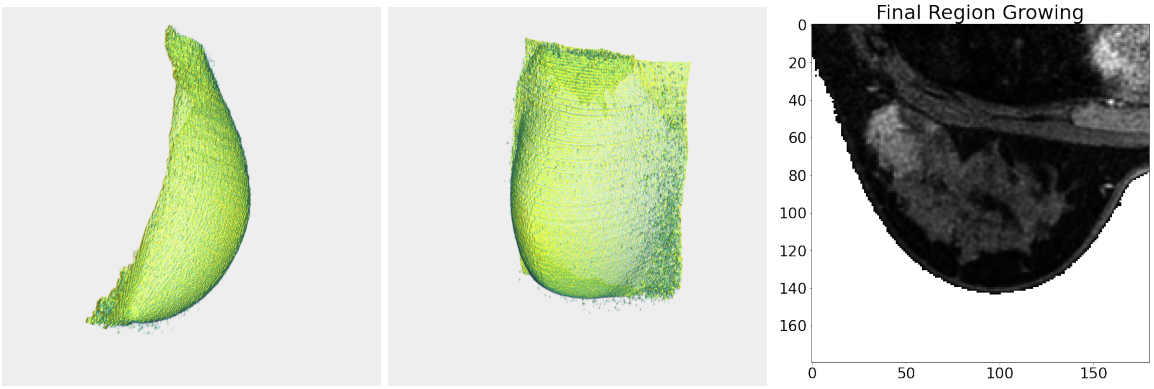

Figure 3.6: 3-dimensional shape of the breast of Patient001 is shown on the left and middle image. The image on the right shows one of the slices with the final breast domain obtained using region growing.

3.4. Segmentation of the Tumour

The next step is to find the actual tumour within the breast. Two different approaches have been taken for this task, though several more exist as explained in section 2.2.4. For the data from the QIN-Breast study, simple thresholding was used to segment the tumour since this was the easiest method to implement. In this study, several dynamic contrast enhanced images are made over a time period in which a contrast agent is given to the patient, in this case gadolinium. In this case, for each slice, 25 images were made. From these 25 different slices, the first three were precontrast images and the latter 22 images were postcontrast images. The tumour lights up due to the contrast agent, so by taking a look at the difference in signal intensity between the two types of images the tumour can be segmented. An average 3D image is made of the three precontrast images as well as the 22 postcontrast images. Then, a region of interest is manually determined in which the signal intensities are compared. Within this region of interest, the signal intensities between the averaged

precontrast and postcontrast scans are compared. A threshold is chosen, in this case if a voxel has increased 30% or more in signal intensity, it is classified as tumour tissue. In the end, the largest connected component is chosen as the tumour region of interest. The result of this can be seen in Figure 3.7, where the fifth slice within the breast of Patient0059 is shown.

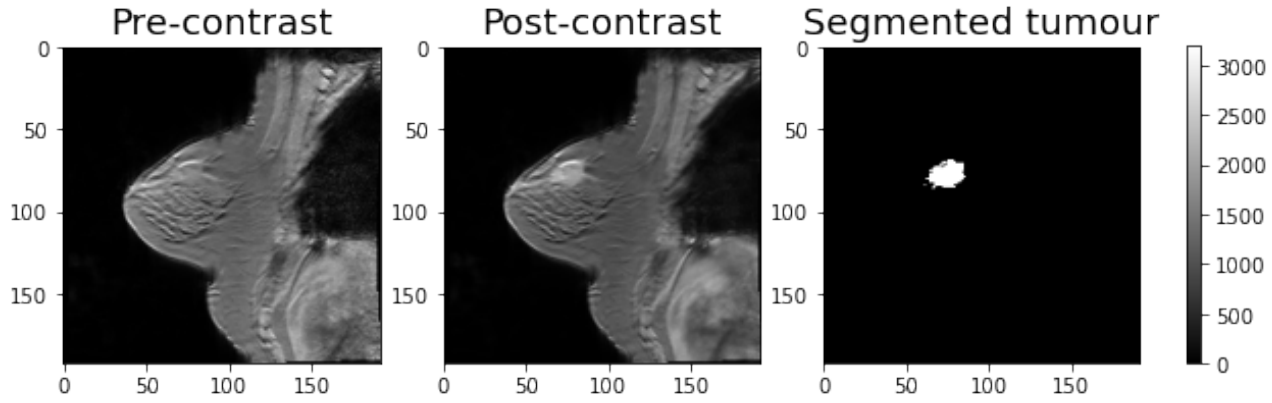

Figure 3.7: Segmantation of the tumour of Patient0059. The precontrast (left) and postcontrast (middle) images are made. Simple thresholding is used between the pixel intensities of the precontrast and postcontrast image. The resulting segmented tumour is shown on the right.

The second approach which has been taken for the segmentation of the tumours of the Erasmus MC data is segmentation done by a radiologist. Because there was only data available of 4 patients, the breast cancer radiologist, dr. A.I.M. Obdeijn was kindly willing to help in this task. By using the pathological rapport available of the patients as well as other contrasting MRI scans, the tumours of the 4 patients have been segmented. For this, the tool ITK-Snap was used to manually draw around the lesion. The results of this approach can be seen in Figure 3.8.

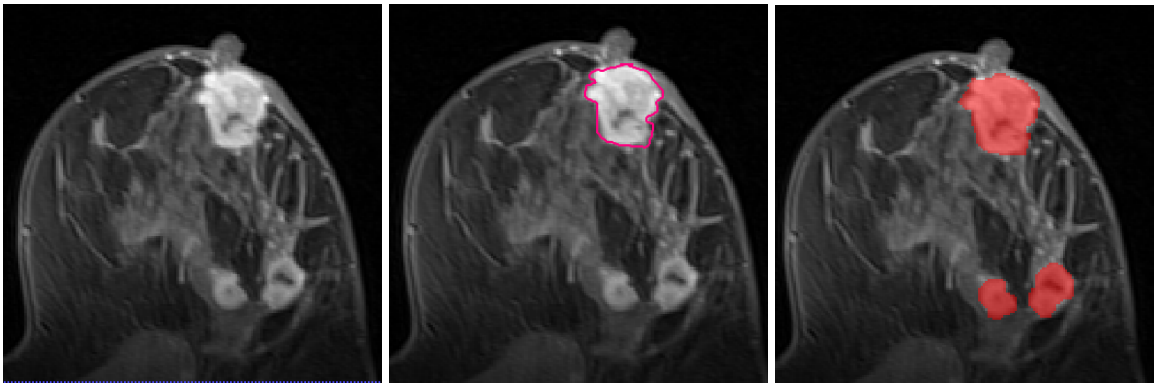

Figure 3.8: Segmentation of the tumours of Patient002 done by a radiologist. Using ITK-Snap, a line is drawn manually around the tumour(s) to segment them on each slice.

Naturally, this approach is far more reliable in determining the actual location, size and shape of the tumour, though it is important to note that some voxels may still be falsely in/excluded. Additionally, only some slices were segmented by the radiologist, for the remaining slices, ITK-Snap's tool of interpolation between slices was used.

3.5. ADC Values and Number of Tumour Cells

Now that the segmented tumour has been determined, it is important to know how many tumour cells are actually within the tumour. This is both used to initialize, as well as validate the model.

In order to calculate the number of tumour cells, first the apparent diffusion coefficient needs to be determined. The apparent diffusion coefficient is a measure of the magnitude of diffusion of water molecules within tissue and can be related to the number of tumour cells within tissue, via Equation (2.6). The ADC values can be calculated in each voxel using the diffusion weighted scans, DWI-MRI. The previously obtained tumour segmentation is used to calculate the ADC values within the tumour. Note that the registered DWI-MRI are used in this case to ensure that the ADC values are indeed taken from within the tumour. To calculate the ADC values, the b-value needs to be known. The higher the b-value, the stronger the diffusion effects are. For the data obtained from the QIN-Breast study, the MRI scans are made with b-values 0, 50 and 600 for each patient. Using the following equation, the apparent diffusion coefficients have been calculated:

$$S_i = S_0 \exp(-ADC \cdot b_i),$$

where S_i is the signal intensity in each voxel when there is diffusion imparted on the sample and b_i is either 50 or 600. S_0 is the signal intensity in the absence of diffusion, i.e. when the b-value is zero. This equation has been used instead of Equation (2.5) since this data contains a scan with the averaged signal intensities of the three diffusion directions. Using nonlinear least squares regression, the data is fit to obtain the ADC values. For the data from Erasmus MC, the ADC maps have already been made by the MRI scanner and did not need to be calculated. In Figure 3.9, the obtained ADC values of Patient001 at time 1 can be seen.

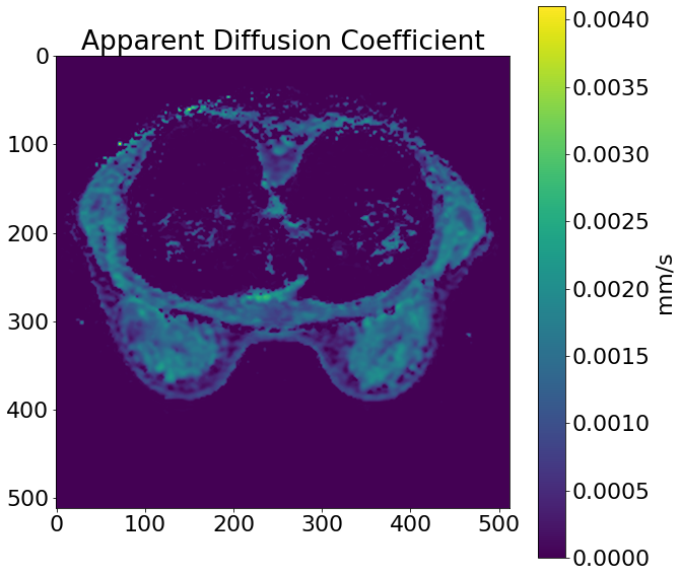

Figure 3.9: Apparent diffusion coefficients of Patient001.

Now that the ADC values are known, these can be related to the number of tumour cells in each voxel, via Equation (2.6). The higher the ADC value is, the less tumour cells are present. First, θ needs to be established, which is the carrying capacity of a voxel, i.e. the maximum number of tumour cells within a voxel. For this, a spherical packing density of 0.7405 is assumed and a nominal tumour cell radius of 10 μm, as was done in literature [19, 20, 44, 45]. For the QIN-Breast data, this leads to the following carrying capacity:

$$\theta = \frac{\text{voxel volume} \cdot \text{packing density}}{\text{tumour cell volume}} = \frac{(1.333 \cdot 1.333 \cdot 5) \cdot 0.7405}{\frac{4}{3}\pi(0.01)^3} \approx 1.571 \cdot 10^6 \text{ cells.}$$

Note that the voxel volume for the Erasmus MC data is different, resulting in $\theta \approx 1.247 \cdot 10^5$ cells for Patient001 and Patient003 and $\theta \approx 1.715 \cdot 10^5$ cells for Patient002. Next, ADC_{min} will need to

be calculated. This will be taken as the minimum ADC values of time 1 and time 2 for each patient. The calculated tumour cells can be observed in Figure 3.10, where also a three-dimensional image of the segmented tumour is shown.

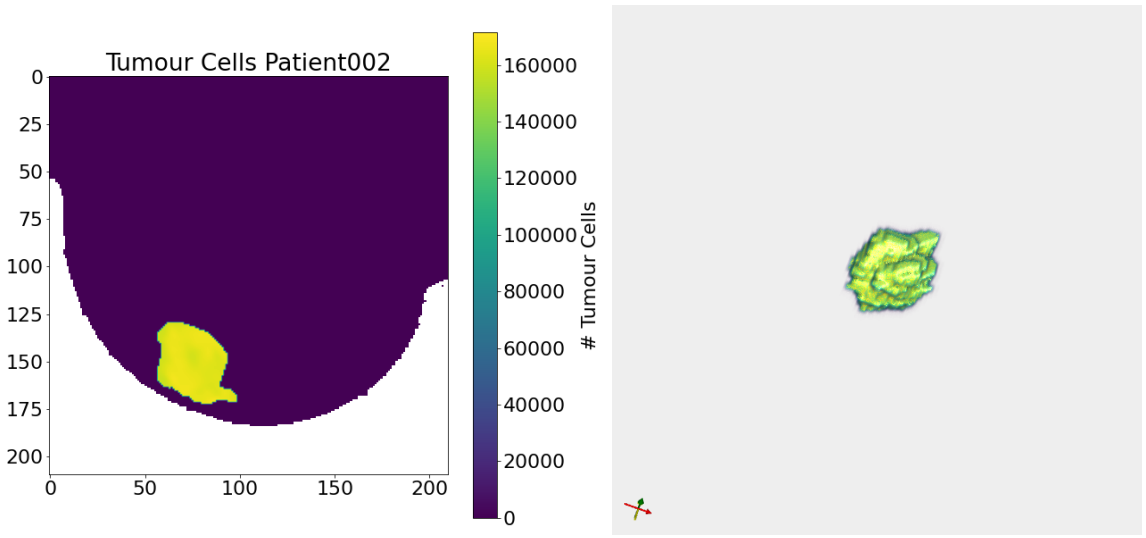

Figure 3.10: Calculated number of tumour cells of Patient 2 (left) along with the three dimensional tumour (right).

3.6. Segmentation of Breast Tissue

The majority of a female breast is made up of fibroglandular and fatty (adipose) tissue. Fibroglandular tissue is a mixture of the connective tissue (fibrous) and the part that produces milk, lobes (glandular) [33]. Each patient has her own individual composition of these two types of tissues. To include the effects of the tissue surrounding the tumour, the adipose and fibroglandular tissue need to be segmented.

The segmentation into adipose and fibroglandular tissue has only been done for the patients from Erasmus MC. The DCE-MRI scans have been used as the adipose and fibroglandular tissue are easily distinguishable here. Three different options have been investigated to approach this. Using a simple threshold above all voxel intensities which are higher would be classified as fibroglandular tissue and the lower voxel intensities were classified as adipose tissue. Another approach is to first use (adaptive) histogram equalization on the data after which this threshold is chosen.

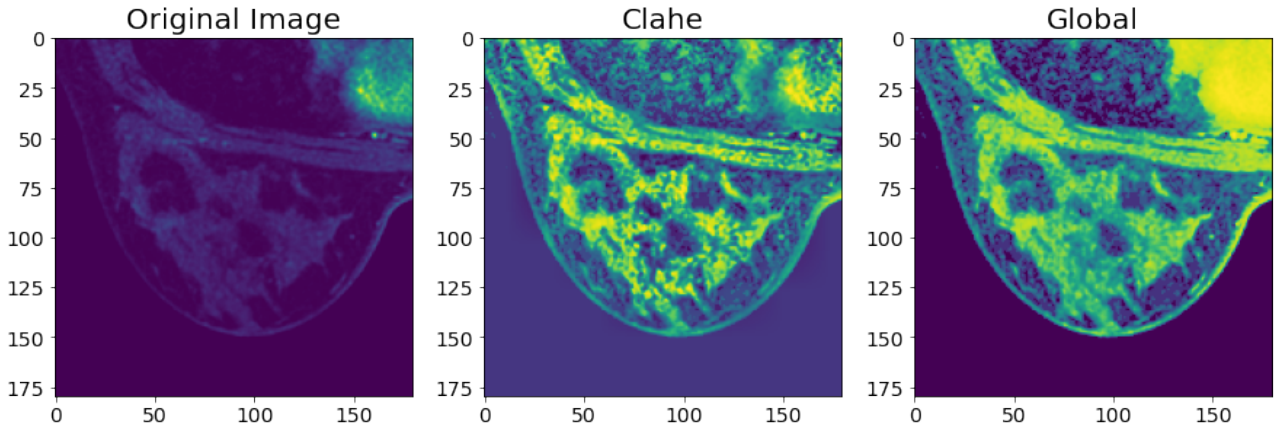

Figure 3.11: Original image (left) along with the result after applying two different kinds of histogram equalization. The middle image is after applying Contrast Limited Adaptive Histogram Equalization (CLAHE), the right image is after global histogram equalization.

In Figure 3.11 the results can be seen how the image looks after Contrast Limited Adaptive Histogram Equalization (CLAHE) and global histogram equalization. Comparing the results of the found domain for both fibroglandular and adipose tissue after these image processing tools, global histogram equalization provided the most satisfactory results. Additionally, the tumour region of interest was inserted into the domain to provide also the stiffness for the tumour tissue.

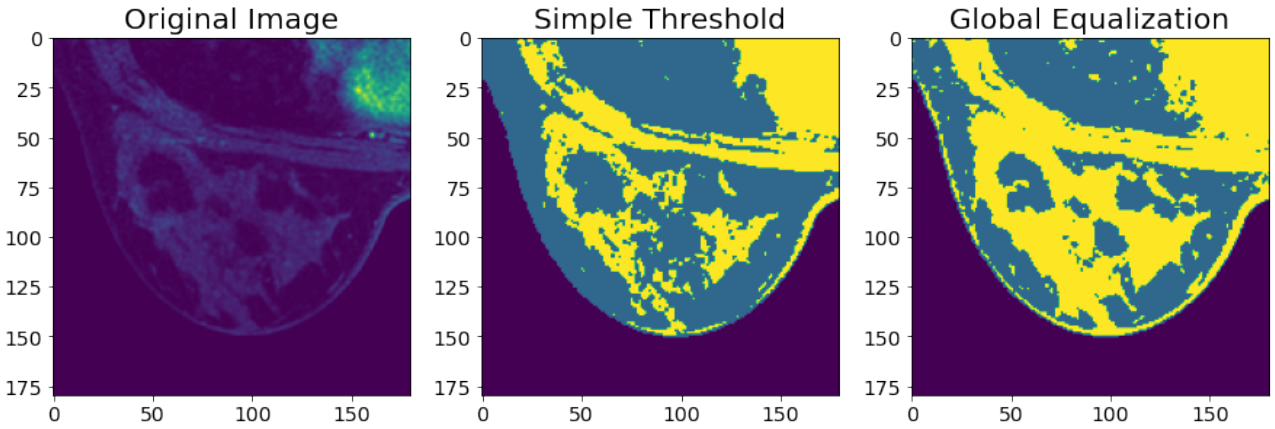

Figure 3.12: Original image (left) along with the segmented tissue into adipose and fibroglandular tissue. The middle image is made using simple thresholding on the original image, the right image is made using thresholding after global histogram equalization. The yellow areas are classed as fibroglandular tissue and the blue is adipose tissue.

The original image along with the segmentation using a simple threshold and thresholding after applying global histogram equalization can be observed in Figure 3.12. The two segmented images show the fibroglandular tissue in yellow and the adipose tissue in blue. Comparing the results to the original image, the global equalization approach shows a more refined segmentation of the tissues. The incorporation of the stiffness of the tissue will inhibit the growth of the tumour more realistically, i.e. the tumour can spread more easily through less stiff material such as adipose tissue. It is known that fibroglandular tissue is twice as stiff as adipose tissue [45].

3.7. Downsampling

One of the things that need to be taken into account is computational complexity. Most of the scans of Erasmus MC are known to have a resolution of 512 x 512 x 120, resulting in more than 31 million voxels within the whole domain. Fortunately, we can reduce this domain quite a bit. Firstly, some parts of the scan might not be of much interest to the model, such as the other (healthy) breast or parts of the patient's torso. To reduce computation time, some of these parts can be left out. An additional technique to reduce computation time will be downsampling. This technique reduces the number of voxels within the domain by combining two or more of its neighbours together. Using downsampling instead of zooming in further on the scan will preserve the overall shape and boundaries of the breast which will be important in the model calculations. By downsampling with a factor 3 along with zooming in on the breast, we can reduce the number of voxels in the domain from one 2-dimensional slice from approximately 260,000 to just 3,600 which can be seen in Figure 3.13.

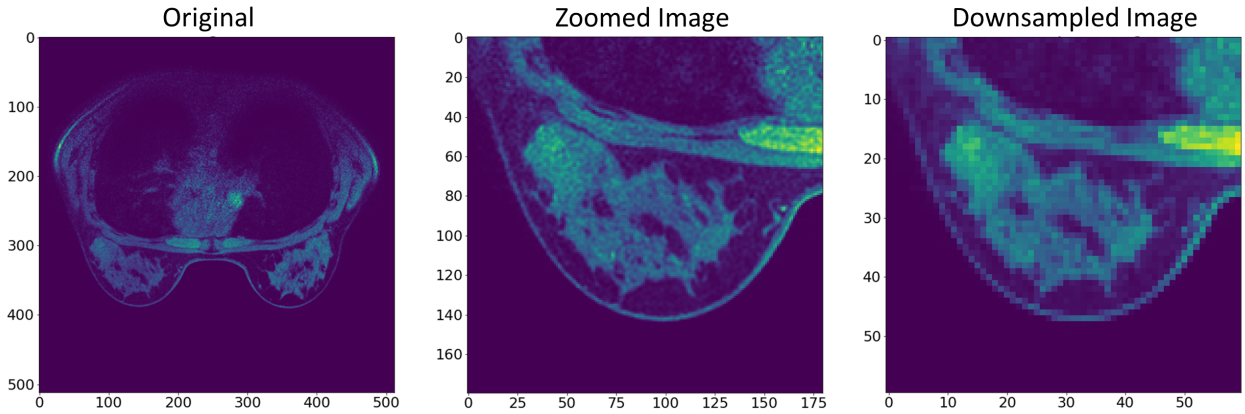

Figure 3.13: The original image (left) along with the zoomed domain of the breast which contains the tumour (middle). Downsampling the zoomed image by a factor 3 results in the downsampled image (right) which has a dimension of 60 by 60 compared to the original image which had a dimension of 512 by 512.

By following this preprocessing pipeline, the necessary information can be extracted from the MRI scans. Obtaining the domain, tumour cell number and tissue segmentations means that the model can now be implemented.

4

Model Implementation

Now that the data has been preprocessed and all necessary information for the model has been extracted, the model implementation is next. In this chapter, the model will be implemented in several stages. Moreover, the parameter calibration will be discussed which will need to be done for each individual patient. Although preprocessing was done in three dimensions, the model was implemented in only two. This was mainly done to reduce computation time. The model explained in Chapter 2 has a couple of different stages. First, the reaction-diffusion shall be implemented and can be tested on its own. Then, the incorporation of the linear elasticity of the surrounding tissue shall be tested to see whether this has a positive effect on the model's predictive capabilities.

4.1. Reaction-Diffusion

The two-dimensional reaction-diffusion equation is as follows:

$$\frac{\partial N(x,y,t)}{\partial t} = \nabla(D\nabla N(x,y,t)) + k(x,y)N(x,y,t)\left(1 - \frac{N(x,y,t)}{\theta}\right), \tag{4.1}$$

where $N(x,y,t)$ is the number of tumour cells in location (x,y) and time t. θ is calculated using the approach discussed in section 3.5 [20]. The other unknown parameters are the patient-specific parameters D_0 and $k(x,y)$ which need to be calibrated, more on that in section 4.3. For this equation, homogeneous Neumann boundary conditions are imposed, i.e. the equation has no diffusive flux at the boundary of the breast [19, 44, 45].

To approximate the continuous variables, discretizations of the spatial and temporal variables are used. For the discretization of the spatial parameters, we can choose between Finite Difference Method (FDM), Finite Element Method (FEM), or Finite Volume Method (FVM). In literature, mostly FDM and FEM have been used and in this thesis, we have chosen for the FDM approach since we already have a nicely shaped square grid in two dimensions [42].

For the time integration method, also several options are available. Most literature uses a fully explicit time integration method, though implicit schemes such as Crank-Nicholson may also be used [15, 19, 20, 45]. The main advantage of an explicit method is simplicity of implementation. However, the method is not unconditionally stable, so the time step Δt is bounded. This could lead to a small time step, which means more computations are needed to propagate the model forward in time. For now, we have chosen to use the fully explicit time integration method, Forward Euler because of its simplicity.

For the discretization of Equation (4.1), we have thus chosen to use a Forward in Time, Central in Space (FTCS) discretization. We use the conservative scheme instead of the non-conservative scheme due to provable stability, as seen in the next section 4.1.1 [25]. The discretization is carried

out as follows:

$$\begin{aligned}\frac{N_{i,j}^{n+1}-N_{i,j}^{n}}{\Delta t} &= \frac{1}{2}(\partial_x(D_{i,j}\bar{\partial}_x N_{i,j}^n)+\bar{\partial}_x(D_{i,j}\partial_x N_{i,j}^n))+\frac{1}{2}(\partial_y(D_{i,j}\bar{\partial}_y N_{i,j}^n)+\bar{\partial}_y(D_{i,j}\partial_y N_{i,j}^n))\\ &\quad + k_{i,j}N_{i,j}^n\left(1-\frac{N_{i,j}^n}{\theta}\right).\end{aligned} \tag{4.2}$$

Where we use the notation $D_{i,j} = D(x_i, y_j)$, $k_{i,j} = k(x_i, y_j)$ and $N_{i,j}^n = N(x_i, y_j, t_n)$. We have $i = 0, \ldots, n_x$ and $j = 0, \ldots, n_y$ with n_x and n_y the dimensions of the matrix and $n = 0, \ldots, T$ with T the total number of timesteps. Furthermore, we use that

$$\partial_x N_{i,j} = \frac{N_{i+1,j}-N_{i,j}}{\Delta x}, \qquad \bar{\partial}_x N_{i,j} = \frac{N_{i,j}-N_{i-1,j}}{\Delta x}.$$

Now, we can write the terms in Equation (4.2) as follows:

$$\begin{aligned}\frac{1}{2}(\partial_x(D_{i,j}\bar{\partial}_x N_{i,j})+\bar{\partial}_x(D_{i,j}\partial_x N_{i,j})) &= \frac{1}{2}\left(\partial_x\left(D_{i,j}\frac{N_{i,j}-N_{i-1,j}}{\Delta x}\right)+\bar{\partial}_x\left(D_{i,j}\frac{N_{i+1,j}-N_{i,j}}{\Delta x}\right)\right),\\ &= \frac{1}{2\Delta x^2}\Big[D_{i+1,j}(N_{i+1,j}-N_{i,j})-D_{i,j}(N_{i,j}-N_{i-1,j})\\ &\quad + D_{i,j}(N_{i+1,j}-N_{i,j})-D_{i-1,j}(N_{i,j}-N_{i-1,j})\Big],\\ &= \frac{1}{2\Delta x^2}\Big[(D_{i-1,j}+D_{i,j})N_{i-1,j}-(D_{i-1,j}+2D_{i,j}+D_{i+1,j})N_{i,j}\\ &\quad + (D_{i,j}+D_{i+1,j})N_{i+1,j}\Big],\\ &= \frac{1}{2\Delta x^2}\mathsf{Diff}_1,\end{aligned}$$

where

$$\mathsf{Diff}_1 = \Big[(D_{i-1,j}+D_{i,j})N_{i-1,j}-(D_{i-1,j}+2D_{i,j}+D_{i+1,j})N_{i,j}+(D_{i,j}+D_{i+1,j})N_{i+1,j}\Big].$$

Similarly,

$$\begin{aligned}\frac{1}{2}(\partial_y(D_{i,j}\partial_y^- N_{i,j}^n)+\partial_y^-(D_{i,j}\partial_y N_{i,j}^n)) &= \frac{1}{2\Delta y^2}\Big[(D_{i,j-1}+D_{i,j})N_{i,j-1}-(D_{i,j-1}+2D_{i,j}+D_{i,j+1})N_{i,j}\\ &\quad + (D_{i,j}+D_{i,j+1})N_{i,j+1}\Big],\\ &= \frac{1}{2\Delta y^2}\mathsf{Diff}_2,\end{aligned}$$

and

$$\mathsf{Diff}_2 = \frac{1}{2\Delta y^2}\Big[(D_{i,j-1}+D_{i,j})N_{i,j-1}-(D_{i,j-1}+2D_{i,j}+D_{i,j+1})N_{i,j}+(D_{i,j}+D_{i,j+1})N_{i,j+1}\Big].$$

So, to calculate the number of tumour cells in the next time step, we need to calculate

$$N_{i,j}^{n+1} = N_{i,j}^n + \frac{\Delta t}{2\Delta x^2}\mathsf{Diff}_1 + \frac{\Delta t}{2\Delta y^2}\mathsf{Diff}_2 + \Delta t k_{i,j}N_{i,j}^n\left(1-\frac{N_{i,j}^n}{\theta}\right). \tag{4.3}$$

For the Neumann boundary condition, it is important to know which pixels belong to the boundary. Here, we make a distinction between the boundary in the x-direction and y-direction for the breast. The two boundaries can be found in Figure 4.1. Note that the orientation is switched. Naturally, the points on the boundary of the matrix are also taken as boundary points. Since we have chosen an explicit time integration step, a bound for Δt has to be established to ensure the method remains stable.

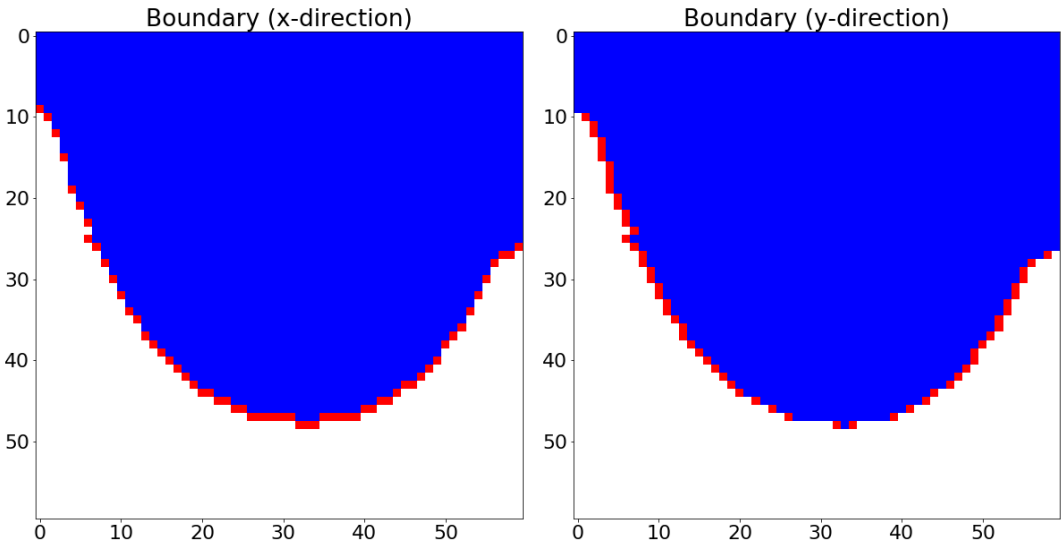

Figure 4.1: Boundaries of the breast for the x- and y-direction.

4.1.1. Stability Time Step

Since we will be using the fully explicit time integration method Forward Euler, the time step Δt has to be chosen such that the system is stable. Note that our equation is made up of a reactive and the diffusive part, so Δt has to be chosen such that both parts will be stable. Since the reactive part in nonlinear, we first linearize the equation $f(N) = kN\left(1 - \frac{N}{\theta}\right)$ around the numerical solution N^0:

$$\begin{aligned}
f(N) &\approx f(N^0) + f'(N^0)(N - N^0), \\
&= kN^0\left(1 - \frac{N^0}{\theta}\right) + \left(k\left(1 - \frac{N^0}{\theta}\right) + kN^0\frac{-1}{\theta}\right)(N - N^0), \\
&= kN^0\left(1 - \frac{N^0}{\theta}\right) + \left(k - \frac{2kN^0}{\theta}\right)(N - N^0), \\
&= kN^0 - \frac{kN^0}{\theta} + \left(k - \frac{2kN^0}{\theta}\right)N - kN^0 + 2k\frac{(N^0)^2}{\theta}, \\
&= k\frac{(N^0)^2}{\theta} + \left(k\left(1 - 2\frac{N^0}{\theta}\right)\right)N, \\
&= \mu + \lambda N.
\end{aligned}$$

Where μ is constant. In this case, we note that the stability of a system $y' = \lambda y$ is the same as $y' = \mu + \lambda y$ when μ is constant. Now, we can write the discretization for Equation (4.1):

$$\begin{aligned}
\frac{N_{i,j}^{n+1} - N_{i,j}^n}{\Delta t} &= \frac{1}{2\Delta x^2}\left[(D_{i-1,j} + D_{i,j})N_{i-1,j}^n - (D_{i-1,j} + 2D_{i,j} + D_{i+1,j})N_{i,j}^n + (D_{i,j} + D_{i+1,j})N_{i+1,j}^n\right] \\
&+ \frac{1}{2\Delta y^2}\left[(D_{i,j-1} + D_{i,j})N_{i,j-1}^n - (D_{i,j-1} + 2D_{i,j} + D_{i,j+1})N_{i,j}^n + (D_{i,j} + D_{i,j+1})N_{i,j+1}^n\right] \\
&+ k\left(1 - 2\frac{N^0}{\theta}\right)N_{i,j}^n
\end{aligned}$$

We can write the matrix produced by the discretization:

$$A = I + \frac{\Delta t}{2\Delta x^2}\begin{pmatrix} X_1 & \hat{X}_1 & & & \\ \hat{X}_1 & X_2 & \hat{X}_2 & & \\ & \ddots & \ddots & \ddots & \\ & & \hat{X}_{n_x-2} & X_{n_x-1} & \hat{X}_{n_x-1} \\ & & & \hat{X}_{n_x-1} & X_{n_x} \end{pmatrix} + \frac{\Delta t}{2\Delta y^2}\begin{pmatrix} Y_1 & & & & \\ & Y_2 & & & \\ & & \ddots & & \\ & & & Y_{n_x-1} & \\ & & & & Y_{n_x} \end{pmatrix}.$$
$$+ \Delta t \begin{pmatrix} k_{i,1}\left(1-2\frac{N^0}{\theta}\right) & & & & \\ & k_{i,2}\left(1-2\frac{N^0}{\theta}\right) & & & \\ & & \ddots & & \\ & & & k_{i,n_x-1}\left(1-2\frac{N^0}{\theta}\right) & \\ & & & & k_{i,n_x}\left(1-2\frac{N^0}{\theta}\right) \end{pmatrix}.$$

Where we have $N^{n+1} = AN^n$ and:

$$X_i = \begin{pmatrix} -(D_{i-1,1} + 2D_{i,1} + D_{i+1,1}) & & \\ & \ddots & \\ & & -(D_{i-1,n_y} + 2D_{i,n_y} + D_{i+1,n_y}) \end{pmatrix},$$
$$\hat{X}_i = \begin{pmatrix} D_{i-1,1} + D_{i,1} & & \\ & \ddots & \\ & & D_{i-1,n_y} + D_{i,n_y} \end{pmatrix},$$
$$Y_i = \begin{pmatrix} -(D_{i,0} + 2D_{i,1} + D_{i+1,2}) & D_{i,2} + D_{i,1} & & & \\ D_{i,2} + D_{i,1} & -(D_{i,1} + 2D_{i,2} + D_{i,3}) & D_{i,3} + D_{i,2} & & \\ & \ddots & \ddots & \ddots & \\ & & & D_{i,n_y+1} + D_{i,n_y} & -(D_{i,n_y-1} + 2D_{i,n_y} + D_{i+1,n_y+1}) \end{pmatrix}.$$

For stability, we need to have that the spectral radius of the matrix A is less than 1, $\rho(A) \leq 1$ [25, 41]. Note that A is symmetric, so all eigenvalues are real. Now, we can use Gershgorin's theorem. We see that the centers are

$$1 - \underbrace{\frac{\Delta t}{2\Delta x^2}}_{\mu_x}\underbrace{(D_{i-1,j} + 2D_{i,j} + D_{i+1,j})}_{D_x} - \underbrace{\frac{\Delta t}{2\Delta y^2}}_{\mu_y}\underbrace{(D_{i,j-1} + 2D_{i,j} + D_{i,j_1})}_{D_y} + \Delta t k_{i,j}\left(1 - 2\frac{N^0_{i,j}}{\theta}\right) =$$
$$1 - \mu_x D_x - \mu_y D_y + \Delta t k_{i,j}\left(1 - 2\frac{N^0_{i,j}}{\theta}\right).$$

With radii given by the sum of the off-diagonal terms:

$$\mu_x(D_{i-1,j} + D_{i,j}) + \mu_x(D_{i,j} + D_{i+1,j}) + \mu_y(D_{i,j-1} + D_{i,j}) + \mu_y(D_{i,j} + D_{i,j+1}) = \mu_x D_x + \mu_y D_y.$$

Now, by Gershgorin, we know that the eigenvalues λ_i for $i = 1, \ldots, n$ are bounded by:

$$\left|\lambda - \left(1 - \mu_x D_x - \mu_y D_y + \Delta t k_{i,j}\left(1 - 2\frac{N^0_{i,j}}{\theta}\right)\right)\right| \leq \mu_x D_x + \mu_y D_y, \tag{4.4}$$

$$\begin{cases} \lambda - \left(1 - \mu_x D_x - \mu_y D_y + \Delta t k_{i,j}\left(1 - 2\frac{N^0_{i,j}}{\theta}\right)\right) \leq \mu_x D_x + \mu_y D_y, \\ -\lambda + \left(1 - \mu_x D_x - \mu_y D_y + \Delta t k_{i,j}\left(1 - 2\frac{N^0_{i,j}}{\theta}\right)\right) \leq \mu_x D_x + \mu_y D_y, \end{cases} \tag{4.5}$$

$$\begin{cases} \lambda \leq 1 + \Delta t k_{i,j}\left(1 - 2\frac{N^0_{i,j}}{\theta}\right), \\ 1 - 2\mu_x D_x - 2\mu_y D_y + \Delta t k_{i,j}\left(1 - 2\frac{N^0_{i,j}}{\theta}\right) \leq \lambda. \end{cases} \tag{4.6}$$

So, for stability we need to have $k_{i,j}\left(1 - 2\frac{N^0_{i,j}}{\theta}\right) < 0, \forall i, j$. This means, that

$$\begin{cases} k < 0 \quad \text{if } (1 - 2\frac{N^0}{\theta}) > 0 \;\Rightarrow\; 0 < N^0 < \frac{1}{2}\theta, \\ k > 0 \quad \text{if } (1 - 2\frac{N^0}{\theta}) < 0 \;\Rightarrow\; \frac{1}{2}\theta < N^0 < \theta. \end{cases}$$

This means we can bound $k\left(1 - 2\frac{N^0}{\theta}\right) \geq -|k|_{max}$. Using this, from the first equation of Equation (4.6) we obtain the bound $\Delta t \geq 0$ for stability. For the second equation, we observe the following:

$$1 - 2\mu_x D_x - 2\mu_y D_y + \Delta t k_{i,j}\left(1 - 2\frac{N^0_{i,j}}{\theta}\right) \geq 1 - 2(\mu_x + \mu_y) \cdot 4D_{max} - \Delta t |k|_{max}. \tag{4.7}$$

Where we use that $D_x = D_{i-1,j} + 2D_{i,j} + D_{i+1,j} \leq 4D_{max}$ and similarly $D_y \leq 4D_{max}$, with D_{max} the largest diffusion coefficient. This needs to be greater or equal to -1 to satisfy the condition $-1 \leq \lambda \leq 1$. Therefore, we need

$$\left(\frac{\Delta t}{\Delta x^2} + \frac{\Delta t}{\Delta y^2}\right) 8D_{max} + \Delta t |k|_{max} \leq 2. \tag{4.8}$$

And thus the bound for the time step becomes:

$$0 \leq \Delta t \leq \frac{2}{|k|_{max} + 8D_{max}\left(\frac{1}{\Delta x^2} + \frac{1}{\Delta y^2}\right)}. \tag{4.9}$$

4.2. Linear Elasticity

The next equations in the model couple the surrounding tissue to the effects of the tumour growth. This will be done by incorporating Equations (2.3) and (2.4) into the model. Equation (2.4) calculates the displacement $\vec{u}$ in the x- and y- direction in each pixel. Using this, the von Mises stress can be calculated which influences the diffusion of tumour cells via Equation (2.3).

Equation (2.4) resembles the linear elasticity in isotropic material where G is the shear modulus representing the stiffness of the surrounding tissue. The breast is segmented into three types of tissue: fibroglandular, adipose and tumour tissue. In order to discretize the equation of linear elasticity, we make use of the Cauchy-Navier equations of linear elasticity [4]. The displacement vector shall be denoted by $\vec{u} = \begin{pmatrix} u \\ v \end{pmatrix}$.

$$\begin{cases} \frac{\partial}{\partial x}\left(\rho(x,y)\frac{\partial u}{\partial x}\right) + \frac{\partial}{\partial y}\left(\mu(x,y)\frac{\partial u}{\partial y}\right) + \frac{\partial}{\partial x}\left(\lambda(x,y)\frac{\partial v}{\partial y}\right) + \frac{\partial}{\partial y}\left(\mu(x,y)\frac{\partial v}{\partial x}\right) & = \lambda_f \frac{\partial}{\partial x} N(x,y,t), \\ \frac{\partial}{\partial y}\left(\rho(x,y)\frac{\partial v}{\partial y}\right) + \frac{\partial}{\partial x}\left(\mu(x,y)\frac{\partial u}{\partial y}\right) + \frac{\partial}{\partial y}\left(\lambda(x,y)\frac{\partial u}{\partial x}\right) + \frac{\partial}{\partial x}\left(\mu(x,y)\frac{\partial v}{\partial x}\right) & = \lambda_f \frac{\partial}{\partial y} N(x,y,t). \end{cases} \tag{4.10}$$

Where, $\rho(x,y) = 2\mu(x,y) + \lambda(x,y)$ and $\lambda_f = 2.5 \cdot 10^{-3}$ as seen in Table 2.2. In our case, $\mu = G$ and $\lambda = \frac{2\nu}{1-2\nu}G$. This means that λ and μ are both spatial parameters as $G = \frac{E}{2(1+\nu)}$. The Young's modulus, E, takes values of 2, 4 and 20 kPa depending whether the voxel is in fibroglandular, adipose or tumour tissue respectively [19, 20]. For the discretization, we again use a finite difference scheme. The same conservative scheme is used since the conservation means that we have a reflexive coefficient property which produces a symmetric matrix [25]. We rewrite Equation 4.10 for each term. We write $\rho_{i,j} = \rho(x_i, y_j)$ and we use that

$$\partial_x u_{i,j} = \frac{u_{i+1,j} - u_{i,j}}{\Delta x}, \qquad \bar{\partial}_x u_{i,j} = \frac{u_{i,j} - u_{i-1,j}}{\Delta x}.$$

Now, we can rewrite

$$\frac{\partial}{\partial x}\left(\rho_{i,j}\left(\frac{\partial u_{i,j}}{\partial x}\right)\right) = \frac{1}{2}\left[\partial_x(\rho_{i,j}\bar{\partial}_x u_{i,j}) + \bar{\partial}_x(\rho_{i,j}\partial_x u_{i,j})\right] \tag{4.11}$$

$$= \frac{1}{2}\left[\partial_x\left(\rho_{i,j}\frac{u_{i,j} - u_{i-1,j}}{\Delta x}\right) + \bar{\partial}_x\left(\rho_{i,j}\frac{u_{i+1,j} - u_{i,j}}{\Delta x}\right)\right] \tag{4.12}$$

$$= \frac{1}{2\Delta x^2}\left[\rho_{i+1,j}(u_{i+1,j} - u_{i,j}) - \rho_{i,j}(u_{i,j} - u_{i-1,j}) + \rho_{i,j}(u_{i+1,j} - u_{i,j}) - \rho_{i-1,j}(u_{i,j} - u_{i-1,j})\right] \tag{4.13}$$

$$= \frac{1}{2\Delta x^2}\left[(\rho_{i-1,j} + \rho_{i,j})u_{i-1,j} - (\rho_{i-1,j} + 2\rho_{i,j} + \rho_{i+1,j})u_{i,j} + (\rho_{i+1,j} + \rho_{i,j})u_{i+1,j}\right] \tag{4.14}$$

Similarly, for all other terms in the x-direction, we obtain:

$$\frac{\partial}{\partial y}\left(\mu_{i,j}\frac{\partial u_{i,j}}{\partial y}\right) = \frac{1}{2\Delta y^2}\left[(\mu_{i,j-1} + \mu_{i,j})u_{i,j-1} - (\mu_{i,j-1} + 2\mu_{i,j} + \mu_{i,j+1})u_{i,j} + (\mu_{i,j+1} + \mu_{i,j})u_{i,j+1}\right] \tag{4.15}$$

$$\frac{\partial}{\partial x}\left(\lambda_{i,j}\frac{\partial v_{i,j}}{\partial y}\right) = \frac{1}{2\Delta x\Delta y}\Big[\lambda_{i+1,j}(v_{i+1,j} - v_{i+1,j-1}) - \lambda_{i,j}(v_{i,j} - v_{i,j-1}) \tag{4.16}$$

$$+ \lambda_{i,j}(v_{i,j+1} - v_{i,j}) - \lambda_{i-1,j}(v_{i-1,j+1} - v_{i-1,j})\Big] \tag{4.17}$$

$$\frac{\partial}{\partial y}\left(\mu_{i,j}\frac{\partial v_{i,j}}{\partial x}\right) = \frac{1}{2\Delta x\Delta y}\Big[\mu_{i,j+1}(v_{i,j+1} - v_{i-1,j+1}) - \mu_{i,j}(v_{i,j} - v_{i-1,j}) \tag{4.18}$$

$$+ \mu_{i,j}(v_{i+1,j} - v_{i,j}) - \mu_{i,j-1}(v_{i+1,j-1} - v_{i,j-1})\Big] \tag{4.19}$$

And for the y-direction we obtain:

$$\frac{\partial}{\partial y}\left(\rho_{i,j}\frac{\partial v_{i,j}}{\partial y}\right) = \frac{1}{2\Delta y^2}\Big[(\rho_{i,j-1}+\rho_{i,j})v_{i,j-1} - (\rho_{i,j-1}+2\rho_{i,j}+\rho_{i,j+1})v_{i,j} + (\rho_{i,j+1}+\rho_{i,j})v_{i,j+1}\Big] \tag{4.20}$$

$$\frac{\partial}{\partial x}\left(\mu_{i,j}\left(\frac{\partial v_{i,j}}{\partial x}\right)\right) = \frac{1}{2\Delta x^2}\Big[(\mu_{i-1,j}+\mu_{i,j})v_{i-1,j} - (\mu_{i-1,j}+2\mu_{i,j}+\mu_{i+1,j})v_{i,j} + (\mu_{i+1,j}+\mu_{i,j})v_{i+1,j}\Big] \tag{4.21}$$

$$\frac{\partial}{\partial x}\left(\mu_{i,j}\frac{\partial u_{i,j}}{\partial y}\right) = \frac{1}{2\Delta x\Delta y}\Big[\mu_{i+1,j}(u_{i+1,j}-u_{i+1,j-1}) - \mu_{i,j}(u_{i,j}-u_{i,j-1}) \tag{4.22}$$

$$+\mu_{i,j}(u_{i,j+1}-u_{i,j}) - \mu_{i-1,j}(u_{i-1,j+1}-u_{i-1,j})\Big] \tag{4.23}$$

$$\frac{\partial}{\partial y}\left(\lambda_{i,j}\frac{\partial u_{i,j}}{\partial x}\right) = \frac{1}{2\Delta x\Delta y}\Big[\lambda_{i,j+1}(u_{i,j+1}-u_{i-1,j+1}) - \lambda_{i,j}(u_{i,j}-u_{i-1,j}) \tag{4.24}$$

$$+\lambda_{i,j}(u_{i+1,j}-u_{i,j}) - \lambda_{i,j-1}(u_{i+1,j-1}-u_{i,j-1})\Big] \tag{4.25}$$

Having obtained these equations, we can rewrite Equation 2.4 into a matrix vector multiplication:

$$M\vec{u} = \lambda_f \nabla N$$

Where $\vec{u} = \begin{pmatrix} u \\ v \end{pmatrix}$. The previous equations are to design the matrix M, which has a size of $2n \times 2n$ where n is the number of pixels in one 2-dimensional slice of the MRI scan. Dirichlet boundary conditions are imposed on the boundary of the breast so that the tissue displacements are zero on the boundary [19, 20, 44, 45].

To solve this system of equations, it is important to note that as the size of the matrix increases, the computation time will also increase drastically. With the full domain of the DCE-MRI scans being 512 x 512, this means the matrix M would be around 500,000 by 500,000. Each pixel on the boundary would produce a zero row in the matrix. However, to produce a matrix of full rank, a one is put on the main diagonal and the right hand side is taken as zero. This ensures that the matrix is invertible. Additionally, we note that the matrix is symmetric and all its eigenvalues are real and positive. This means that the matrix is symmetric and positive definite, SPD. For each time step, $\vec{u}$ needs to be solved. However, the matrix M only needs to be constructed once and does not change over time. Several approaches exist to solve the system of equations, direct solver, basic iterative methods or Krylov subspace methods [41]. The drawback of a direct solver such as Gaussian elimination is that they often take up too much time as the problem size gets larger. However, since the current implementation in two-dimensions is still reasonably small, a direct solver has been used to find $\vec{u}$. Note that for the three-dimensional model a Krylov subspace method such as Conjugate Gradient can be used to increase computational efficiency.

4.2.1. Von Mises Stress

In mechanics, von Mises stress combines the three principal stresses which can be compared to the yield stress to judge whether the material will yield or fracture. To calculate the von Mises stress, the displacements obtained by solving Equation 2.4 are used. Since we are working in 2-dimensions, the plane-strain equations are used as we cannot assume that the z-axis is infinitesimal. Note that

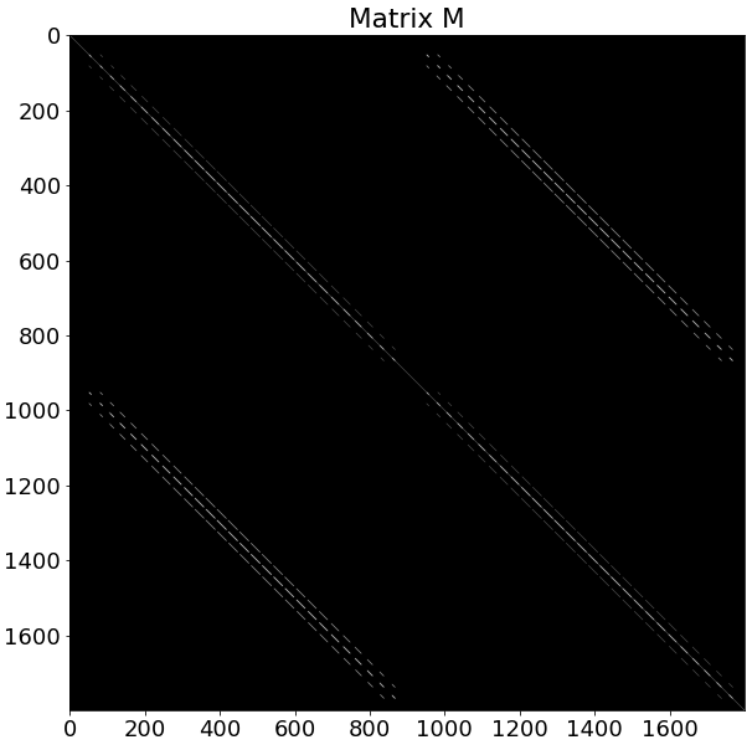

Figure 4.2: Constructed discretization matrix for Equation (2.4) for the domain which has been downsampled by factor 3. The resulting matrix is symmetric and positive definite with size $2n$ by $2n$ with n the number of voxels in the domain.

this means that $\sigma_{zz} \neq 0$ [21]. By using Hooke's 2D law for the stress-strain relationship:

$$\begin{aligned}
\sigma_{xx} &= \frac{E}{(1+\nu)(1-2\nu)}[(1-\nu)\varepsilon_{xx} + \nu\varepsilon_{yy}] \\
\sigma_{yy} &= \frac{E}{(1+\nu)(1-2\nu)}[\nu\varepsilon_{xx} + (1-\nu)\varepsilon_{yy}] \\
\sigma_{xy} &= \frac{E}{(1+\nu)}\varepsilon_{xy} \\
\sigma_{zz} &= \nu(\sigma_{xx} + \sigma_{yy}) \\
\sigma_{xz} &= 0 \\
\sigma_{yz} &= 0
\end{aligned}$$

And in turn we can relate the strain to the obtained displacements.

$$\begin{aligned}
\varepsilon_{xx} &= \frac{\partial u}{\partial x} \\
\varepsilon_{yy} &= \frac{\partial v}{\partial y} \\
\varepsilon_{xy} &= \frac{1}{2}\left(\frac{\partial u}{\partial y} + \frac{\partial v}{\partial x}\right)
\end{aligned}$$

Lastly, we can calculate the von Mises stress in each voxel using

$$\sigma_{vm}(x,y) = \sqrt{\sigma_{xx}^2 + \sigma_{yy}^2 + \sigma_{zz}^2 - \sigma_{xx}\sigma_{yy} - \sigma_{xx}\sigma_{zz} + \sigma_{yy}\sigma_{zz} + 3\sigma_{xy}^2} \tag{4.26}$$

Using the obtained von Mises stress, the diffusion coefficient, D, is updated. There is an inverse relationship between the von Mises stress and diffusion, as the stress increases, the diffusion will

decrease. This means that areas where the tumour wants to grow with higher stiffness will result in more stress, which in turn results in the diffusion becoming smaller. This means that the tumour can less easily spread through fibroglandular tissue than adipose tissue.

4.3. Parameter Calibration

The goal of this thesis is to be able to accurately predict the response for each individual patient. Therefore, the patient-specific parameters will need to be calibrated. There are two different parameters which will be calibrated, the global diffusion of tumour cells when there is no stress D_0 and the spatial parameter which denotes the proliferation rate in each voxel $k(x, y)$. To calibrate these parameters, the non-linear least squares optimization algorithm Levenberg-Marquardt will be used. This algorithm is widely used for data fitting applications [15, 16, 19, 20, 28, 44, 45]. The algorithm combines two minimization algorithms: the gradient-descent method and the Gauss-Newton method. Levenberg-Marquardt acts more like a gradient-descent method whenever the parameters are far from the optimal value and more like Gauss-Newton when they are closer.

Levenberg-Marquardt tries to minimize the sum of the squares of the deviations, $S(\bar{\beta})$.

$$\text{argmin}_{\bar{\beta}} S(\bar{\beta}) = \text{argmin}_{\bar{\beta}} ||f(\bar{\beta}) - \bar{y}||_2^2$$

Where $\bar{\beta}$ are the to be determined parameters $(D_0, k_1, \ldots, k_n)$ with n number of voxels, and $\bar{y}$ are the observations. In this particular case, the MRI scan at time 1, t_1, and time 2, t_2 shall be used to calibrate the parameters. The model is initialized with the number of tumour cells from time 1, $N(x, y, t_1)$, then it is propagated forward in time to calculate the number of tumour cells at time 2, $N(x, y, t_2)$. The error between this estimate, $f(\bar{\beta})$ and the actual number of tumour cells from scan 2, the observations $\bar{y}$, is to be minimized. For n number of voxels within an MRI scan, we have n observations, $\bar{y} \in \mathbb{R}^n$. However, there are $n + 1$ parameters, $\bar{\beta} = D_0, k_1, \ldots, k_n \in \mathbb{R}^{n+1}$. This means that the current optimization problem is underdetermined. Thus, there are more unknowns than equations, which means there are either 0 or ∞ number of solutions. Since the equations describe reality and have been widely used in previous literature, we can assume that there is at least 1 solution, thus there are infinitely many solutions.

Therefore, a Tikhonov regularization term is added to the optimization to ensure the problem is no longer ill-posed. This means that the minimization now goes as follows:

$$\text{argmin}_{\bar{\beta}}(S(\bar{\beta}) + ||\Gamma\beta_0||_2^2) = \text{argmin}_{\bar{\beta}}(||f(\bar{\beta}) - \bar{y}||_2^2 + ||\Gamma\beta_0||_2^2). \tag{4.27}$$

The Tikhonov regularization term is denoted by Γ. From this, we can observe that whenever Γ is large, β_0 should be close to zero to minimize the error. When Γ is small, β_0 has more freedom. For our application, we have chosen to put the Tikhonov regularization only on the diffusion coefficient D_0 since this is the global parameter and literature suggests that its value should be close to zero [19, 46].

We do note the following observation. If all voxels which contain tumour cells at time 2, already contained tumour cells at time 1 and all voxels with tumour cells at t_1 have more than 0 but less than θ tumour cells, there is one unique solution for D_0. Namely, the diffusion D_0 is zero and the proliferation rate for each voxel can be chosen such that Equation 4.27 is zero. However, this is naturally not the case since the number of tumour cells at t_1 is θ for at least one voxel and because of registration the shape of the tumour might shift a bit over time. Conversely, some voxels might not have any tumour cells at t_1 but do have tumour cells at t_2.

To further illustrate the step-by-step procedure for the parameter calibration, two diagrams have been made. The diagram in Figure 4.3 shows the parameter calibration for the simple model, i.e. the implementation of only the reaction-diffusion equation. We initialize with the tumour cell number from MRI scan at t_1. Then, the tumour cells in the next time step are iteratively calculated until we

reach t_2. Next, it is determined whether the convergence criterion is met which tries to minimize the error between obtained tumour cells and the tumour cells from the MRI scan at t_2. If the convergence criterion is not met, the parameters are changed slightly and the model calculations are performed again until model parameters have been found which satisfy the convergence criterion.

The second diagram can be found in Figure 4.4. In this diagram, the parameter calibration is shown for the complete model. The concept is the same, though a few more steps are done. Again, we initialize with the number of tumour cells determined from MRI scan 1. Then, the spatial derivative of the tumour cells, $N(x, y, t)$ is calculated in each voxel. Using this, Equation 2.4 is solved for the displacement $\vec{u}$. The displacements are then used to determine the strain, stress and finally the von Mises stress in each voxel. Using the von Mises stress, the diffusion coefficients are updated. Finally, the number of tumour cells in the next time step can be found using Equation 2.2. This process is repeated for every time step until we reach t_2. The remainder of the procedure remains the same. The calculated number of tumour cells is compared to the actual observed number of cells. If the convergence criterion is not met, the parameters are changed and this is all repeated until convergence is met. Using these calibrated parameters $k(x, y)$ and D_0, the model can then be propagated forward in time to predict the number of tumour cells at a later stage. The third MRI scan can then be used to validate the model's predictive capability.

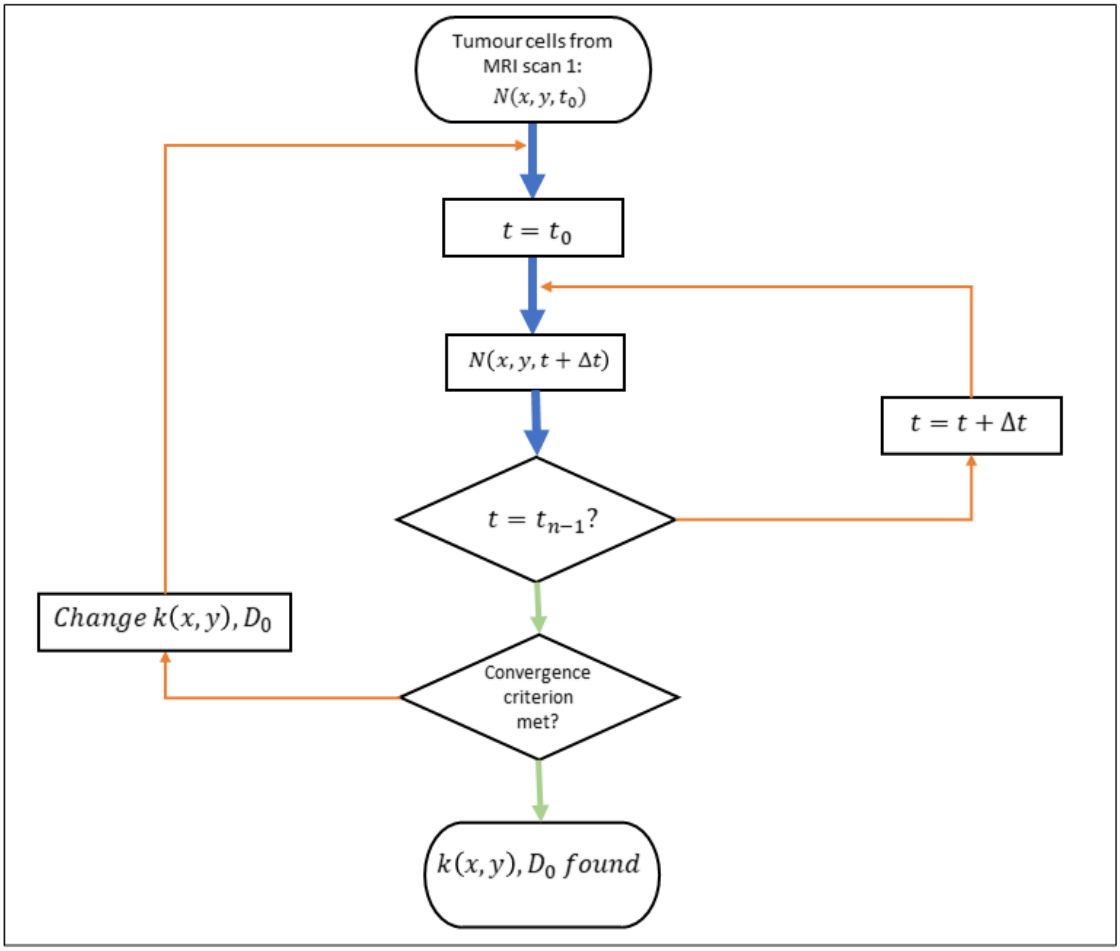

Figure 4.3: Diagram for the parameter calibration of the simple model. Initialization with the tumour cells from scan 1 and an initial guess for $k(x, y)$ and D_0. Then, the number of tumour cells is updated until we arrive at the time of MRI scan 2. Check whether the convergence criterion is met, if not, change the parameters. Repeat this until the convergence criterion is met, then the parameters have been optimized.

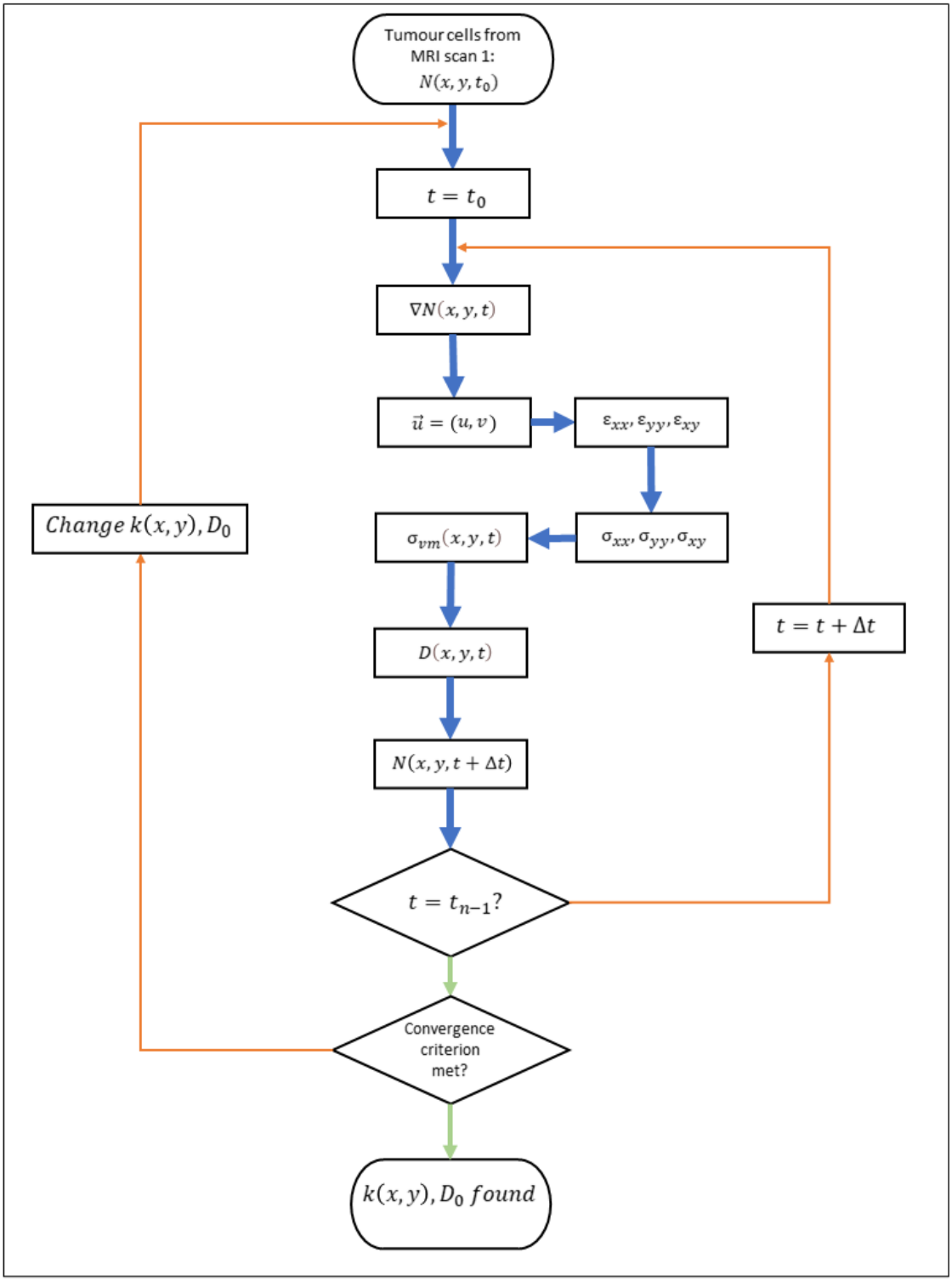

Figure 4.4: Diagram for the parameter calibration of the complete model. Initialization with the tumour cells from scan 1 and an initial guess for $k(x, y)$ and D_0. Then, the gradient of the number of tumour cells is calculated to solve equation (2.4). This provides $\vec{u}$ which is used to calculate the strain, stress and use them to update the von Mises stress. Using the von Mises stress, the diffusion is updated and the number of tumour cells can be calculated for the next time step. This is repeated until we arrive at the time of MRI scan 2. Check whether the convergence criterion is met, if not, change the parameters. Repeat this until the convergence criterion is met, then the parameters have been optimized.

5

Analysis

This chapter will focus to elaborate and illustrate the model's performance. First, the influence of the patient-specific parameters will be illustrated. Then, some initial experiments with the QIN-Breast data are done. Additionally, some in silico experiments are performed to study the model's predictive capabilities as well as the influence of the incorporation of the surrounding tissue.

5.1. Influence of Patient-Specific Parameters

The key components to this model, the patient-specific parameters, are the diffusion of tumour cells, D_0, and proliferation rate, $k(x, y)$. D_0 is a global parameter and determines how much the tumour cells 'spread', while $k(x, y)$ is a spatial parameter with a value in each pixel. Note that in the current model, $k(x, y)$ may take either positive or negative values depending on whether there is tumour cell growth or decay in this particular voxel. To illustrate the effects of different values of k and D_0, we will experiment with different values for both to see the outcome. The first experiment will be done for just the diffusive part of the equation, to validate that the model has been correctly implemented. Due to the Neumann boundary conditions, if the proliferation rate is 0, the number of tumour cells within the breast should reach a steady state equilibrium which is the average of all tumour cells. We will start with a very simple square domain. Within this domain, each pixel will be provided with a random number of tumour cells between 0 and 100. The four middle points in the domain will have the most tumour cells of 200. For this test, we take $D_0 = 0.5$ and calculate the tumour cell distribution over a span of 35 days. The results can be observed in Figure 5.1. We indeed see that the number of tumour cells in each pixel approaches the equilibrium. The next step is of course to carry out multiple experiments for the actual domain. For now, the data of the QIN-Breast study is used to perform the experiments.

The simple model, i.e. only the reaction-diffusion as seen in Equation 4.1, is implemented for different choices of $k(x, y)$ and D_0 to see what the influence is of both parameters. Here, even though the proliferation rate is a spatial parameter, $k(x, y)$ is chosen the same for each pixel. The results of the performed experiments can be found in Figure 5.2. In this figure, the initial tumour cell number can be seen (top left), followed by 8 experiments that show the modelled tumour cell number after 10 days with various choices for $k(x, y)$ and D_0. We see that both the proliferation rate and diffusion of tumour cells affect the spread of the tumour differently.

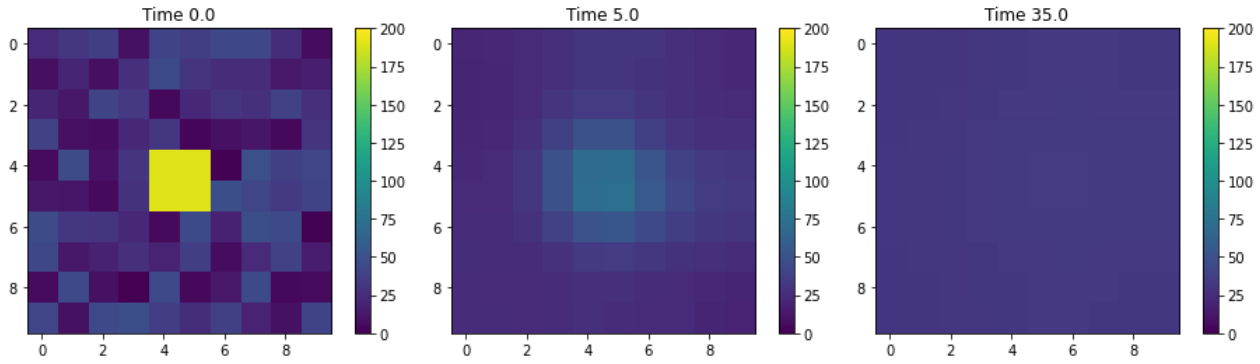

Figure 5.1: Tumour growth simulation using a diffusion equation with Neumann boundary conditions over a timespan of 35 days. Every pixel is initialized with a random number of tumour cells between 0 and 100. The four pixels in the centre have 200 tumour cells Since no proliferation is present, the solution should reach a steady state which is the average of the tumour cells. This is the case, as seen in the image on the right.

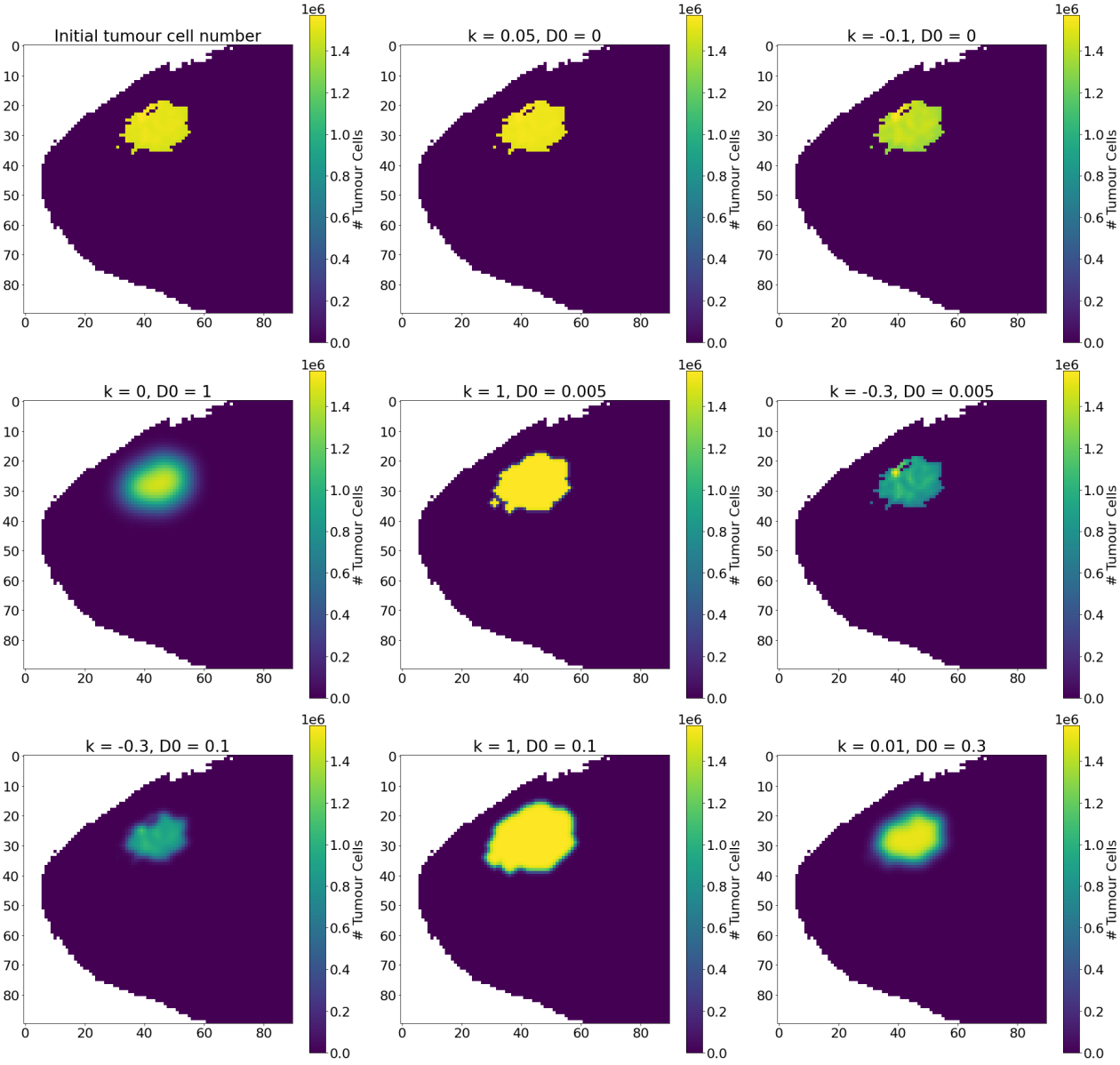

Figure 5.2: Simulations over 10 days of the reaction-diffusion equation using different values for $k(x, y)$ and D_0. The top left image shows the initial tumour cell number. All other images are the resulting tumour after 10 days with their respective choices of $k(x, y)$ and D_0. Note, $k(x, y)$ is chosen as a global value, the same for each pixel.

The diffusion determines how much the current tumour cells spread. The proliferation rate determines how fast the tumour cells within a pixel will grow/decay. We see that combining a high proliferation rate with high diffusion causes the tumour to spread most rapidly. If we only have the proliferation rate in each pixel, the tumour will not spread, i.e. surrounding pixels will not become tumour cells, but the number of tumour cells within each pixel will only grow/decay (bounded by zero and the carrying capacity). If there is only diffusion, the total number of tumour cells will not change but the surrounding cells will become tumour cells. Different combinations of both are possible and are shown in Figure 5.2 to illustrate the effects of both parameters.

5.2. Simple Parameter Calibration

In the previous section, we experimented with different values for $k(x, y)$ and D_0. In reality, these patient-specific parameters have to be determined from data. Two MRI scans are used, one prior to the patient receiving chemotherapy and one during the treatment. Using these two MRI scans, an estimation can be made for the diffusion and proliferation rate of the patient's tumour. These parameters will then be taken as their given value and finally, the model can be projected forward in time to see whether the model is capable of accurately predicting the tumour's size at the conclusion of therapy. To make an estimation of $k(x, y)$ and D_0, we will use a nonlinear least squares regression, Levenberg Marquardt as explained in the previous chapter [19, 20, 45].

This experiment is carried out using the data from the QIN-Breast study, Patient0059. Since this parameter calibration is carried out only using the simple model, i.e. Equation 2.2, no downsampling was necessary. Since for this patient, data from only two time points are available, this experiment is merely to see how well the model can calibrate using real data.

In Equation (2.2), changing the value of $k(x, y)$ in the pixels where no tumour cells are found, will have no influence on the model since $N(x, y)$ is zero. Therefore, to reduce computation time, we have decided to make a mask in which the values of $k(x, y)$ need to be determined as this drastically reduces the number of variables. In Figure 5.3, the number of tumour cells extracted from the MRI scans at time 0 and time 1, i.e. before and during chemotherapy, along with the made mask for $k(x, y)$ are shown. Now, we need to determine the variables $k(x, y)$ and D_0. To do this, we again refer to the diagram in Figure 4.3. We wish to obtain an estimate for $k(x, y)$ and D_0 which minimizes the error between the modelled tumour growth at time 1 and the obtained tumour from MRI scans at time 1. Then, these estimates can be used to further propagate the model in time and see how the tumour will grow.

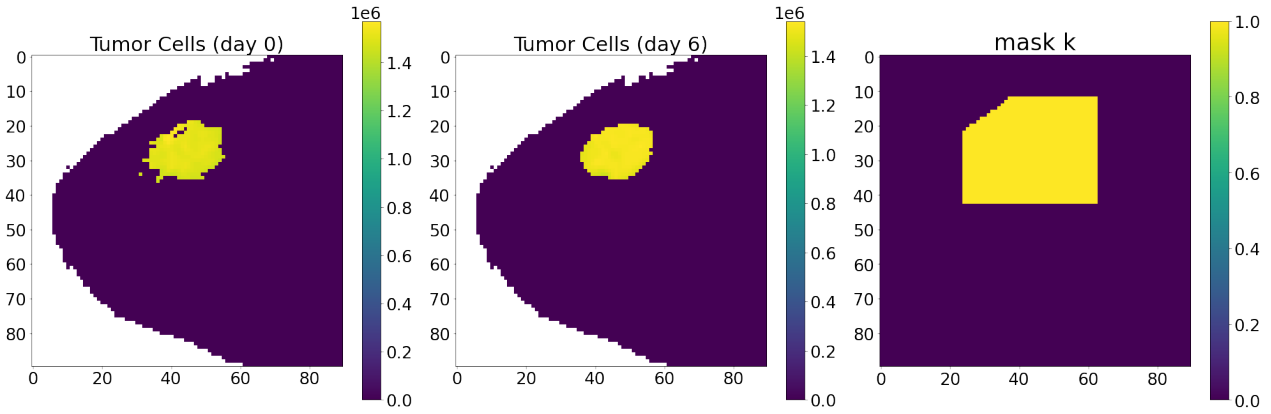

Figure 5.3: Tumour cells derived from the MRI scan 1 (day 0) and 2 (day 6), seen on the left and middle image. The right image shows the mask made for the parameter calibration for $k(x, y)$. All pixels within the yellow part will be used in calibration. Since $k(x, y)$ can only be determined in pixels where tumour cells are present, the mask is made to reduce computation time.

The convergence criterion which has been used is to stop whenever the changes in $k(x, y)$ and D_0 become smaller than 10^{-4} and we let the Levenberg-Marquardt algorithm calculate until this criterion is met. Estimating the proliferation rate and diffusion, took about 3.5 minutes. The resulting proliferation rate can be found in Figure 5.4. In this figure, we also see the model prediction with the obtained $k(x, y)$ and D_0 at time 1, which is after 6 days in this case. Additionally, the absolute error is shown between the actual number of tumour cells from MRI scans and the obtained tumour prediction. The estimate for the diffusion, D_0, is $1.47 \cdot 10^{-2}$ mm^2/day. The values obtained lie within the expected range obtained from literature values [19].

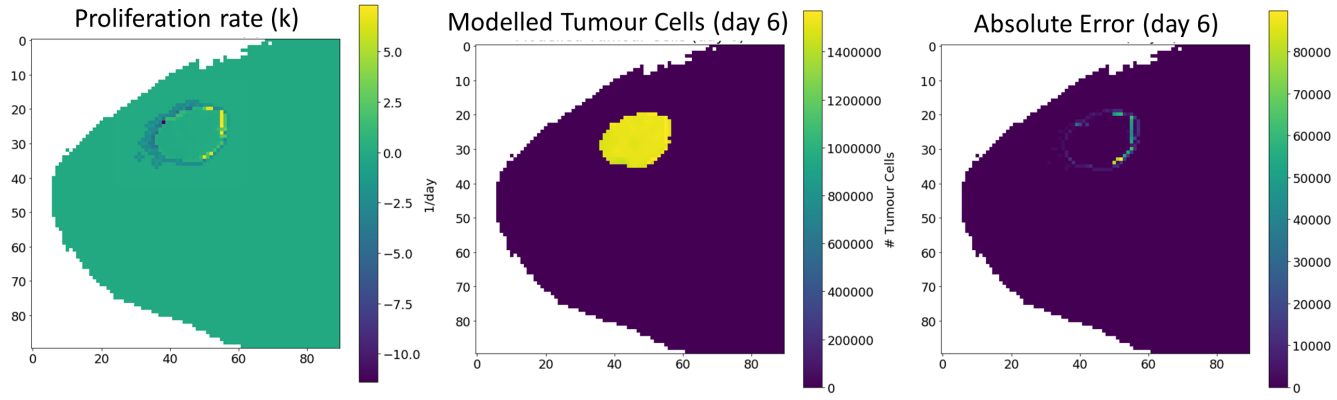

Figure 5.4: Results after parameter calibration. Left shows the obtained proliferation rate map. Middle image shows the modelled tumour cellls on day 6 using the calibrated parameters. Right image shows the absolute error made between the tumour cells from the MRI scan and the calculated number of tumour cells.

As we can see, the error is quite small with a maximum of about 80,000 on a scale of 1.6 million. To decrease the error, we could change the convergence criterion to a more strict one. The proliferation rate shows a decay on the left side of the tumour and an increase on the right hand side. This is likely due to the tumour not overlapping completely after registration and not necessarily because the tumour grew in this direction.

Lastly, we can also take a look at the model prediction further in time with the obtained proliferation rate and diffusion. The resulting image can be seen in Figure 5.5. It is interesting to see how the tumour would change after such time, though we are unable to validate these results as no further MRI scan is available. In the next chapter, we will take a much closer look at these predictions and validate them using the data from Erasmus MC.

5.3. In Silico Experiments

In this section, several in silico experiments shall be carried out to observe the model performance in a controlled setting. First, the parameter calibration shall be carried out for both the simple and complete model to see how well the correct values are found. Then, an experiment is done to observe the effects of incorporating the surrounding tissue on tumour cell growth.

5.3.1. Parameter Calibration

The first experiment will be a controlled experiment where the model is initialized with the tumour cells from time 1 from Patient001. Then, the model is propagated forward in time using chosen values of D_0 and $k(x, y)$ to produce a 'grown' tumour after 10 days using time steps of 0.25 days. Using this obtained tumour cell number, the parameter calibration is carried out to observe the performance of Levenberg-Marquardt in obtaining the parameters. Again, a mask for $k(x, y)$ was used to reduce the computation time. This experiment is performed for both the simple model, i.e. only Equation 2.2,

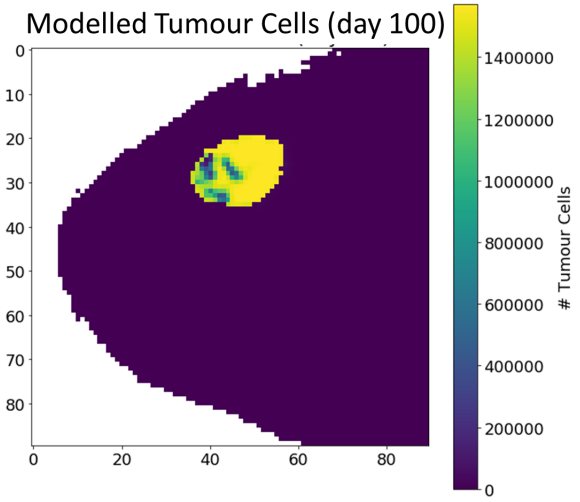

Figure 5.5: Estimation for number of tumour cells after 100 days using the calibrated parameters.

and the complete model, i.e. all three Equations 2.2, 2.3 and 2.4. The initial guess, true values along with the obtained estimation can be observed in Table 5.1. Additionally, the maximum absolute error is shown between the predicted tumour cell number using the obtained parameters and the tumour cell number found using the chosen parameters. The estimation shown for $k(x, y)$ is the average value within the tumour.

	Parameter	Initial Guess	True Value	Estimation	Max. absolute Error
Simple Model	D_0	1.00×10^{-3}	1.00×10^{-4}	6.022×10^{-5}	8.903×10^{-3}
	k	-0.08	-0.1	-0.1011	
Complete Model	D_0	1.00×10^{-3}	1.00×10^{-4}	6.022×10^{-5}	6.507×10^{-3}
	k	-0.08	-0.1	-0.1010	

Table 5.1: Results of in silico parameter estimation for both simple and complete model. Estimation for k refers to the average proliferation rate within the tumour since this is a spatial parameter. The maximum absolute error refers to the maximum error between the calculated tumour cell number at time 2 and obtained tumour cell number from the MRI scan at time 2.

Additionally, the proliferation rate maps can be observed in Figure 5.6. As can be seen, the difference in predictions for the simple and complete model is minimal. One of the things we observed was that using an initial guess quite close to the true value increased the accuracy of the estimation. Also, the calibration of the proliferation is very good within the tumour, but we can see in Figure 5.6 that on the border of the tumour the proliferation rate is predicted to be positive.

5.3.2. Effects of Surrounding Tissue

To illustrate the effects of the incorporation of the surrounding tissue in the breast into the model, the following experiment shall be carried out. A slice is taken from one of the breasts of Patient001, which contains no tumour. Then, a seed tumour is modelled inside the breast that is surrounded by the adipose, fatty, tissue. This seed tumour will be one pixel with value θ tumour cells. Then, the model is propagated forward in time. This experiment is done to observe how the stiffness of the

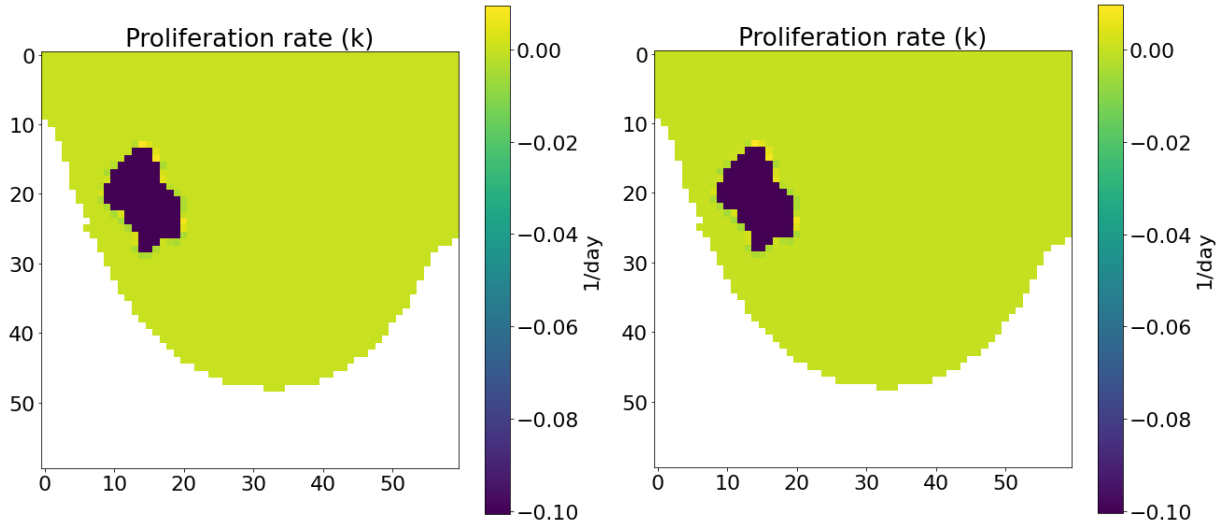

Figure 5.6: Spatial map of the proliferation rates obtained in the in silico experiment. Left image is after calibration using only the simple model, right image is for the complete model. Both are very similar.

surrounding tissue will inhibit the growth of the tumour compared to the simple model. The adipose tissue is the softest tissue where the Young's modulus, E, is 2 kPa. Since this is an experiment, the values of D_0 and $k(x, y)$ were chosen and not calculated. The chosen values are 0.5 [mm^2/day] and 1 [day^{-1}] respectively. Note that $k(x, y)$ is taken the same for every voxel. Using these choices, the tumour will actively grow and thus the effects can be seen more clearly. No downsampling is used in this experiment, only the zoomed in breast which has a matrix resolution of 180×180. Using the obtained carrying capacity from the dimensions of the slice, $\theta \approx 1.247 \cdot 10^5$, produces the results found in Figure 5.9.

In this figure, the location of the seed tumour and the stiffness of surrounding tissue can be observed in subfigure (b). In subfigure (c), the tumour cells after 20 days are shown for the simple model and in subfigure (d) for the complete model. In this current experiment, the difference in tumour cells is not noticeable between the two different model calculations. In figure 5.8, the spatial distribution of the tumour cells is shown along the biggest axes. It can be seen that the spatial distribution of the tumour cells using the simple model, i.e. no mechanics, is slightly larger than the complete model. This is in line with what we would expect since the incorporation of the surrounding tissue produces stress which in turn decreases the diffusion and thus the spread of the tumour. Whilst there is a very slight difference in number of tumour cells between the simple and complete model, this is much less pronounced than we initially expected from the literature [45]. In this paper, they use an initial value of $\theta \approx 5 \cdot 10^6$. Therefore, we will repeat the experiment where the seed tumour will be initialized with 5 million tumour cells. As we can see in Figure 5.9, the effects of the incorporation of surrounding tissue are much more pronounced. The cell distribution in the case of no mechanical coupling shows uniform radial decay, whereas the mechanically coupled version does not. In the mechanically coupled version, the complete model, it can also be observed that the areas where the tumour grows in fibroglandular tissue is more restricted than areas where the tumour continues to grow in adipose tissue. The spatial distributions of the tumour cells for this experiment can be found in Figure 5.10. Here, it can be seen how the incorporation of the surrounding tissue has a drastic effect on the spatial distribution of the tumour cells.

The areas where the tumour growth is most inhibited, the fibroglandular tissue, are the areas where the highest amount of stress is exhibited. Since the diffusion is inversely related to the amount of stress, this reduces the diffusion in these areas. This can be observed in Figure 5.11. This figure shows the Von Mises stress as well as the diffusion coefficients at 20 days. As can be seen, the

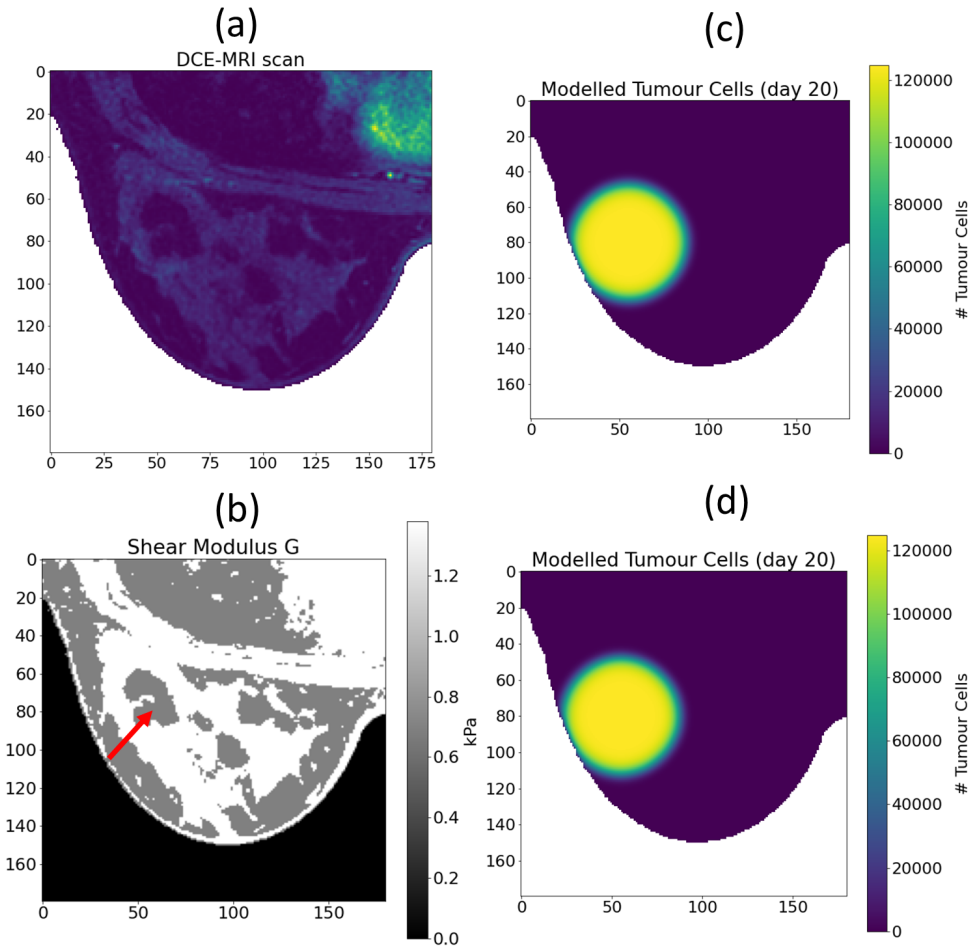

Figure 5.7: Results for tumour growth using seed tumour for simple and complete model. Figure (a) shows the original breast slice used without which has no tumour. Figure (b) shows the segmentation of the fibroglandular (white) and adipose tissue (grey) and the red arrow shows the location of the seed tumour, initialized with value $\theta \approx 1.247 \cdot 10^5$. Figures (c) & (d) show the calculated tumour cell number after 20 days for the simple and complete model, respectively. For both experiments, $D_0 = 0.5$ mm^2/day and $k(x, y) = 1$ day^{-1}.

areas with the higher tissue stiffness produce more stress and thus lower diffusion. This experiment was done using a positive proliferation rate. Note that using the same negative proliferation rate also means that the model with mechanics is slower to reduce in tumour cellularity than the simple model.

From this experiment, the following observation can be made. For the model, only one 2-dimensional slice is taken from within the breast. The dimensions of the voxels in this 2-dimensional slice are used to calculate the carrying capacity, θ. After this, the model predictions are only carried out in 2-dimensions. This means that although the size of the voxel in the third dimension is not used in the model calculations, it does have a significant role in determining the carrying capacity for the model. This, in turn, has effects on how much the surrounding tissue has influence on the growth of the tumour cell number, as illustrated here. This shall be further discussed in the next chapter.

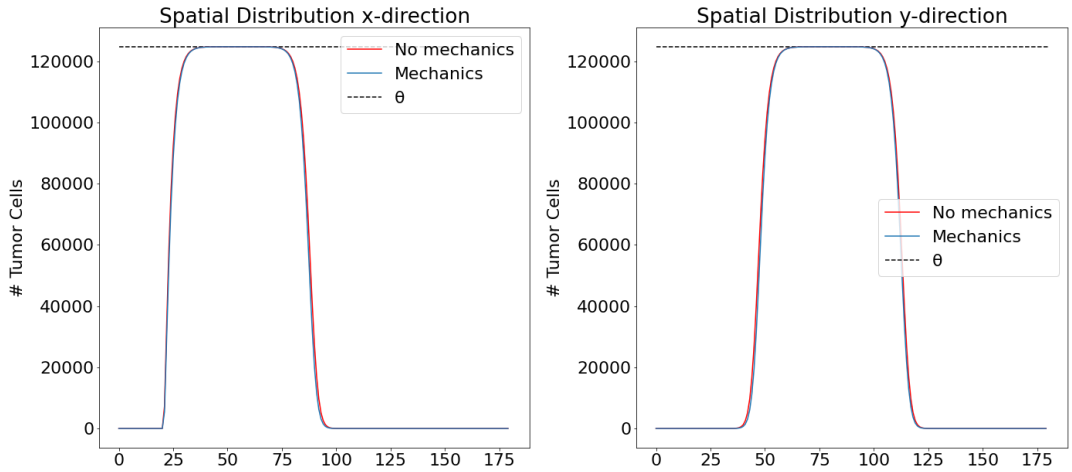

Figure 5.8: Spatial distribution of tumour cells taken through the centre of the tumour. Red shows the tumour distribution for the simple model after 20 days, blue for the complete model.

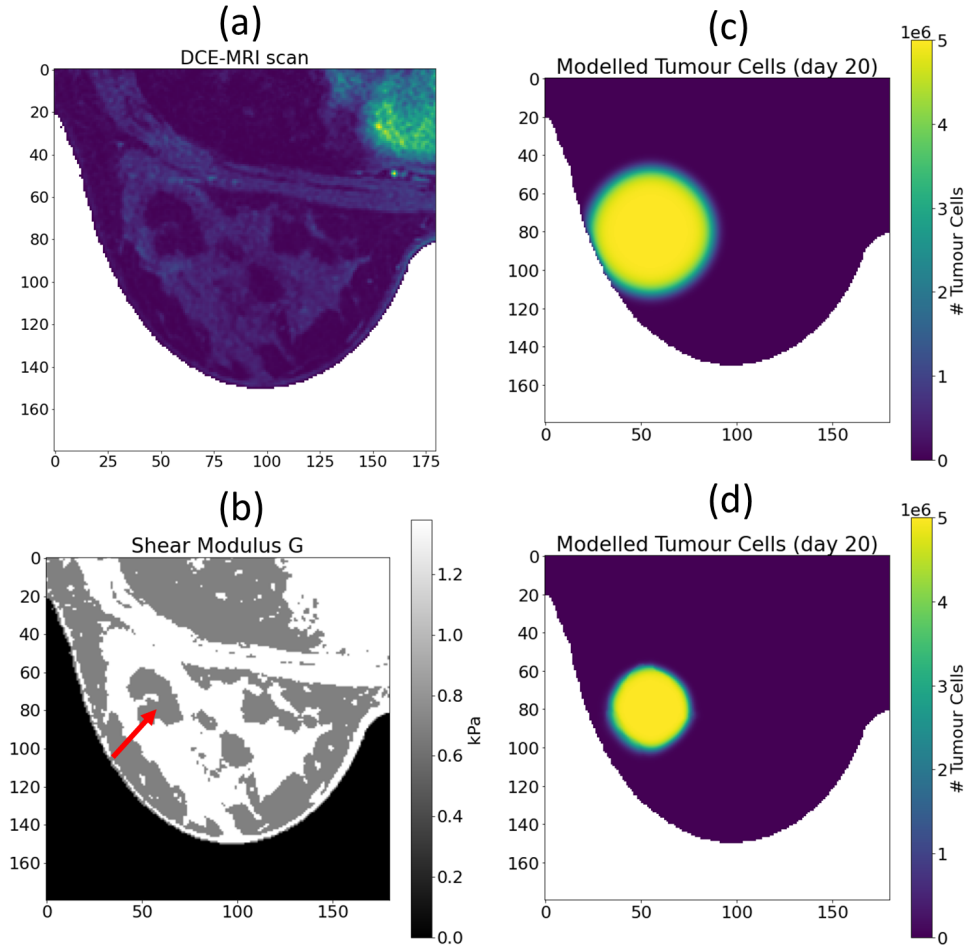

Figure 5.9: Results for tumour growth using seed tumour for simple and complete model. Figure (a) shows the original breast slice used without which has no tumour. Figure (b) shows the segmentation of the fibroglandular (white) and adipose tissue (grey) and the red arrow shows the location of the seed tumour, initialized with value $\theta \approx 5 \cdot 10^6$. Figures (c) & (d) show the calculated tumour cell number after 20 days for the simple and complete model, respectively. For both experiments, $D_0 = 0.5$ mm^2/day and $k(x, y) = 1$ day^{-1}.

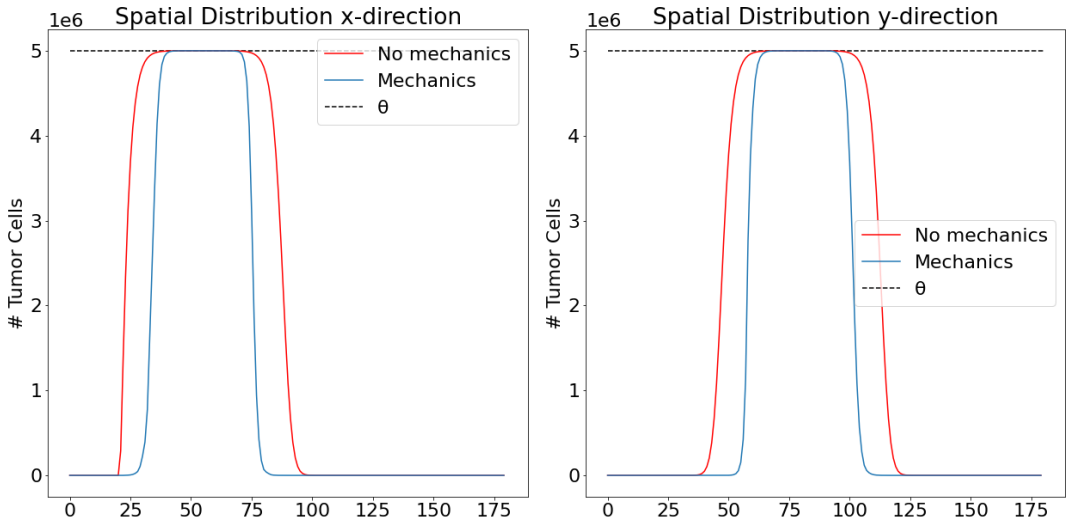

Figure 5.10: Spatial distribution of tumour cells taken through the centre of the tumour. Red shows the tumour distribution for the simple model after 20 days, blue for the complete model.

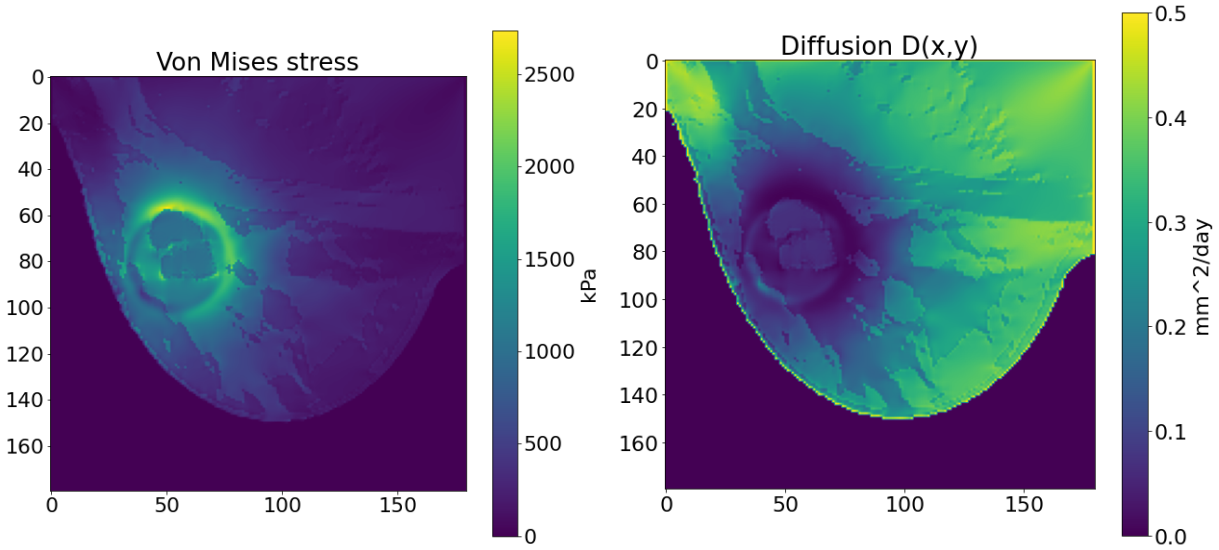

Figure 5.11: Left shows the von Mises stress after 20 days, right image shows the diffusion. In areas with higher tissue stiffness, the von Mises stress becomes larger, this has an inverse effect on the diffusion. This shows that the tumour cells can spread more easily through less stiff tissues.

6

Results

In the previous chapters, the model implementation has been discussed in detail and some preliminary results and in silico experiments of the model performance have been shown. As these experiments were done using the QIN-Breast study data, no model validation was possible. In this chapter, the performance of the model will be looked at in several different stages. The model using only the reaction-diffusion equation as well as the complete model implementation shall be tested for the different patients provided by Erasmus MC. In the end, the results will be compared to the third MRI scan to validate the model's predictive capabilities.

6.1. Model Predictions

For each patient, all scans were registered to a common image space using the preprocessing described in Chapter 3. To reduce computation time, the domain of interest is zoomed in to that of just the breast. This results in a resolution of 180 x 180 for Patient001 and Patient003 and 210 x 210 for Patient002. Then, they are downsampled by a factor three, as this still preserves the shape of the tissues and tumour while reducing the computation time drastically. Since the model implementation was done in 2-dimensions, a slice within the breast needed to be chosen at each time point. For the experiments, the central tumour slice was chosen for each different time point. Ideally, this would be the same slice for each time point since registration has been carried out. Unfortunately, this is not necessarily the case, especially for Patient002 who was challenging for the registration. Therefore, the central tumour slice for each individual time point is taken. In Figure 6.1, the tumour cell number is shown of the three MRI scans of Patient001. Additionally, the segmented tissues are shown, where the breast was segmented into adipose, fibroglandular and tumour tissue. Lastly, the breast region of interest is shown which was found using region growing. This is also done for the other patients, which can be found in the Appendix.

6.1.1. Patient001

What we wish to investigate is the predictive ability of the simple model, i.e. only using the reaction-diffusion equation. Additionally, we wish to compare this to the predictive ability of the complete model, i.e. with the incorporation of the surrounding tissues. To create a model prediction, the patient-specific parameters need to be calibrated, the spatial proliferation rate $k(x, y)$ and global diffusion of tumour cells D_0.

The Levenberg-Marquardt nonlinear least squares regression algorithm has been used to determine these parameters. Using this algorithm, the first two MRI scans time point are used for the optimization, as explained in previous chapters. Several factors can be chosen which will affect the resulting proliferation rate map and diffusion. These consist of the convergence criterion, the

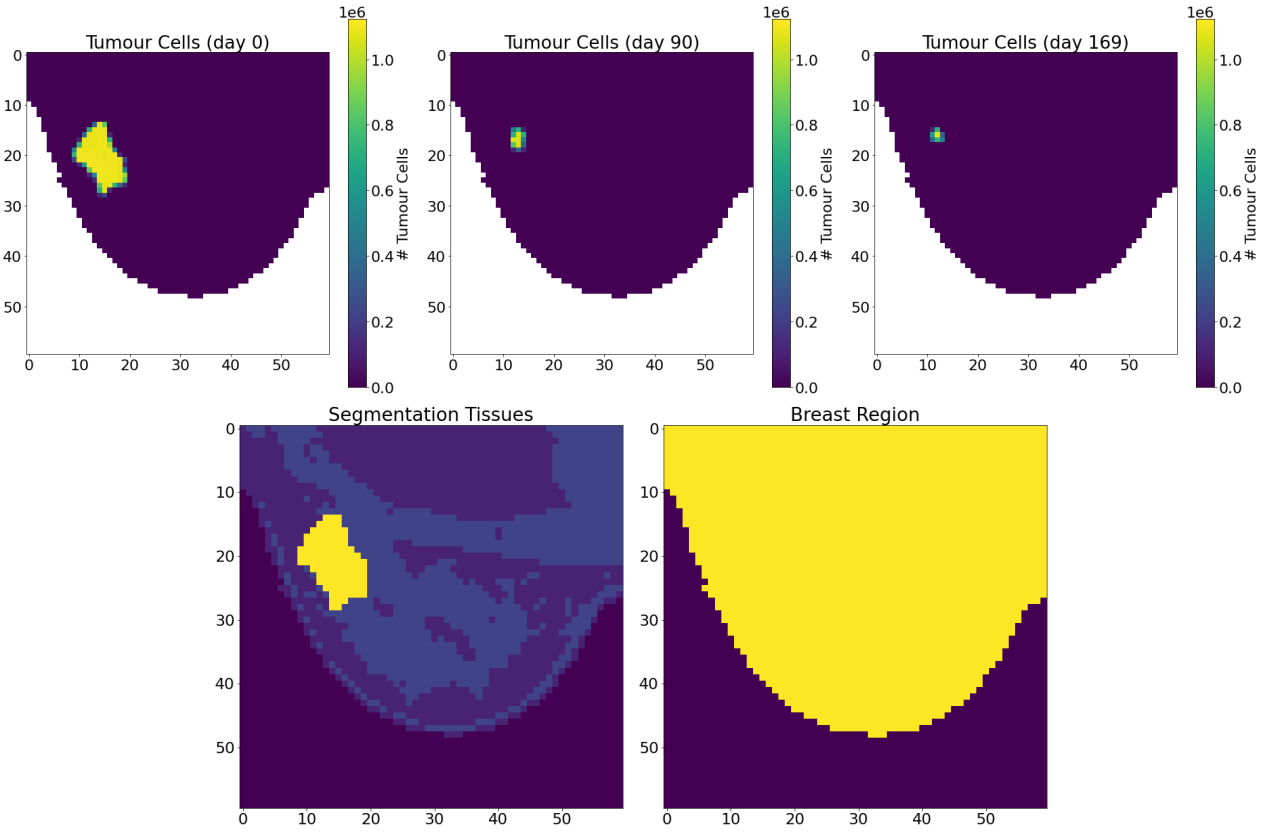

Figure 6.1: Tumour cells of Patient001 obtained from the DWI-MRI scans at the three time points. Bottom left shows the segmentations of the fibroglandular (light blue), adipose (blue) and tumour tissue (yellow). Bottom right image shows the breast region of interest.

initial guess as well as the Tikhonov regularization term. The convergence criterion which is used is determined by the changes in $k(x, y)$ or D_0. Furthermore, performing several runs indicates that using an initial guess higher than 0.01 will not be beneficial as this drastically increases computation time, since Δt is bound by the diffusion and needs to be very small for the time integration method to remain stable.

From literature, it is known that D_0 should take values close to zero, while $k(x, y)$ can fluctuate between -20 to 20 days [19, 46]. Because of this, the Tikhonov regularization term shall be imposed on D_0 to force the algorithm to find values of D_0 to be small. The choice of the Tikhonov regularization term has been somewhat trial and error to investigate which values will produce the best results.

Several experiments have been carried out to investigate the influence of the initial guess, Tikhonov regularization term and to find which final tumour cellularity for time 3 can be taken as the found value. Since the registration still proves to be somewhat of a challenge, the tumour across the time points may not precisely overlap. Due to this, the model produces a large 'error' at time three since the tumour seems to have shifted. Since this error is most likely caused by registration, we quantify the error of the model by looking at the difference between the predicted total tumour cellularity at time 3 and the actual value found from the DWI-MRI scan at time 3.

In total, data of three patients from Erasmus MC has been used in the tests. All patients can be classified as non-responders, as they all have residual tumour cells at time 3. So whilst we cannot currently test the model's performance for responding patients, we can investigate how well the model predicts the number of tumour cells at time 3. We do note that Patient001 and Patient002 respond better to treatment than Patient003 as their tumours have reduced vastly in size between t_1 and t_2. Additionally, we will compare the simple model's predictive capabilities to the complete

model's predictive capabilities to see whether the incorporation of the surrounding tissue increases the accuracy of the prediction.

	D_0	Mean Proliferation	Max Proliferation	Min Proliferation
Simple Model	4.59×10^{-8}	3.862×10^{-2}	2.440×10^{-1}	-2.310×10^{-1}
Complete Model	1.77×10^{-8}	-2.947×10^{-2}	3.493×10^{-2}	-2.749×10^{-1}

Table 6.1: Obtained diffusion D_0 and proliferation rate $k(x, y)$ after calibration for Patient001. Mean proliferation refers to the average of the nonzero elements.

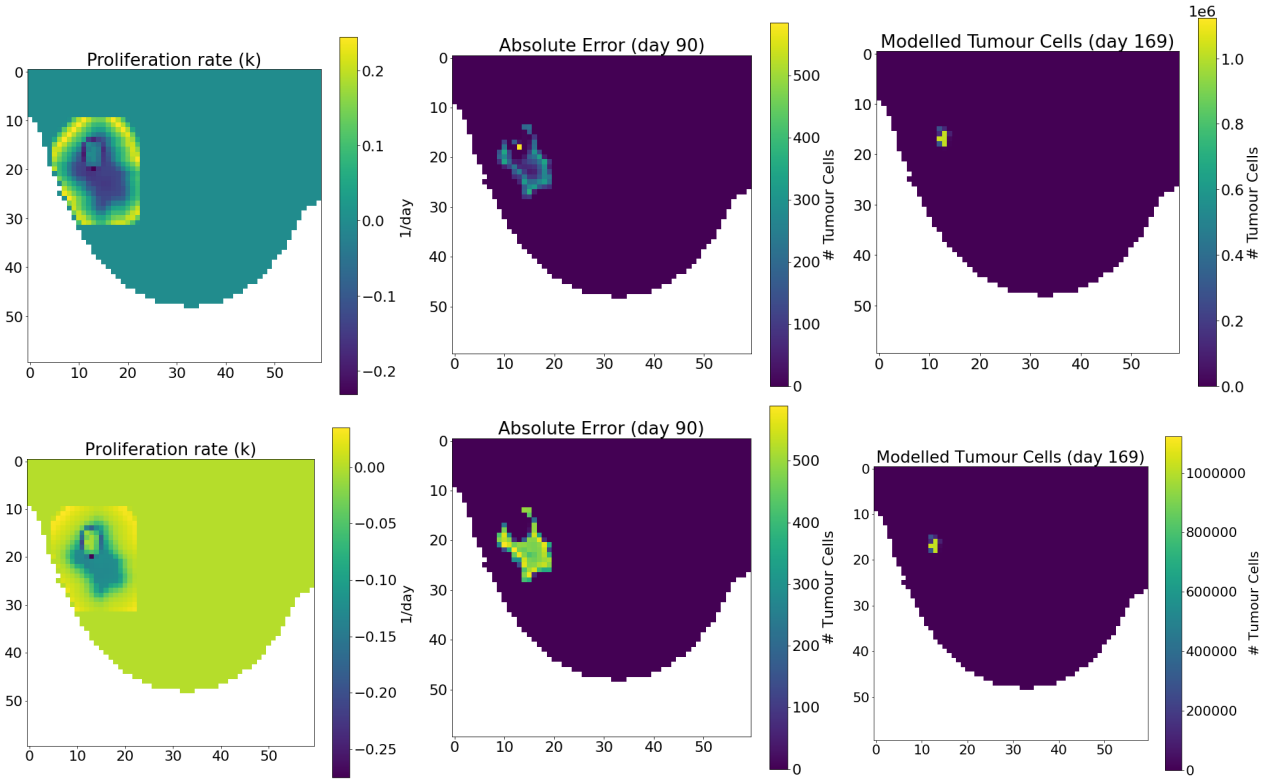

Figure 6.2: Results after parameter calibration for Patient001. Top row of images belong to the simple model, bottom row to the complete model. The left images show the proliferation rate maps obtained after parameter calibration. The middle images show the absolute error between the observed tumour cell number at time 2 and the calculated tumour cell number using the calibrated parameters. The right images show the model tumour cell prediction at time 3.

Several runs have been performed for both the simple as well as the complete model with different initial guesses, convergence criteria and Tikhonov regularization terms. The initial guess was taken as 0.01, 0.001, 0.0001 or $1 \cdot 10^{-4}$, the Tikhonov regularization term was taken as 100, 1 or $1 \cdot 10^{-5}$ and we used the convergence criterion that the rate of change of the independent variables was smaller than $1 \cdot 10^{-3}$ or $1 \cdot 10^{-4}$. In the end, the run which had the closest predicted tumour cell number to the actual tumour cell number at time 3 was chosen as the result. What we observed from doing these different runs was that taking a smaller initial guess was not only faster but tended to generally find better results. The influence of the Tikhonov parameter was indeed that generally, we obtain smaller results for D_0 when the Tikhonov parameter was large and vice versa.

In Table 6.1 and Figure 6.2, the results found for Patient001 can be observed. The obtained

parameters for both the simple model, as well as complete model are in line with the expected values seen in Weis et al. 2017. We see that the parameters are both of the same order of magnitude though the mean proliferation of the simple model is higher. In Figure 6.2, the maps of the proliferation rates can be observed both for the simple model (top) and complete model (bottom). Here, we can see where the change in mean proliferation rate comes from since for the areas outside of the tumour, the simple model determines $k(x, y)$ to be larger than zero. Since there are no tumour cells in these areas, $k(x, y)$ can actually be any value and will not have an effect on the tumour growth. The two figures in the middle show the absolute error which is made when using the calibrated parameters at time 2. We see here that the error for the complete model is generally about twice the error of the simple model, but we note that both errors are very small compared to θ. Lastly, on the right the estimated tumour cells at time 3 are shown modelled using the obtained values for D_0 and $k(x, y)$. As we can see, no difference in these two images is visible. In fact, the difference between the number of tumour cells predicted by the simple and complete model is only about 1,000. This is in line with what we could expect after the results from the in silico experiments in the previous chapter. There, we saw that the incorporation of the surrounding tissue in the model with the current carrying capacity obtained from the MRI scans was negligible.

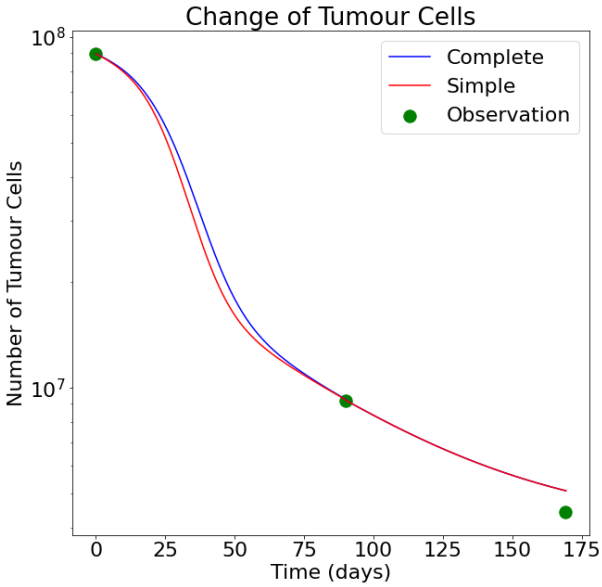

Figure 6.3: Change in the number of tumour cells over the course of the three MRI scans for Patient001. In blue the complete model's tumour cell evolution is shown, in red the simple model. The actual observations obtained from the MRI scans are shown in green.

Nevertheless, in Table 6.4 the actual tumour cell number along with the predicted tumour cell number from both models at time 3 are shown. Here, we see that currently, the model has an error of about 600,000 tumour cells. To put this further into perspective, a plot is made to show the change in tumour cells over the course of the three MRI scans. The result for Patient001 can be seen in Figure 6.3, where also the observations from the MRI scans are shown. As we can see, the complete and simple model follow the same trajectory when predicting the tumour cell number at time 3. Also, whilst an error of 600,000 tumour cells at time 3 remains large, in this figure we can see that the model shows a good downward trend in tumour cells. This particular patient was responding quite well to treatment, with the number of tumour cells from time 1 reducing drastically from 89 million to about 9 million at time 2.

6.1.2. Patient002 and Patient003

For Patient002 and Patient003, the same type of runs have been performed as before. The results of the best experiment for Patient002 can be found in Table 6.2 and for Patient003 in Table 6.3. For Patient002, we see that the proliferation rate is again in the same order of magnitude for both the simple as well as complete model. For the diffusion, the difference is larger. In the appendix, further images are shown for both patients regarding their tumour sizes at time 1, 2 and 3 as well as the proliferation rate maps and modelled tumour cells. In Figure 6.4, the change of tumour cells is shown for both Patient002 (left) and Patient003 (right). Patient002 also responds to treatment quite well, with the number of tumour cells reducing from 234 million at time 1 to 24 million at time 2. Again, both model predictions are almost exactly the same for time 3, with both underestimating the number of tumour cells, in this case. The exact values of the model predictions at time 3 can be observed in Table 6.4. It is important to note that the registration for this patient was somewhat of a challenge due to the first MRI scans being made at a different hospital. This caused not only the resolution to be different, but the shape of the breast was also very different.

	D_0	Mean Proliferation	Max Proliferation	Min Proliferation
Simple Model	2.699×10^{-6}	-3.059×10^{-2}	2.744×10^{-1}	-3.515×10^{-1}
Complete Model	1.638×10^{-11}	-2.303×10^{-2}	2.295×10^{-1}	-1.833×10^{-1}

Table 6.2: Obtained diffusion D_0 and proliferation rate $k(x, y)$ after calibration for Patient002. Mean proliferation refers to the average of the nonzero elements.

For Patient003, the model has much more difficulty with accurately predicting the number of tumour cells at time 3. In fact, the predicted number of tumour cells actually increases after time 2. One of the observations we make is that this patient did not respond to treatment quite as well as Patient001 and Patient003. The number of tumour cells only reduce from 84 million cells at time 1 to 68 million tumour cells at time 2. Furthermore, this patient was the most challenging regarding the registration of the tumour. Although the segmentation was performed by the radiologist, after registration this could be somewhat distorted and was attempted to be reconstructed by me. This could have led to voxels being wrongfully classified as tumurous. Patient001 and Patient002 had quite distinct tumours which lit up, but this was not the case for Patient003. This made the shape of the tumour change from time 1 to time 2 and time 3 quite a bit as can be observed in the appendix. We do note that the calibrated parameters are again in line with what would be expected from literature values.

	D_0	Mean Proliferation	Max Proliferation	Min Proliferation
Simple Model	5.086×10^{-3}	-1.644×10^{-1}	1.058×10^{-1}	-1.828
Complete Model	5.093×10^{-3}	-8.271×10^{-2}	1.063×10^{-1}	-8.079×10^{-1}

Table 6.3: Obtained diffusion D_0 and proliferation rate $k(x, y)$ after calibration for Patient003. Mean proliferation refers to the average of the nonzero elements.

In the end, for Patient001 and Patient002, the model's predictive capabilities show promise. These patients both behaved quite similarly in the fact that they both had a drastic reduction in tumour cell number from time 1 to time 2. For Patient003, the model could not accurately predict the number of tumour cells and the tumour was even predicted to grow from time 2 onward.

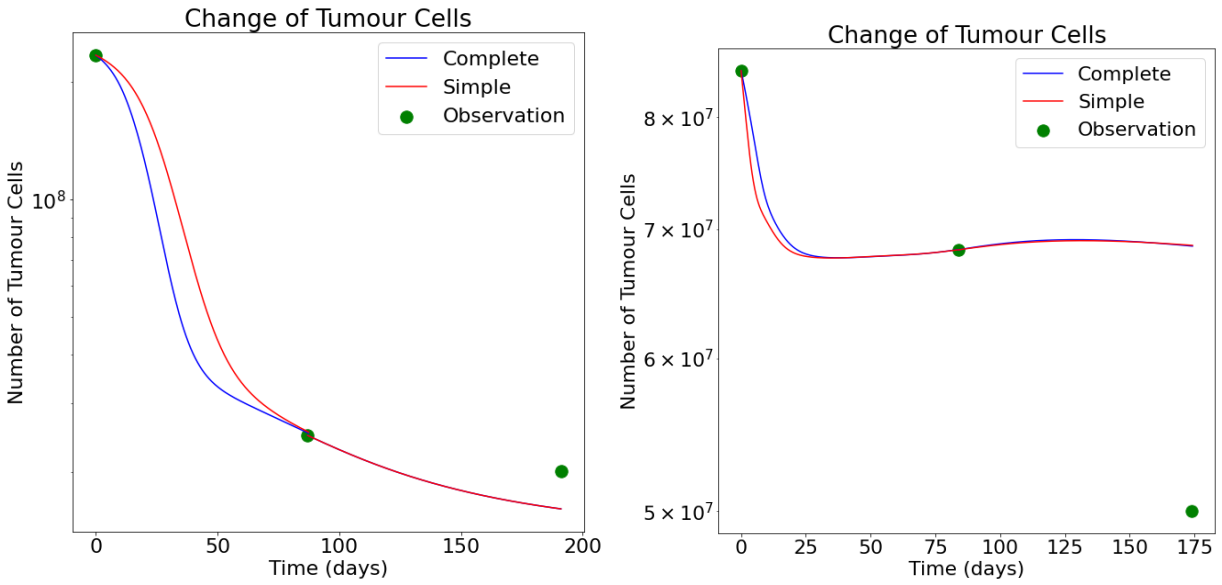

Figure 6.4: Change in the number of tumour cells over the course of the three MRI scans for Patient002 (left) and Patient003 (right). In blue the complete model's tumour cell evolution is shown, in red the simple model. The actual observations obtained from the MRI scans are shown in green.

	Observed	Simple Model	Complete Model
Patient001	4,422,723	5,087,818	5,088,914
Patient002	20,112,640	16,099,977	16,100,214
Patient003	50,020,596	68,668,713	68,607,973

Table 6.4: Number of tumour cells at time 3 found from DWI-MRI scans as well as both model predictions.

6.2. Reduced Number of Slices

As could be seen from Table 6.4, the difference between the simple model prediction and complete model predictions are not big. This is in line with the expectation one would have from the previous chapter, where the influence of the incorporation of the linear elasticity was explored. One of the observations made, is that the literature makes use of a much higher carrying capacity for their 2D model calculations [20, 44, 45]. As seen in the previous chapter, this would provide a much bigger influence of the surrounding tissue. With this knowledge at hand, a closer look has been taken at the available literature to investigate how they came to a higher carrying capacity. We note that whilst we have made use of the original number of slices/resolution provided by the MRI scanner, the data used in the literature is of a much coarser state. Instead of using 120 slices in the third dimension, they only use about 20-30. This, in turn, will cause the carrying capacity to become much higher, and whilst we still do model calculations in two dimensions, the growth of the tumour will have a much higher impact on the surrounding tissue. As such, another experiment is done. Since Patient001 was the most ideal patient in terms of tumour visibility as well as data structure, this patient will be used for the experiment. In the experiment, the whole preprocessing pipeline is again performed, however this time with only 32 slices instead of 120 slices in the third dimension. These slices were now 6.5 mm thick. Using these slices and again by downsampling by a factor 3, we now have a carrying capacity of $4.21 \cdot 10^6$ per voxel. In the other two dimensions we have the same resolution

as in the previous section. This means that we would expect a more significant difference in the predictions of the simple and complete model. Again, the central slice is taken of the tumour for the experiment.

	D_0	Mean Proliferation	Max Proliferation	Min Proliferation
Simple Model	8.260×10^{-3}	-2.005×10^{-1}	2.067×10^{-1}	-2.240
Complete Model	2.049×10^{-2}	-2.733×10^{-1}	1.734×10^{-1}	-5.006

Table 6.5: Obtained diffusion D_0 and proliferation rate $k(x, y)$ after calibration for Patient001 with thicker silces. Mean proliferation refers to the average of the nonzero elements.

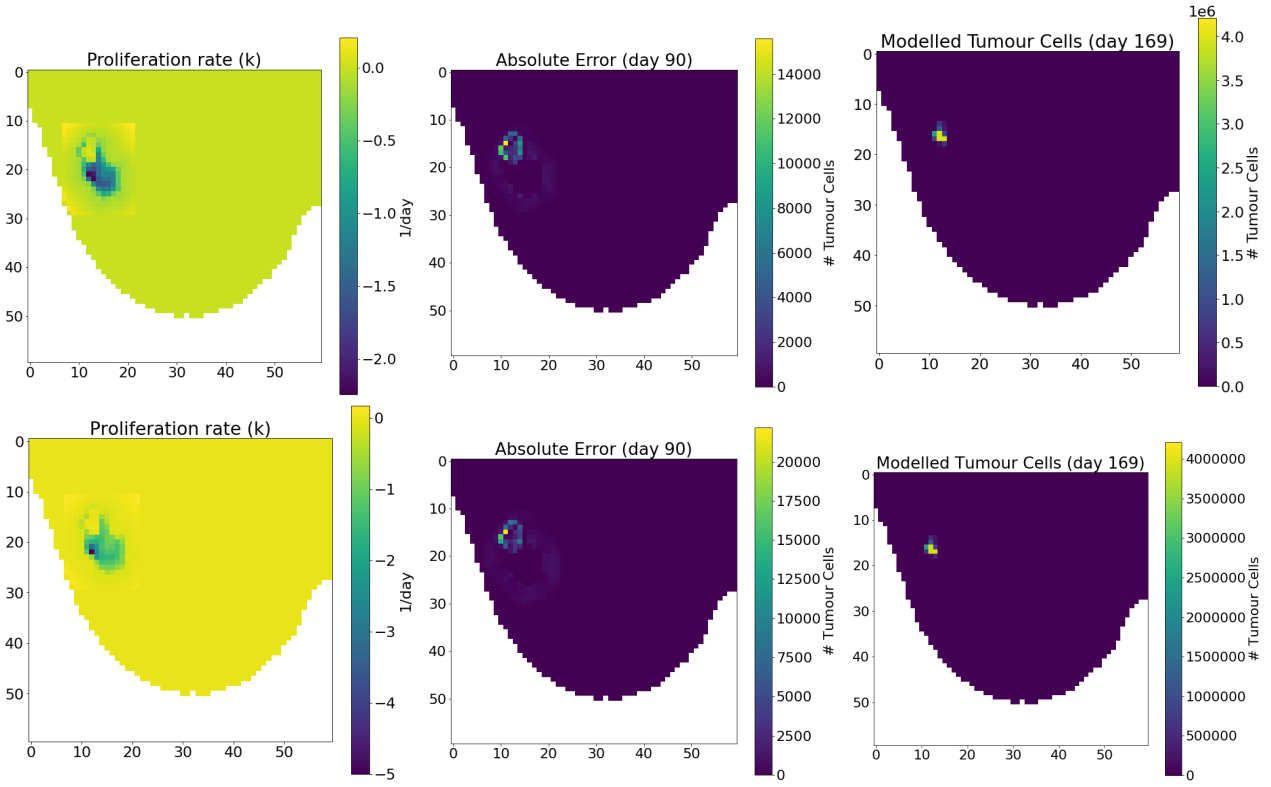

Figure 6.5: Results after parameter calibration for Patient001 using thicker slices. Top row of images belong to the simple model, bottom row to the complete model. The left images show the proliferation rate maps obtained after parameter calibration. The middle images show the absolute error between the observed tumour cell number at time 2 and the calculated tumour cell number using the calibrated parameters. The right images show the model tumour cell prediction at time 3.

The obtained parameters can be observed in Table 6.5. We can see that for the complete model, the diffusion as well as proliferation rate is larger than for the simple model. This is what we would expect as the incorporation of the surrounding tissues' stiffness causes the tumour to grow and also decay slower for the same proliferation rates in the simple model. Furthermore, in Figure 6.5, the proliferation rate map along with the made calibration error and modelled tumour cells at time 3 can be observe again. We see that for both the simple as well as for the complete model, the errors are in the same order of magnitude. Additionally, there is a slight difference in the modelled tumour cell number at time 3, though it is difficult to visually see this. Therefore, in Figure 6.6, the change

of tumour cell number can be seen over the course of patient's treatment. What we can observe from this figure, is that indeed there is a difference in the complete models prediction compared to the simple models prediction. In fact, the complete model performs slightly better than the simple model. In Table 6.6, the exact number of actual tumour cells along with predicted tumour cells can be observed. Note that the number of tumour cells is higher than before, since we have taken thicker slices, which therefore contain more tumour cells.

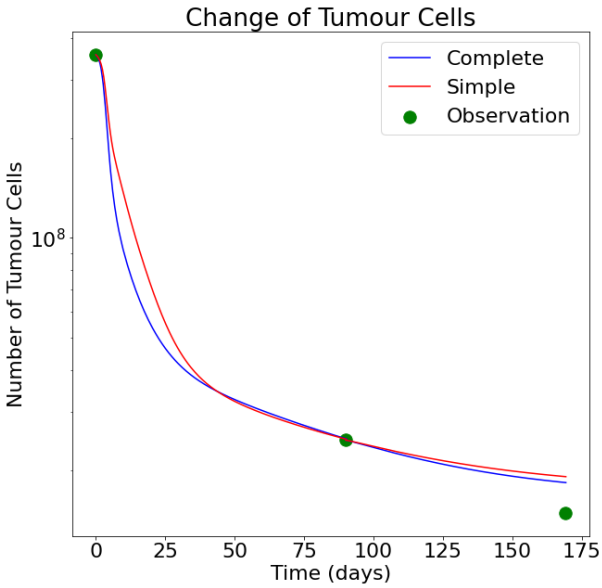

Figure 6.6: Change in the number of tumour cells over the course of the three MRI scans for Patient001 with reduced slices. In blue the complete model's tumour cell evolution is shown, in red the simple model. The actual observations obtained from the MRI scans are shown in green.

	Observed	Simple Model	Complete Model
$\text{Patient001}_{\text{reduced}}$	14,852,145	19,120,975	18,347,708

Table 6.6: Number of tumour cells at time 3 found from DWI-MRI scans as well as both model predictions.

What we observe from these experiments, is that the choice in slice thickness can have a great influence on the model's performance and especially on the influence of the surrounding tissue. This is due to the model calculations being performed in 2 dimensions. In the end, the complete model shows potential for predicting the tumour cell number for responding patients. The predictions for Patient001 and Patient002 were much better than for Patient003, which had a less distinctly defined tumour and responded to chemotherapy less well. However, the current model can be expanded and refined further to, hopefully, increase the accuracy of its predictive abilities.

7

Future Improvements

One of the most important things to note is that the current model which has been implemented and investigated in this thesis, still has many more refinements and expansions to become more accurate.

7.1. Incorporation of Chemotherapy

One of the most important factors which has not currently been incorporated into the model, is the chemotherapy. The chemotherapy which has been administered to these patients has a different influence depending on the vascularity of the tumour. Due to time constraints, this is one of the most important things we have not yet taken into consideration. Whenever a tumour grows beyond about 2 mm^2, tumour angiogenesis occurs [14]. This means that the tumour starts to grow its own blood vessels to increase its nutrients and oxygen causing it to grow even further. The vascularity is also what causes us to be able to identify the tumour as it lights up using a contrast agent and DCE-MRI scans. This means that the DCE-MRI can be used further to identify the vascularity of the tumour. Since the chemotherapy will move in a similar way through the tumour's blood vessels, it can be used to determine the amount of chemotherapy concentration in the tumour. The incorporation of the chemotherapy will result in the following reaction-diffusion equation:

$$\frac{\partial N(\bar{x},t)}{\partial t} = \underbrace{\nabla \cdot (D \nabla N(\bar{x},t))}_{\text{Diffusion}} + \underbrace{k(\bar{x}) N(\bar{x},t) \left(1 - \frac{N(\bar{x},t)}{\theta}\right)}_{\text{Proliferation}} - \underbrace{\alpha C^{drug}_{tissue}(\bar{x},t) N(\bar{x},t)}_{\text{Chemotherapy}} \tag{7.1}$$

In this case, the proliferation rate $k(x, y)$ would actually represent the tumour's growth in case of no chemotherapy and therefore be positive. Since we had no other factor representing tumour decay, our proliferation rate could be negative to represent this. The parameter α is a global parameter that describes the efficacy of the specific chemotherapy used. The chemotherapy concentration C^{drug}_{tissue} could be found by fitting the extended Kety-Tofts model to the DCE-MRI scans [17, 19, 20].

$$C_{tissue}(\bar{x},t) = K^{trans}(\bar{x}) \int_0^t \left(C_{plasma}(u) \cdot \exp\left(-\frac{K^{trans}(\bar{x})}{v_e(\bar{x})}(t-u) \right) \right) du + v_p(\bar{x}) C_{plasma}(t) \tag{7.2}$$

In this equation, C_{tissue} and C_{plasma} are the concentrations of the contrast agent in the tissue and plasma respectively. K^{trans} is the volume transfer constant from the plasma space to the tissue space and v_e is the volume fraction of the extravascular extracellular space. Lastly, v_p is the volume fraction of the plasma space. Using DCE-MRI scans, the parameters K^{trans}, v_e and v_p can be estimated for each individual patient [17]. Several papers exist such as Jarrett et al. 2018 and Jarrett

et al. 2020 who discuss the effects of incorporating the chemotherapy and show that it increases the accuracy of the model predictions. This would be the next step in modelling the patient-specific tumour cell evolution.

7.2. Further Improvements and Refinements

Another expansion of the current model is to implement it in 3-dimensions. In this current research, we made use of the central tumour slice to model the tumour growth. The results showed that with this current approach, the thickness of the slice chosen has a great influence in the effects of the surrounding tissue on the tumour growth. The thicker the slices are taken, the larger the carrying capacity becomes and in turn the more the surrounding tissue inhibits the growth/decay of the tumour. Therefore, the incorporation of tumour cell growth in the three-dimensions will likely provide more accurate predictions [46]. The extension of the currently implemented 2-dimensional model to a 3-dimensional model should be straightforward. However, computational speed enhancements should be performed as the parameter calibration already takes more than an hour for the downsampled 2-dimensional model.

One of the first refinements that could be done is taking a closer look at the registration of the images. In this research, the ITKElastix toolkit was used to register both inter-scan and intra-scan [23]. For both the rigid and nonrigid registration, the default parametermap was used. However, it became clear after registration that the tumour was not necessarily in the same slices for all three time points. For patient 3 for example, the central tumour slice was slice 73 at time 1, slice 72 at time 2 but slice 64 at time 3. For the model calibration and validation, it is very important that the registration is carried out correctly as we are calculating the number of tumour cells on a voxel-by-voxel basis. Several other parameter maps exist, which should be investigated to see whether these might perform better. Additionally, the setting 'FinalGridSpacing' can be adjusted so that during the registration, the image cannot be distorted too little or too much. Lastly, in the ITKElastix toolkit, one could perhaps also use an additional mask for the tumour to make sure that not only the contour of the breast is correctly aligned but also the tumour within the breast is registered correctly.

During this thesis, the availability of patient data was also one of the difficulties to overcome. In the end, 3 usable patient's data were provided by Erasmus MC. However, this subset remains far too small to statistically give insight into how often the complete model might outperform the simple model and vice versa, as was done in previous literature [45]. Testing the model validity more elaborately could shed light on which kind of patients the model performs best. As was seen in the previous chapter, the model came quite close to the actual tumour cell number for Patient001 and Patient002, but not for Patient003. This might be the case because Patient003 responded the least to treatment compared to the other patients. Further investigation with different patients, e.g. some of whom do not have any residual tumour at time 3, could give other insights into which kind of responding patients the model can predict the outcome for best.

One of the difficulties in finding suitable patient data was the unavailability of a third MRI scan before surgery. This MRI scan is vital for the validation of the model. However, providing more than three MRI scans could also increase the model's predictive accuracy. Currently, the parameter calibration is ill-posed. In each voxel, there are 2 unknowns, i.e. the global parameter D_0 and the spatial parameter $k(x, y)$, but there is only 1 measurement. This meant that there are an infinite number of possible solutions. To solve this problem, we made use of a Tikhonov regularization term. However, by providing more scans, more measurements are available, making it more accurate to calibrate the model parameters. In addition to this, the currently used nonlinear least squares optimization algorithm used was Levenberg-Marquardt. Recent literature uses a Polak-Robiere conjugate gradient algorithm for the parameter calibration [46]. For the in silico experiments performed in this paper, their approach shows good accuracy.

Next, the assignment of other model parameters can be revised. Several of these, λ, E, etc. have been taken as literature values as could be seen in Table 2.2. For the stiffness of the fibroglandular, adipose and tumour tissues within the breast, literature values were taken. A more patient-specific approach would be to use MRI-based elasticity imaging methods to increase the accuracy of the estimates of spacial elasticity on an indiviual basis. Modality independent elastography (MIE) could be used for this approach [45]. One other limiting assumption is that the proliferation rate and carrying capacity are both constant in time. For the proliferation rate, this is a current simplification since it is impractical to perform enough MRI scans at different time points to accurately create a temporal proliferation rate. The same holds for the carrying capacity, where a more realistic approach would be to let the carrying capacity change over time. Additionally, for the calculation of θ, the tumour cells are assumed to be spherical and with the same radius. However, it is known that cancerous cells have an irregular shape and are not all the same size [24]. To incorporate this would require an additional model equation for θ such as coupling the carrying capacity to the vascularity of the tumour [16]. Other parameters which could be improved upon are the γ which couples the stress on the tissue to the diffusion of tumour cells. This parameter has been empirically derived in literature, so further investigation of this parameter might be beneficial.

Lastly, further improvements on the model can include investigating the current level of ambiguity for the cause of changes in ADC. Not only tumour cellularity causes fluctuations in the ADC values, but also cell size or cell membrane permeability can be factors [16, 19]. In this research, the current assumption was that whenever a voxel was classified as tumorous, the only type of tissue in this voxel was tumour cells. As such, the number of tumour cells within a voxel was only depending on the ADC values and the carrying capacity. However, recent literature suggests that the incorporation of extravascular extracellular volume fractions can increase the accuracy of estimating the number of tumour cells when compared to only using ADC values [1]. This means instead of using equation (2.6) for the estimation of number of tumour cells, one can use:

$$N(\bar{x},t) = \theta \left(\frac{ADC_w - ADC_{min}(\bar{x},t)}{ADC_w - ADC(\bar{x},t)} \right) v_{TC}$$

Where $v_{TC} = 1 - v_e - v_p$ which are derived via the Kety-Tofts equation.

8

Conclusion

In this chapter, the research and analysis shall be summarized and an answer will be provided to the main question *Can a mathematical model of tumour growth predict patient-specific response for HER2+ breast cancer patients?* Additionally, the most important extensions to the model for future improvement will be discussed.

In this thesis, we presented a mechanically coupled reaction-diffusion model which could integrate quantitative magnetic resonance imaging data to predict the tumor growth of an individual patient. Prior to testing the model, a preprocessing pipeline was constructed to extract all necessary information from the MRI data such as tumour cell number, segmentation of tissues. and domain of the breast. We performed several experiments on data provided by Erasmus Medical Centre, to investigate the mechanically coupled reaction-diffusion model versus the non-mechanically coupled model. By performing these experiments, we saw that for patients who responded well to treatment, the model was able to predict the downward trend in tumour cellularity. For the patient who did not respond well to treatment, the model had much more difficulty in finding an accurate estimate for time 3. Though it is important to note that this patient had a difficult tumour to segment and therefore registration proved to be a challenge. This could have both contributed to the error from the model. The current model should be tested on a more diverse patient cohort to investigate for which kinds of patients the model performance is best.

However, we do note that there was barely any difference in the complete model's prediction versus the simple model's prediction. This was caused by taking a high resolution in the third dimension. The model was implemented in 2-dimensions, but the number of tumour cells in a voxel depends on the thickness of the slice taken. When experimenting with thicker slices, which meant that there are more tumour cells in a voxel, a larger effect of the surrounding tissue could be observed. This resulted in a better prediction for the complete mechanically coupled model versus the simple reaction-diffusion model. Although, it is important to note this experiment was only performed for one patient. Again, it is important to experiment with this on more patients to see whether the mechanically coupled model is indeed statistically better at predicting the number of tumour cells than the non-mechanically coupled model.

Several limitations of this study have been discussed. One of the major limitations at this current stage is not incorporating the chemotherapy administered to the patient. In the current model, the proliferation rate can be both positive or negative to denote the tumour cell growth or decay, respectively. In reality, the tumour would try to grow, i.e. $k(x, y)$ is positive, and the decay is strictly because of the chemotherapy given to the patient. Another limitation is that the model was only implemented in 2-dimensions with only the central tumour slice instead of in 3-dimensions. This meant

that the slice thickness determined whether the surrounding tissue had more or less effect on the tumour growth. Including both of these expansions will most likely result in better model performance. Another important addition to the model would be an additional MRI scan. The current parameter calibration is an underdetermined problem since there are 2 unknowns in each voxel but only one measurement. Incorporating an additional MRI scan for the calibration, will result in better estimates for the patient-specific parameters.

The ultimate goal of this project is to create a model which is able to accurately predict the number of cycles of chemotherapy a HER2+ breast cancer patient will need to achieve complete pathological response. In this thesis, we provided the first steps to achieving this goal. At this current stage, we are unable to give an accurate prediction in the number of cycles since the chemotherapy is not yet incorporated into the model. However, in this thesis, we have shown that the reaction-diffusion model coupled to surrounding tissue shows potential to be able to predict the change in overall tumour cellularity for a patient.

A

Appendix

The displacements obtained solving Equation (2.4) at time 20 can be seen in Figure A.1. These displacements are used to calculate the von Mises stress as seen in Figure 5.11.

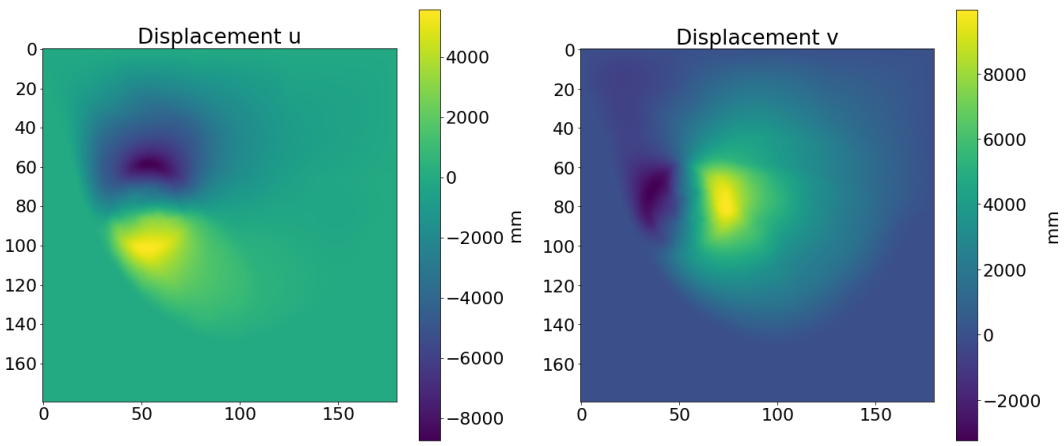

Figure A.1: Displacements calculated solving equation 2.4. U denotes the displacement in the $x-$direction and v the displacements in the $y-$direction.

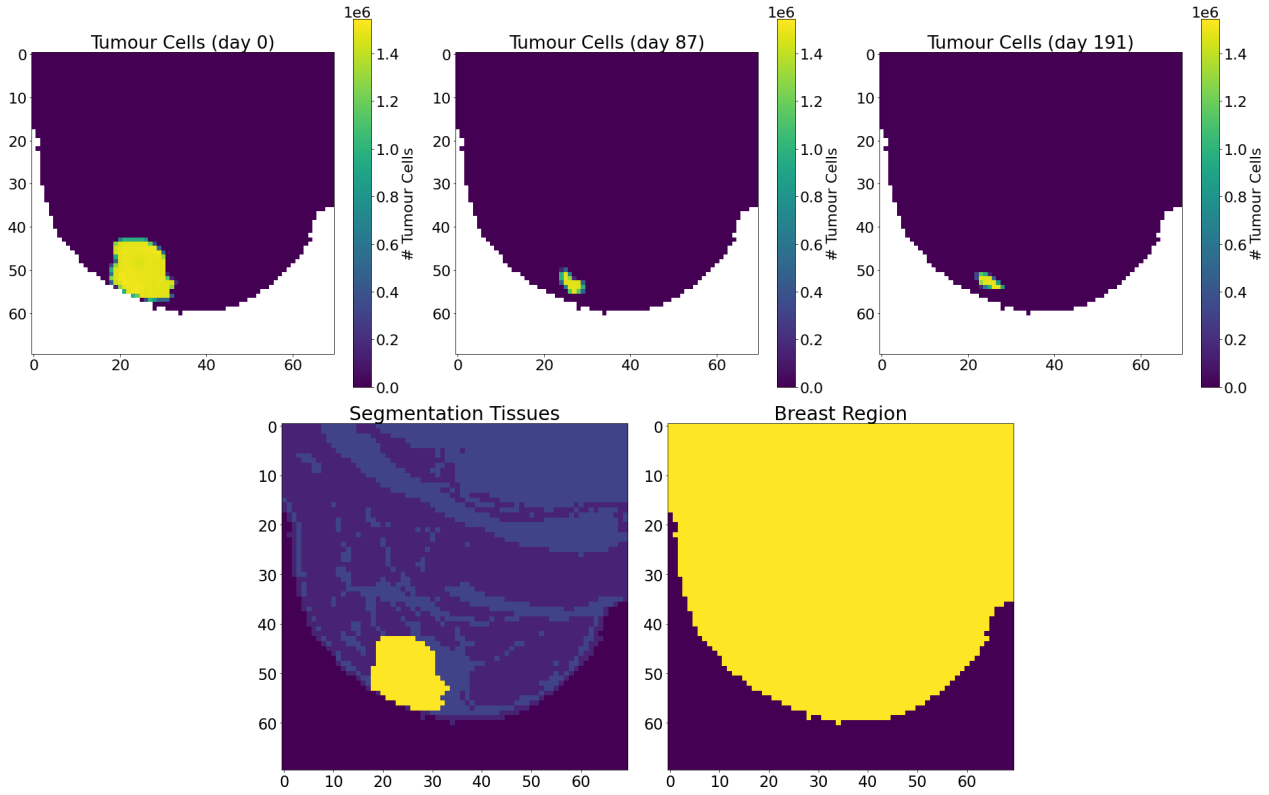

Figure A.2: Tumour cells of Patient002 obtained from the DWI-MRI scans at the three time points.

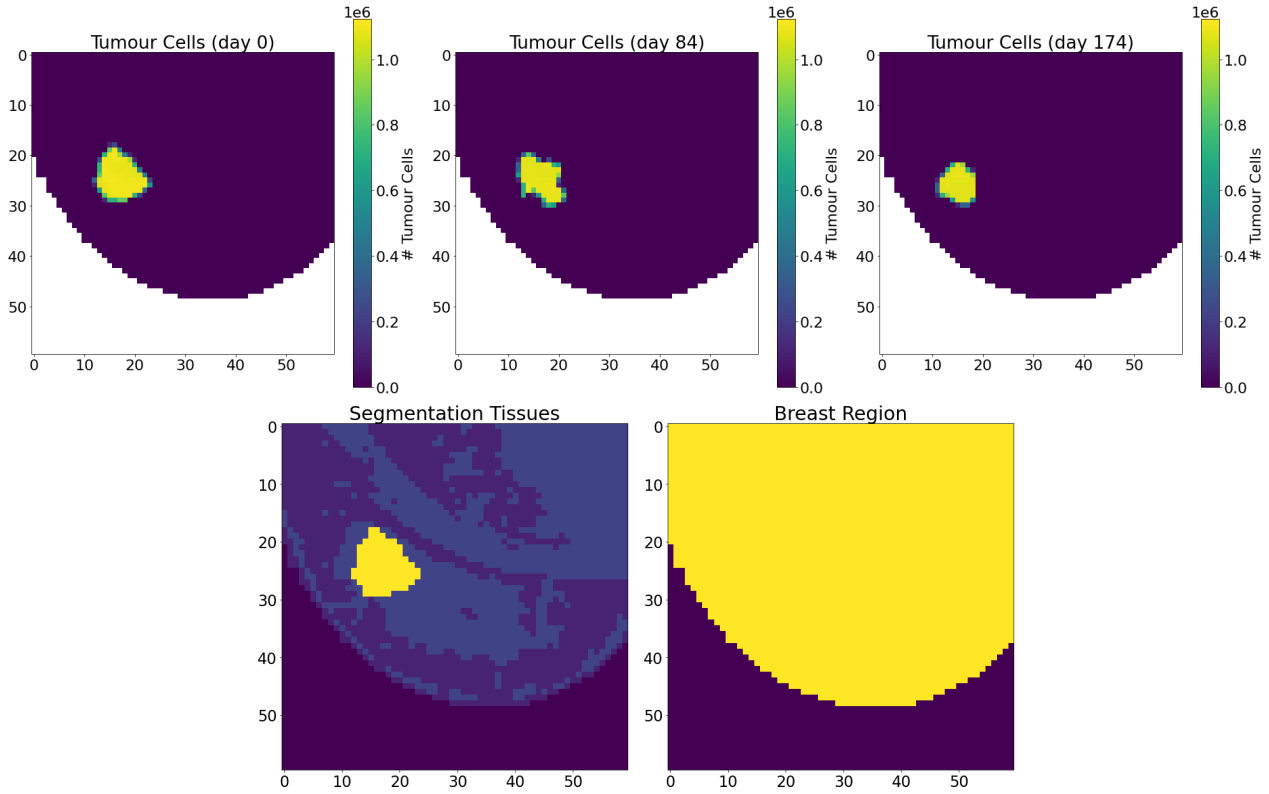

Figure A.3: Tumour cells of Patient003 obtained from the DWI-MRI scans at the three time points.

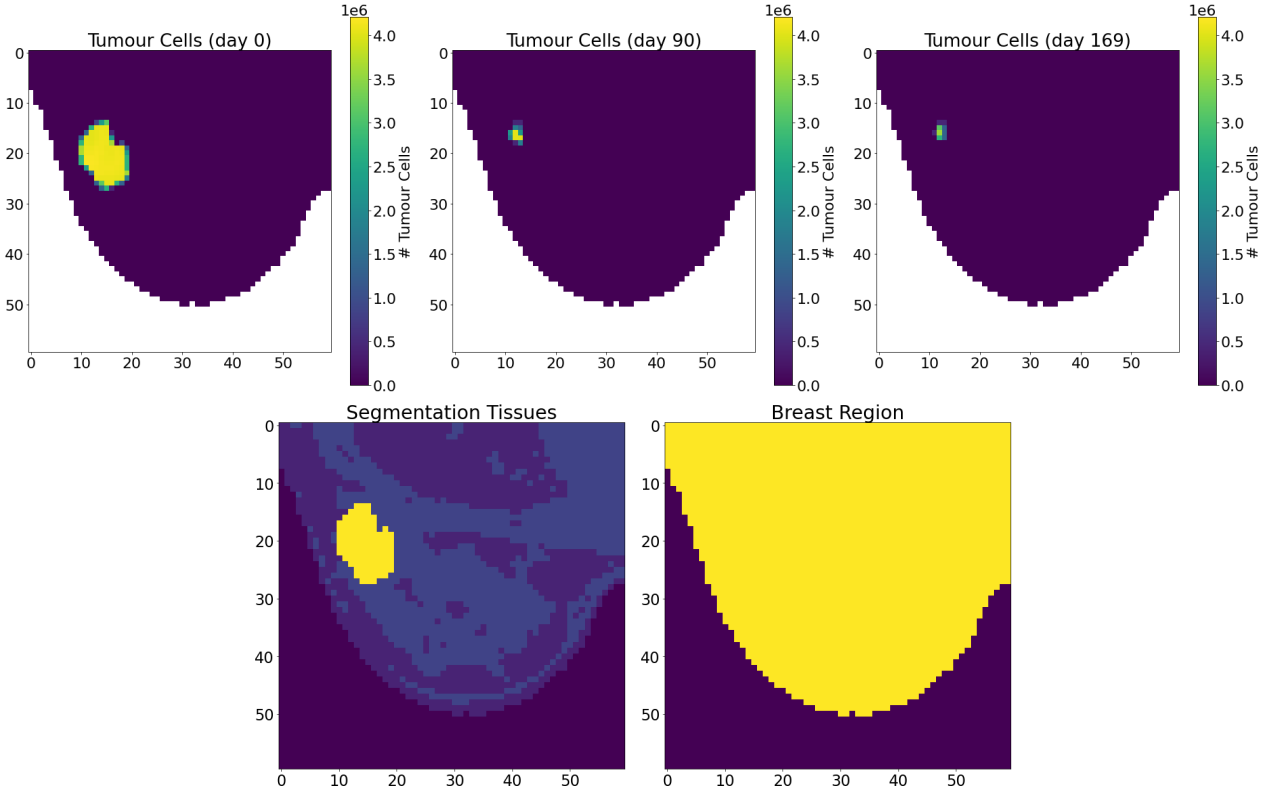

Figure A.4: Tumour cells of Patient001 with reduced slices obtained from the DWI-MRI scans at the three time points.

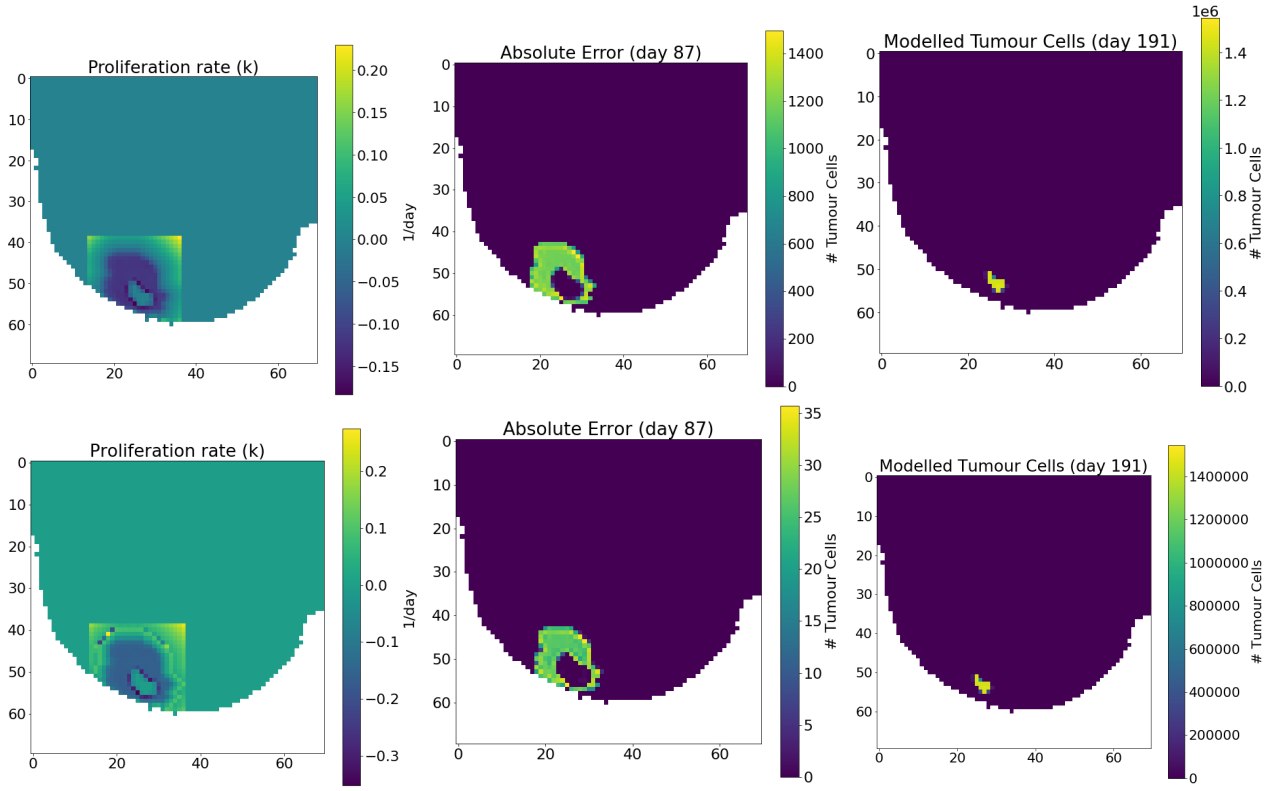

Figure A.5: Results after parameter calibration for Patient002. Top row of images belong to the simple model, bottom row to the complete model. The left images show the proliferation rate maps obtained after parameter calibration. The middle images show the absolute error between the observed tumour cell number at time 2 and the calculated tumour cell number using the calibrated parameters. The right images show the model tumour cell prediction at time 3.

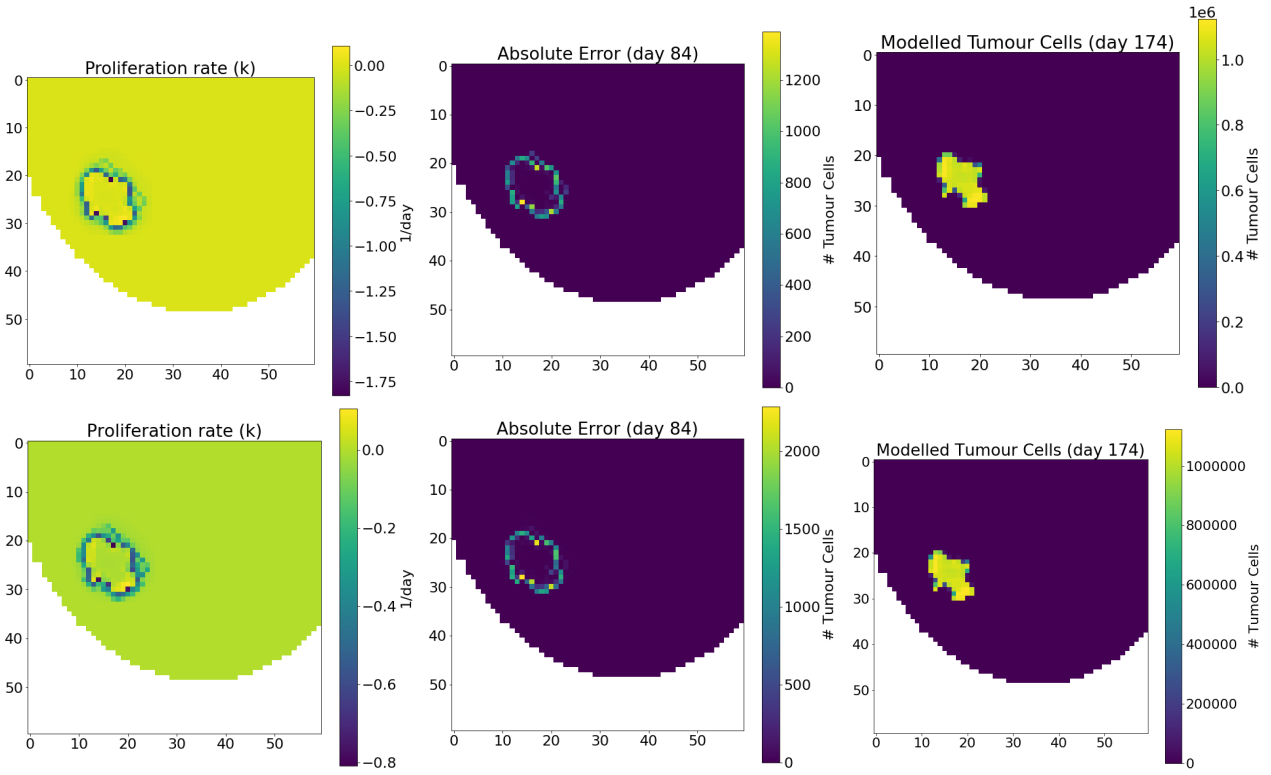

Figure A.6: Results after parameter calibration for Patient003. Top row of images belong to the simple model, bottom row to the complete model. The left images show the proliferation rate maps obtained after parameter calibration. The middle images show the absolute error between the observed tumour cell number at time 2 and the calculated tumour cell number using the calibrated parameters. The right images show the model tumour cell prediction at time 3.

Bibliography

1 Atuegwu, N. C., Arlinghaus, L. R., Li, X., Chakravarthy, A. B., Abramson, V. G., Sanders, M. E., & Yankeelov, T. E. (2013). Parameterizing the logistic model of tumor growth by dw-mri and dce-mri data to predict treatment response and changes in breast cancer cellularity during neoadjuvant chemotherapy. *Translational oncology*, *6*(3), 256–264.

2 Atuegwu, N. C., Arlinghaus, L. R., Li, X., Welch, E. B., Chakravarthy, B. A., Gore, J. C., & Yankeelov, T. E. (2011). Integration of diffusion-weighted mri data and a simple mathematical model to predict breast tumor cellularity during neoadjuvant chemotherapy. *Magnetic resonance in medicine*, *66*(6), 1689–1696.

3 Bhattacharyya, M., Ryan, D., Carpenter, R., Vinnicombe, S., & Gallagher, C. (2008). Using mri to plan breast-conserving surgery following neoadjuvant chemotherapy for early breast cancer. *British journal of cancer*, *98*(2), 289–293.

4 Bialecki, B., & Karageorghis, A. (2014). Finite Difference Schemes for the Cauchy–Navier Equations of Elasticity with Variable Coefficients. *Journal of Scientific Computing*, *62*(1), 78–121. https://doi.org/10.1007/s10915-014-9847-8

5 Borstkanker: cijfers en feiten. (n.d.). https://www.pinkribbon.nl/over-borstkanker/cijfers-en-feiten.html

6 Boyle, P., & Levin, B. (2008). *World cancer report 2008*. IARC Press.

7 Breast cancer - introduction. (2020). https://www.cancer.net/cancer-types/breast-cancer/introduction

8 Chamseddine, I. M., & Rejniak, K. A. (2020). Hybrid modeling frameworks of tumor development and treatment. *Wiley Interdisciplinary Reviews: Systems Biology and Medicine*, *12*(1), e1461.

9 Chen, W., Giger, M. L., & Bick, U. (2006). A fuzzy c-means (fcm)-based approach for computerized segmentation of breast lesions in dynamic contrast-enhanced mr images1. *Academic radiology*, *13*(1), 63–72.

10 Date, S. (2021). A Guide to Building Nonlinear Least Squares (NLS) Regression Models | Towards Data Science. https://towardsdatascience.com/a-guide-to-building-nonlinear-least-squares-nls-regression-models-310b97a7baeb

11 Fox, J. (2015). *Applied Regression Analysis and Generalized Linear Models*. SAGE Publications.

12 Gonzalez, R., & Woods, R. (2017). *Digital Image Processing, Global Edition* (4th edition). Pearson Education Limited.

13 Häggström, M. (2019). *Ducts and lobules, the main locations of breast cancers.*

14 Hillen, F., & Griffioen, A. W. (2007). Tumour vascularization: sprouting angiogenesis and beyond. *Cancer and Metastasis Reviews*, *26*(3-4), 489–502. https://doi.org/10.1007/s10555-007-9094-7

15 Hormuth, D. A., Eldridge, S. L., Weis, J. A., Miga, M. I., & Yankeelov, T. E. (2018). Mechanically coupled reaction-diffusion model to predict glioma growth: Methodological details. *Cancer systems biology* (pp. 225–241). Springer.

16 Hormuth, D. A., Jarrett, A. M., Feng, X., & Yankeelov, T. E. (2019). Calibrating a predictive model of tumor growth and angiogenesis with quantitative mri. *Annals of biomedical engineering*, *47*(7), 1539–1551.

17 Hormuth, D. A., Jarrett, A. M., Lima, E. A., McKenna, M. T., Fuentes, D. T., & Yankeelov, T. E. (2019). Mechanism-based modeling of tumor growth and treatment response constrained by multiparametric imaging data. *JCO clinical cancer informatics*, *3*, 1–10.

18 Jaroudi, R., Åström, F., Johansson, B., & Baravdish, G. (2019). Numerical simulations in 3-dimensions of reaction–diffusion models for brain tumour growth. *International Journal of Computer Mathematics*, *97*(6), 1151–1169. https://doi.org/10.1080/00207160.2019.1613526

19 Jarrett, A. M., Hormuth, D. A., Barnes, S. L., Feng, X., Huang, W., & Yankeelov, T. E. (2018). Incorporating drug delivery into an imaging-driven, mechanics-coupled reaction diffusion model for predicting the response of breast cancer to neoadjuvant chemotherapy: Theory and preliminary clinical results. *Physics in Medicine & Biology*, *63*(10), 105015.

20 Jarrett, A. M., Hormuth II, D. A., Wu, C., Kazerouni, A. S., Ekrut, D. A., Virostko, J., Sorace, A. G., DiCarlo, J. C., Kowalski, J., Patt, D. et al. (2020). Evaluating patient-specific neoadjuvant regimens for breast cancer via a mathematical model constrained by quantitative magnetic resonance imaging data. *Neoplasia*, *22*(12), 820–830.

21 Kelly, P. (n.d.). Lecture Notes: An introduction to Solid Mechanics. https://pkel015.connect.amazon.auckland.ac.nz/SolidMechanicsBooks/index.html

22 Kelly, P. (2015). Linear Elasticity. *Mechanics Lecture Notes: An introduction to Solid Mechanics.*

23 Klein, S., Staring, M., Murphy, K., Viergever, M., & Pluim, J. (2010). elastix: A Toolbox for Intensity-Based Medical Image Registration. *IEEE Transactions on Medical Imaging*, *29*(1), 196–205. https://doi.org/10.1109/tmi.2009.2035616

24 Lansdowne, L. E. (2021). Cancer Cells vs Normal Cells. https://www.technologynetworks.com/cancer-research/articles/cancer-cells-vs-normal-cells-307366

25 Lee, J., & Jeong, M. S. (2017). Stability of finite difference schemes on the diffusion equation with discontinuous coefficients.

26 Li, X., Arlinghaus, L. R., Ayers, G. D., Chakravarthy, A. B., Abramson, R. G., Abramson, V. G., Atuegwu, N., Farley, J., Mayer, I. A., Kelley, M. C. et al. (2014). Dce-mri analysis methods for predicting the response of breast cancer to neoadjuvant chemotherapy: Pilot study findings. *Magnetic resonance in medicine*, *71*(4), 1592–1602.

27 Li, X., Welch, E. B., Arlinghaus, L. R., Chakravarthy, A. B., Xu, L., Farley, J., Loveless, M. E., Mayer, I. A., Kelley, M. C., Meszoely, I. M. et al. (2011). A novel aif tracking method and comparison of dce-mri parameters using individual and population-based aifs in human breast cancer. *Physics in Medicine & Biology*, *56*(17), 5753.

28 Lourakis, M. I. A., & Argyros, A. A. (2005). Is levenberg-marquardt the most efficient optimization algorithm for implementing bundle adjustment? *Tenth IEEE International Conference on Computer Vision (ICCV'05) Volume 1*, *2*, 1526–1531 Vol. 2.

29 Lowengrub, J. S., Frieboes, H. B., Jin, F., Chuang, Y.-L., Li, X., Macklin, P., Wise, S. M., & Cristini, V. (2009). Nonlinear modelling of cancer: Bridging the gap between cells and tumours. *Nonlinearity*, *23*(1), R1.

30 Magnetism. (n.d.). http://mriquestions.com/dce-tissue-parmeters.html

31 Meyer, H. J., Garnov, N., & Surov, A. (2018). Comparison of two mathematical models of cellularity calculation. *Translational oncology*, *11*(2), 307–310.

32 Murphy, H., Jaafari, H., & Dobrovolny, H. M. (2016). Differences in predictions of ode models of tumor growth: A cautionary example. *BMC cancer*, *16*(1), 1–10.

33 Overview of the Breast - Breast Pathology | Johns Hopkins Pathology. (n.d.). https://pathology.jhu.edu/breast/overview/

34 Rejniak, K. A., & Anderson, A. R. (2011). Hybrid models of tumor growth. *Wiley Interdisciplinary Reviews: Systems Biology and Medicine*, *3*(1), 115–125.

35 Rieber, A., Brambs, H.-J., Gabelmann, A., Heilmann, V., Kreienberg, R., & Kühn, T. (2002). Breast mri for monitoring response of primary breast cancer to neo-adjuvant chemotherapy. *European radiology*, *12*(7), 1711–1719.
36 Shamonin, D., Bron, E., Lelieveldt, B., Smits, M., Klein, S., & Staring, M. (2013). Fast parallel image registration on CPU and GPU for diagnostic classification of Alzheimer's disease. *Frontiers in Neuroinformatics*, *7*. https://doi.org/10.3389/fninf.2013.00050
37 Stewart, B., & Wild, C. (2014). *World cancer report 2014*. IARC Press.
38 The Cancer Imaging Archive". (2020). Welcome to The Cancer Imaging Archive. https://www.cancerimagingarchive.net/
39 Understand Your Breast Cancer Diagnosis | Types of Breast Cancer. (n.d.). https://www.cancer.org/cancer/breast-cancer/understanding-a-breast-cancer-diagnosis.html
40 van Ramshorst, M. S., Loo, C. E., Groen, E. J., Winter-Warnars, G. H., Wesseling, J., van Duijnhoven, F., Peeters, M.-J. T. V., & Sonke, G. S. (2017). Mri predicts pathologic complete response in her2-positive breast cancer after neoadjuvant chemotherapy. *Breast cancer research and treatment*, *164*(1), 99–106.
41 Vuik, B., & Lahaye, D. (2019). *Scientific Computing* (Vol. 2019). Delft University of Technology.
42 Vuik, C., Vermolen, F., van Gijzen, M., & Vuik, M. (2015). *Numerical methods for ordinary differential equations* (2nd ed.). TU Delft.
43 Wang, Z., & Deisboeck, T. S. (2008). Computational modeling of brain tumors: Discrete, continuum or hybrid? *Scientific modeling and simulations* (pp. 381–393). Springer.
44 Weis, J. A., Miga, M. I., Arlinghaus, L. R., Li, X., Abramson, V., Chakravarthy, A. B., Pendyala, P., & Yankeelov, T. E. (2015). Predicting the response of breast cancer to neoadjuvant therapy using a mechanically coupled reaction–diffusion model. *Cancer research*, *75*(22), 4697–4707.
45 Weis, J. A., Miga, M. I., Arlinghaus, L. R., Li, X., Chakravarthy, A. B., Abramson, V., Farley, J., & Yankeelov, T. E. (2013). A mechanically coupled reaction–diffusion model for predicting the response of breast tumors to neoadjuvant chemotherapy. *Physics in Medicine & Biology*, *58*(17), 5851.
46 Weis, J. A., Miga, M. I., & Yankeelov, T. E. (2017). Three-dimensional image-based mechanical modeling for predicting the response of breast cancer to neoadjuvant therapy. *Computer Methods in Applied Mechanics and Engineering*, *314*, 494–512. https://doi.org/10.1016/j.cma.2016.08.024
47 Whisenant, J. G., Ayers, G. D., Loveless, M. E., Barnes, S. L., Colvin, D. C., & Yankeelov, T. E. (2014). Assessing reproducibility of diffusion-weighted magnetic resonance imaging studies in a murine model of her2+ breast cancer. *Magnetic resonance imaging*, *32*(3), 245–249.
48 World health organization: Cancer. (n.d.). https://www.who.int/en/news-room/fact-sheets/detail/cancer
49 Yankeelov, T. E., & Gore, J. C. (2007). Dynamic contrast enhanced magnetic resonance imaging in oncology: Theory, data acquisition, analysis, and examples. *Current Medical Imaging*, *3*(2), 91–107.